Optimizing Compton Camera Performance

A thesis submitted in partial fulfilment
of the requirements for the degree of

Doctor of Philosophy

in

Physics

at

The University of Waikato

by

Chibueze Uche

THE UNIVERSITY OF
WAIKATO
Te Whare Wānanga o Waikato

2011

Abstract

A more realistic simulation approach is used to study the behavior of the Compton camera in this thesis than previous studies to date. The Compton camera differs from gamma cameras in that the collimator is replaced by a detector known as the 'scatterer'. Gamma rays may be Compton scattered in the scatterer and subsequently detected by an 'absorber' which is the equivalent of the detector in a gamma camera. By measuring the energies and the positions of the points on the scatterer and the absorber where the incident and scattered gamma rays interacted with the detectors, an image of the source can be reconstructed. Because there is no collimator present, the potential sensitivity of the Compton camera is much higher than the gamma camera, resulting in reduced acquisition times.

Most of the work described in this thesis was done with the GEANT4 Monte Carlo simulation software. GEANT4 has been proven to be very robust and efficient in modelling physics problems of radiation transport and interactions with matter in complex geometries. Four major studies are carried out to estimate and optimize the performance of this novel equipment. The first study takes a look at the scatterer's imaging parameters with the aim of prescribing an optimal scatterer material and geometry. In the second study, the contribution of the absorber to the overall Compton camera performance is evaluated, considering detector material, interaction type and geometry. The third study explores the limitations imposed by the detector energy threshold and dead time on the Compton camera performance, using a simplified model of the general electronic architecture. An evaluation of Compton camera for scintimammography was performed in the fourth study. For this study, three dual-head Compton camera models (Si/CZT, Si/$LaBr_3$:Ce and Si/NaI(Tl) Compton cameras) were simulated, and the effect of scintillation photons' interactions with the photomultipliers was implemented.

The results show that silicon of about 1 cm thickness would be adequate as the Compton camera scatterer. Analyses suggest however, that the choice of silicon is not completely flawless. Doppler broadening for this detector material contributes as much as 7.3 mm and 2.4 mm to full-width-at-half-maximum (FWHM) image resolution at 140.5 keV and 511 keV respectively. On the other hand, detector spatial resolution which accounts for the least image degradation at 140.5 keV is found to be the dominant degrading factor at 511 keV, suggesting that the absorber parameters play major roles in image resolution at higher diagnostic energies. Findings further suggest that cadmium zinc telluride (CZT) would be the most suitable detector as the absorber since the material demonstrated the high-

est efficiency and least positioning error due to multiple interactions as well as good spatial resolution. The inclusion of the energy threshold and detector dead time at 140.5 keV, reduced the Compton camera detection efficiency by 48% and 17% respectively, but improved the image resolution from 10.7 mm to 9.5 mm at the source-to-scatterer distance of 5 cm. At 511 keV, the inclusion of these parameters reduced the efficiency by 6% and 13% respectively, but made no significant difference on the camera resolution. For a challenging detection case in scintimammography, 5 mm breast tumours of tumour/background uptakes of 10:1 and 6:1 at 511 keV were used. The best signal-to-noise ratio (SNR) was attained for the Si/CZT Compton camera model, with the SNR values of 12.2 and 5.3.

It is therefore envisioned that with an optimal camera geometry, improved reconstruction technique and adequate filter algorithm, the combination of Si and CZT as the scatterer and the absorber of the Compton camera would make a very promising imaging system for nuclear medicine studies at higher gamma ray energies where the collimated SPECT systems perform very poorly due to increased septal penetration. It is equally evident from the studies that with improved technology, new detectors such as $LaBr_3$:Ce could replace the traditional NaI(Tl) detector as imaging detectors.

Acknowledgement

There is a lot to know, to know that we need to know. My thoughts and gratitude turn first to my supervisor, Dr Howell Round. He is the first to see my hidden talents even in the face of glaring discouraging background. Many of the ideas, principles and results that appear in this thesis stem from thoughts provoked by his guidance, encouragement and corrections over the last four years. I am sure it has set me in good stead for the future. My co-supervisor, Dr Michael Cree took enormous trouble I am not able to repay to fortify my research skills. To him I owe my deep thanks. His expert critical opinions have made this thesis a much better one. Associate Professor Alista Steyn-Ross kept his door opened to my numerous questions on MATLAB programming. I express my appreciation to my current and former colleagues, Alista Fow, John Godbaz, Dr Lee Streeter, Suihali Zakariah and Padmanaban Sadasivam for their warm companionship. I was about despairing of making any headway when I received a GEANT4 code from Hee Seo. That code was a gold mine! I am also grateful to other international collaborators, Dr Soo Mee Kim and Dr Andriy Andreyev who lent me their reconstruction algorithms.

If I had known half of the story I would not have dared; but my family ‘climate’ was balanced by my wife, Onyinye (English meaning — Gift). All that became wanting in me was supplied by her. My enormous thanks to my children, Esther, Israel and Emmanuel for daily evenings of laughter and play after exhausting studies. Those moments were real healings to my frustrations and miseries. To all those people who have given me personal support, their love and their prayers, I am very grateful.

Above all, I thank you O God, my mighty Fortress, for the hard times, for they have taught me the secret treasures of courage, perseverance and trust. Let my life always please you until I see your face, Lord Jesus, amen.

The fear of the LORD is the beginning of wisdom: and the knowledge of the holy is understanding
(*Proverbs 9:10*)

Contents

List of Figures

List of Tables

Chapter 1

INTRODUCTION TO MEDICAL NUCLEAR IMAGING

Nuclear medical imaging is a generic term for the imaging techniques that make use of ionizing radiation emanating from within the body to determine a physiological component that is not obtainable with most other imaging modalities (Cree and Bones, 1994). The radiation source is usually a short-lived isotope linked to a chemical compound that permits specific physiological processes to be scrutinised. It is given by injection, inhalation or orally in trace amounts. The compound then accumulates in the patient and the pattern of its subsequent radioactive emission is used to estimate the distribution of the radioisotope. Information gained from these techniques is often useful in evaluating the functions of human organs, as well as detecting sites with infections or tumour growth. They also serve as valuable adjuncts to other imaging techniques such as x-ray mammography and magnetic resonance imaging as they provide complementary information about the patient. A distinct advantage of nuclear medical imaging over x-ray techniques is that both bone and soft tissue can be imaged.

The first tomographic method of nuclear medical imaging is single photon emission computed tomography (SPECT). In SPECT, single photons are detected by a gamma camera which can view organs from many different angles. The camera measures the projections to the radiation emission points. The image is reconstructed by a computer and viewed by a physician on a monitor for indications of abnormal conditions (McKillop, 1996).

The second tomographic method of nuclear medical imaging is positron emission tomography (PET) which uses radioisotopes produced in a cyclotron. For PET imaging, a positron-emitting radionuclide is introduced by injection, and accumulates in the target tissue. As it decays it emits a positron, that promptly combines with a nearby electron resulting in the simultaneous emission of two identifiable gamma rays in opposite directions. These are detected by a PET camera which gives an indication of their origin. PET's most important clinical role is in oncology, with ^{18}F as the common radiotracer. It is also well used in cardiac and brain imaging (Phelps *et al.*, 1975; Hawkins and Phelps, 1988; Cherry *et al.*, 2003).

In some imaging centres, nuclear medical images can be superimposed with computed tomography (CT) or magnetic resonance imaging (MRI) images to produce special views, a practice known as image co-registration. These views allow the information from two different studies to be correlated and interpreted on one image, leading to more precise information and accurate diagnoses. Along these lines, manufacturers are now making Single Photon Emission Computed Tomography/Computed Tomography (SPECT/CT) and Positron Emission Tomography/Computed Tomography (PET/CT) units that are able to perform both imaging studies at the same time. These are believed to be very powerful and significant tools that can provide unique information on a wide variety of diseases from dementia to cardiovascular disease and cancer (Beyer *et al.*, 2000; Townsend and Beyer, 2002).

It is important in nuclear medical imaging that the energy and the direction of the administered radiotracer be measured as accurately as possible to provide reliable medical information to the clinician. The accuracy of the energy and the direction information, of course, relies significantly on the operating condition of the imaging system. Consequently, the question of how to optimize the existing and new system models has become a major challenge and is a very active area of research. While it is true that the performance of PET systems has been greatly advanced by diverse optimization measures, only marginal improvements in resolution and sensitivity have been recorded in SPECT despite the tremendous efforts that have been invested in detector research and collimator design (Hua, 2000).

SPECT limitations arise from diverse complexities associated with system designs. The most obvious reason SPECT resolution and efficiency are difficult to improve is that SPECT is still performed using the Anger camera (Anger, 1958), equipped with a mechanical (lead) collimator to determine the distribution of the radiotracer. The need for a mechanical collimator places a physical limit that couples detection efficiency and spatial resolution in an inverse trend, thus limiting the achievable resolution for a specific dose limit. A primary consideration in collimator design is the septal thickness, which can be evaluated by analysis of Figure 1.1(a). As Figure 1.1(a) suggests, septal thickness t depends on the shortest path length w for the gamma rays to travel from one collimator hole to the next, the collimator length l and the diameter d of the collimator holes. The relationship between septal thickness t and the other parameters can be expressed as (Cherry *et al.*, 2003)

$$t \approx \frac{2dw}{l-w}. \tag{1.1}$$

It is generally desirable that t be as small as possible so that the collimator septa obstruct the smallest possible area of detector surface thereby maximizes the collimator efficiency g, which can be defined as the fraction of gamma rays that pass through the collimator for each gamma ray emitted by the source. The collimator efficiency is related to septal thickness in

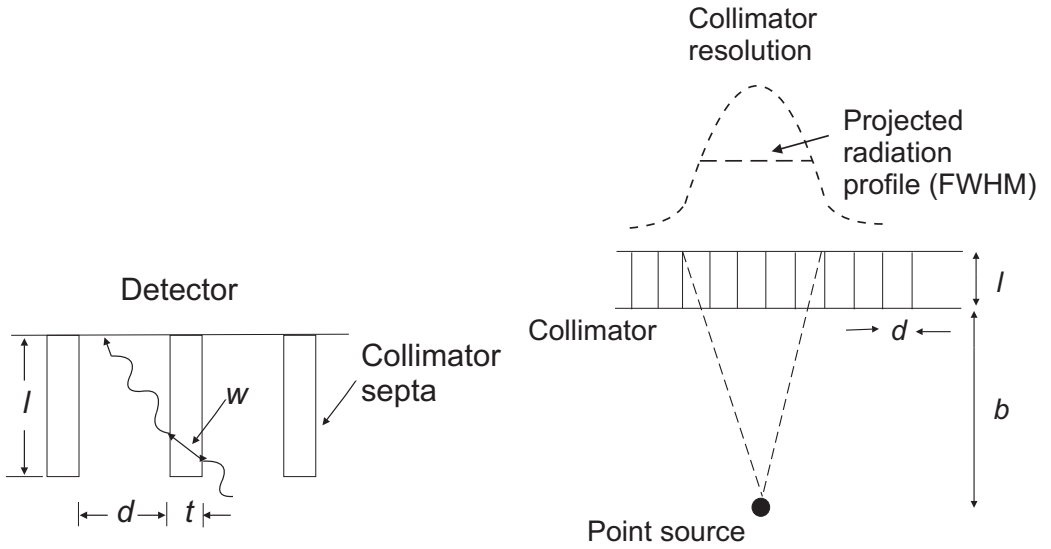

(a) (b)

Figure 1.1: (a) A diagram illustrating how the minimum path length w for a gamma ray passing through the collimator septa from one hole to the next depends on length l and diameter d of the collimator holes and on septa thicknesses t. (b) A diagram showing how the collimator resolution is derived from radiation profile (FWHM) for a parallel-hole collimator. Figures adapted from Cherry *et al.* (2003).

the following way,

$$g \approx K^2 \left(\frac{d}{l_e}\right)^2 \left(\frac{d^2}{(d+t)^2}\right), \tag{1.2}$$

where K is a constant that depends on the hole shape, normally taken to be 0.24 for round holes in a hexagonal array, 0.26 for hexagonal holes in a hexagonal array and 0.28 for square holes in a square array (Cherry *et al.*, 2003)). The term l_e is the effective length of the holes, and defined as

$$l - 2\mu^{-1}, \tag{1.3}$$

where μ is the linear attentuation coefficient of the collimator material. The effective length of the collimator holes l_e is somewhat less than the actual collimator length l due to septal penetration. The collimator resolution R_c, which refers to the sharpness or detail of the gamma ray image projected onto the detector can be expressed from Figure 1.1(b) as

$$R_c \approx \frac{d(l_e + b)}{l_e} \tag{1.4}$$

An approximate relationship between collimator efficiency, g, and collimator resolution, R_c is (Cherry *et al.*, 2003)

$$g \propto R_c^2. \tag{1.5}$$

It follows that for a given septal thickness, collimator resolution is practically improved at the expense of decreased collimator efficiency, and vice versa. Again, the use of the

collimator places a substantial limit on the camera's field of view. This is because only the photons travelling approximately parallel to the axis of the holes are allowed to pass through the holes without being absorbed in the lead. This necessitates the rotation of the Anger camera around the patient for performing SPECT. Problems become substantially worse when attempting to image high energy gamma rays. The incident energy of the photons has to be, at most, a few hundred keV otherwise photons will penetrate through the collimator and increase the image background. In reality, no thickness of septal material is sufficient to stop all gamma photons, so the usual criterion is to accept some reasonably small level of septal penetration (approximately 5%). As the quantity of the radiotracer administered is restricted by the allowable radiation dose to the patient, imaging times are often long in order to collect a statistically sufficient number of photons. To overcome these fundamental drawbacks, the Compton camera has been proposed to hold a better future than the conventional SPECT technique (Singh, 1983; Singh and Doria, 1983; Todd *et al.*, 1974).

1.1 Radiopharmaceuticals

The gamma ray source for nuclear medical imaging is the radiopharmaceutical (radioactive drug) injected into the patient's body for either medical diagnosis or treatment of disease. It can be thought of as comprised of two compounds: a radioactive compound that produces the radiation to be detected and a non-radioactive compound that provides the distinctive chemical and physical properties. Good imaging requires an accurate determination of a specific tissue's function, shape, or distribution of a radioactive source within the tissue. Radiopharmaceuticals must therefore emit gamma rays of sufficient energy to escape from the body which must be readily detectable in minute amounts. The compounds must not be toxic in the amounts utilized, and should not be present previously in the body. They must not in any way disturb the very phenomena under investigation. It is desirable that the radioactive compounds disappear from the body with sufficient rapidity to allow repeated measurements if necessary. Their availability at low cost and ease of production is also critical. Different radiopharmaceuticals have different affinity to a specific bodily function, hence the choice of radiopharmaceuticals is often based on their preference to collect around certain bodily functions or organs (Cree, 1994).

The first implementation of a radiopharmaceutical to study a physiological process was accomplished by Blumgart and Yen in 1927 (Blumgart and Yen, 1927). They used a gas-filled detector to measure the arm-to-arm transit time of a bolus of dissolved radium C injected into an antecubital vein of one arm, timing its appearance in the other arm by observing the response in a shielded cloud chamber.

In the 1950s, gamma scintigraphy was developed by Hal O. Anger, an electrical engineer at Lawrence Berkeley Laboratory (Anger, 1958). This imaging procedure requires a radiopharmaceutical containing a radionuclide that emits gamma radiation and a SPECT camera capable of imaging the patient injected with the gamma emitting radiopharmaceutical. Since then, the most widely used radiopharmaceutical for SPECT became ^{99m}Tc ($T_{1/2}$

= 6 hours), which is produced from the decay of ^{99}Mo ($T_{1/2}$ = 66 hours). The low cost and convenience of the ^{99}Mo/^{99m}Tc generator, as well as the ideal photon energy of ^{99m}Tc (140 keV), are the key reasons for its widespread use. A wide variety of ^{99m}Tc radiopharmaceuticals have been developed during the last forty years. Many of them are currently used every day in hospitals around the world to aid in the diagnosis of heart disease, cancer, and an assortment of other medical conditions.

PET was developed by Ter-Pogossian et al. at Washington University during the 1970s (Ter-Pogossian *et al.*, 1975). This imaging modality requires a radiopharmaceutical labelled with a positron emitting radionuclide (β^+) and a PET camera for imaging the patient. Positron decay results in the emission of two 511 keV photons 180° apart. PET scanners often contain a circular array of detectors with coincidence circuits designed to specifically detect the 511 keV photons emitted in opposite directions. The positron emitting radionuclides most frequently used for PET imaging are ^{15}O ($T_{1/2}$ = 2 minutes), ^{13}N ($T_{1/2}$ = 10 minutes), ^{11}C ($T_{1/2}$= 20 minutes), and ^{18}F ($T_{1/2}$ = 110 minutes). Of these, ^{18}F is most widely used for producing PET radiopharmaceuticals. The most frequently used ^{18}F labelled radiopharmaceutical is 2-deoxy-2 [^{18}F]fluoro-D-glucose (FDG). This agent is routinely used to image various types of cancer as well as heart disease.

The Compton camera principle differs significantly from those of the Anger and PET cameras. However, research has shown that the camera can also image the distribution of radiopharmaceuticals used in conventional SPECT and PET. The imaging resolution of the Compton camera is nevertheless better for radionuclides with higher photon energies, such as ^{131}I or positron sources ^{11}C, ^{18}F, ^{13}N and ^{15}O. Table 1.1 shows the properties of selected radionuclides that are commonly used for nuclear medical imaging (McCarthy *et al.*, 1994; Troy, 2006). The common production method of the radionuclides is described by the general expression

$$X(BP, EP)Y, \tag{1.6}$$

where X is the target element, BP is the bombarding particle, EP is the emitted product and Y is the product element. Table 1.1 shows that radionuclides can decay by one or more than one possible mode (positron emission, electron capture and so on). In each decay process, high photon abundance is desirable in that it fosters high photon flux and minimizes the imaging time. By photon abundance, we refer to the percentage (or fractional) yield of the photon emitted for each decay process. This factor also represents the fraction of the time taken to emit a gamma ray during a decay process. It is possible for photon abundance to exceed 100 % in a particular decay event because deexcitation may occur through sequential emissions from different nuclear excited states. An example is the case of ^{11}C radionuclide. In this case, the nucleus decays about 100 % of the time by positron emission, the emitted positron recombines with a nearby electron and emits two gamma rays of 511 keV each at 180° apart, creating a photon abundance of 200 %. Another example is the case of ^{111}In radionuclide. In this case, nucleus decays about 100 % of the time by electron capture, leading to an excited state of ^{112}Cd. This excited state deexcites about 90 % of the time

Table 1.1: A table of selected radionuclides used in nuclear medical imaging. EC stands for electron capture, IT for isomeric transition, d for deuteron, n for neutron, p for proton and α for alpha particle.

Radionuclide	Half life	Mode of decay	Energy (keV)	Abundance of primary photons (%)	Common production method
^{11}C	20.4 min	β^+	511	200	^{10}B(d, n)^{11}C
^{18}F	110 min	β^+, EC	635 511	97 194	^{18}O(p, n)^{18}F
^{123}I	13.2 hr	EC	27 159	71 84	^{123}I(p, 5n)^{123}Xe daughter
^{131}I	8.04 days	β^-	284 364	6 82	fission
^{111}In	67.3 hr	EC	171 245	90 94	^{112}Cd(p, 2n)^{111}In
^{13}N	10 min	β^+	511	200	^{10}C(d, n)^{13}N ^{10}O(p, α)^{13}N ^{13}C(p, n)^{13}N
^{15}O	2 min	β^+	511	194	^{18}O(p, n)^{18}F
^{99m}Tc	6.02 hr	IT	18 140	6.5 89	^{99}Mo daughter

with the emission of a 171 keV gamma ray, and in the other 10 % of the deexcitation a conversion electron is emitted rather than a gamma ray. The initial deexctation leads to a lower excited state that also deexites about 94 % of the time with the emission of a second gamma ray with an energy of 245 keV. The sum of the two gamma ray yields gives the photon abundance of 184 %.

1.2 The Compton camera

A simple model for the Compton camera consists of two planar detectors, the scatterer at the front and the absorber at the back, that operate in time coincidence. Figure 1.2(a) shows a schematic diagram of a typical Compton camera model. For a successful image reconstruction, a gamma photon emitted from a radioisotope source must undergo Compton scattering with a shell electron inside the scatterer where the time of interaction, position of interaction and kinetic energy of the recoil electron are measured. The scattered photon must escape from the scatterer and undergo photoelectric absorption inside the absorber

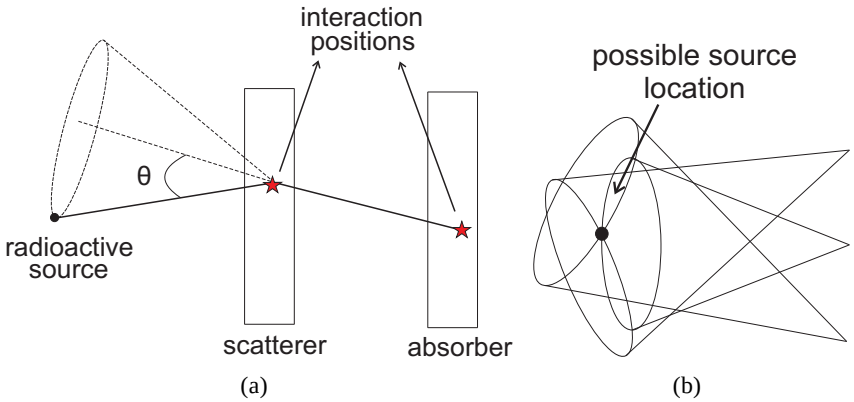

Figure 1.2: (a) A diagram of the Compton camera, (b) accumulation of backprojected cones to locate a point radioactive source (in principle, three cones can be used to locate a source).

where the time of interaction, position of energy deposition and the total energy deposited are also measured. The path of the scattered photon between the detectors allows the axis of a cone within which the source may possibly be located to be drawn and the recoil electron energy deposited in the scatterer permits the scattered photon angle to be estimated. This information constrains the incoming photon to lie on a cone surface without limiting the incident photon flux, and subsequent accumulation of the cone beams shows the possible location of the source (Figure 1.2(b)). Detailed discussions on the Compton camera operation principles are presented in Chapter 2.

It is obvious from the above that the Compton camera scatterer replaces the mechanical collimators used regularly with clinical Anger cameras by the sometimes-called electronic collimation using the Compton effect (Meier *et al.*, 2002). Unlike Anger cameras, the Compton camera's useful energy range extends over the region of gamma ray energies where Compton scattering is the dominant process, from about 100 keV to beyond 10 MeV (Phillips, 1995). However, building a practical Compton camera system with a high resolution and sensitivity in the energy range of nuclear medicine presents more serious design challenges that result from optimizing various camera parameters. This notwithstanding, high performance is needed to reduce exposure times, and/or improve image quality. High sensitivity translates to better contrast, shorter imaging time and consequently, lower dose to the tissue or organ under examination. Also, a high resolution provides the ability to accurately trace the distribution of a radiopharmaceutical located in a given region of the body. The desire to optimize Compton camera performance for medical procedures that favour compact and lightweight imaging systems motivated this thesis.

1.2.1 Compton camera parameters

Extensive evaluations of how the Compton camera parameters impact on its performance are the major consideration in this thesis. The reason is that the camera's parameters govern its behaviour. Research (Studen, 2005a) has shown that the Compton camera parameters

can be categorized as:

Energy resolution: This parameter reflects the measurement uncertainty in determining the energy to the recoil electron. It depends strictly on the physics of particle interactions with the surrounding media and specific intrinsic detector characteristics. The degree of energy resolution of the Compton camera is dominated by the choice of the scatterer material and governs its ability to resolve between two close radiation energy peaks.

Doppler broadening: This parameter adds to the uncertainty generated by the energy resolution. It is the spread of the energy spectra due to Compton interaction between a photon and a moving electron bound to an atom in the scatterer. Doppler broadening decreases with increasing incident energy of the gamma photons, thus favouring the choice of higher energy radiation, which is in strong contrast to the requirement of the Anger camera.

Detector Material: The density and effective atomic number of the detector material determine the type and number of interactions the incident gamma rays can undergo, therefore, defines fundamental limits on the sensitivity and spatial resolution.

Geometry: The importance of the nature of Compton camera geometry is underscored by the small tradeoff that exists between the spatial resolution and sensitivity. A decrease in source-to-scatterer distance for instance increases sensitivity and angular uncertainty simultaneously. However, angular uncertainty in medical Compton cameras does not dominate the spatial resolution as position uncertainty does, and the tradeoff between Compton camera spatial resolution and sensitivity is less than that of the Anger camera.

Charge collection time: This is the time interval after a radiation interaction, during which the signal current flows between the terminals of the detector. This parameter is controlled by the detector readout characteristics such as dead time, detector time resolution and thresholds.

It is worth mentioning that the list of the Compton camera parameters can be continued. The examples above are just the ones considered in this thesis. Note that in reality, the Compton camera parameters are difficult to isolate, they are only detected and estimated through their manifestations.

1.2.2 Historical résumé of methods employed in studying the Compton camera

The concept of Compton coincidence detection was first implemented by Hofstadter and McIntyre in 1950 for a two-plane sodium iodide (NaI) scintillator system in which the energy of the recoil electron in the first detector and the energy of the backscattered photon in the second detector were measured with good accuracy (Hofstadter and McIntyre, 1950). Since then, the technique has been implemented in diverse fields such as gamma ray astronomy, industrial imaging, radioactive waste management and nuclear medical imaging (Phillips, 1995).

Compton coincidence detection was implemented for the first time in gamma ray astronomy in the form of the Compton telescope by Schönfelder et al. in 1973 for imaging

the distributions of the cosmic and atmospheric gamma rays (Schönfelder *et al.*, 1973). The group had for their initial Compton telescope design two large plastic scintillation detectors, separated 1.20 m apart, and operated at an energy range of 1 MeV to 10 MeV. The telescope model has an opening half angle of 15° with an energy resolution of ± 20% and an absolute detection efficiency of about 0.5%. The sequence of gamma detection in this telescope was verified by the collision time information in the two detectors which was used to eliminate undesirable cosmic radiation backgrounds. Two gamma ray sources, ^{60}Co and ^{24}Na, were used to characterize the performance of the telescope in the laboratory. However, the energy and angular resolution of the Compton telescope needed to be improved to obtain more valuable information on specific celestial structures in the gamma ray energy spectrum. This telescope was afterwards modified and called COMPTEL (COMPton TELescope) (Schönfelder *et al.*, 1984), which had a better angular resolution of 2° at 1 MeV and 0.7° at 10 MeV. The COMPTEL later on, developed into a joint project by several countries for imaging gamma rays emitted by celestial bodies in the energy range of 1 MeV to 30 MeV (Schönfelder *et al.*, 1996).

The possible application of the Compton camera in the field of nuclear medical imaging was first proposed by Todd *et al.* (1974) one year after its introduction in gamma ray astronomy. The proposal presented new prospects as well as new challenges to the nuclear medical imaging field. Specifically, the Compton camera higher sensitivity over the traditional SPECT systems, wider imaging field of view and ability to image a wider range of radiopharmaceutical energies (typically, 100 keV to 600 keV) captured a lot of interest. However, excellent energy resolution is required for the scatterer to match or surpass the image resolution of the traditional SPECT systems at the low to medium radiopharmaceutical energies. Other challenges lie on the fact that high position resolution and more robust reconstruction algorithms are needed for imaging complicated physiological structures in three dimensions, with a limited number of gamma photons emitted from the source, in a limited data acquisition time to reduce the radiation dose to the patient (Çonka Nurdan, 2004).

A great deal of effort has been put forth by several research groups to study the application of Compton cameras in nuclear medical imaging. Singh et al. published a series of papers that described the theories upon which the Compton camera is based (Singh *et al.*, 1977; Singh, 1983; Singh *et al.*, 1988). Their grasp of the essentials of the camera's operation principles was extraordinary. From their estimation, the Compton coincidence detection capability of the camera should lead to a higher sensitivity than that obtainable with a mechanically collimated gamma camera and also provide multiple views of the source simultaneously. They proposed that the cumulative signal-to-noise ratio in projection images obtained with a simulated system with a 33 × 33 array of germanium detectors was expected to be about a factor of four higher than that obtained in a corresponding projection image with a conventional gamma camera when imaging a uniformly distributed ^{99m}Tc source in a 20 cm diameter and 20 cm tall cylinder. Singh (1983) described how the detector type and size could affect the Compton camera performance. The group also published experimen-

tal results for a Compton camera composed of a pixelated high-purity germanium (HPGe) scatterer and an uncollimated conventional Anger camera absorber (sodium iodide) (Singh and Doria, 1983, 1985; Singh and Chris, 1987). Their results for a ^{99m}Tc (140.5 keV) point source showed that their prototype camera had a sensitivity gain of an order of magnitude at the same spatial resolution with the mechanically collimated camera. However, the reconstructed images were somewhat worse than predicted and suggested that, there may be some other factors that were not captured in their theoretical evaluations and which caused disagreements between the predicted and experimental results, and therefore failed to predict the Compton camera behaviour accurately. Further, the germanium detector which they used is very expensive and requires liquid nitrogen cooling. In recent years, radiation detector technology has advanced significantly, leading to detectors with better energy resolution, lower noise, lower cost, and no need for cryogenic cooling. Further limitation of Singh's camera was that of large detector dead time of the sodium iodide absorber processing electronics due to extremely high photon events rates at higher energies (LeBlanc, 1999). Singh's scatterer detector was subsequently lent to Martin et al. to investigate the potentials of a ring geometry Compton camera to image radioactive spills, monitor nuclear wastes and medical imaging (Martin *et al.*, 1993, 1994; Martin, 1994; Rogers *et al.*, 2004). However, Martin's camera suffered low sensitivity which resulted from the small solid angle of the second detector.

The problem of Compton camera implementation in the medical field received its next impetus in 1997, when Ordonez *et al.* (1997) studied the role of Doppler broadening to the detector energy resolution. The group predicted that Doppler broadening causes non-negligible uncertainty in the scattered photon energy and angular uncertainty, and therefore could have non-negligible degrading effects on the reconstructed source image. Wilderman *et al.* (1998b) validated Ordnez et al.'s predictions by showing the degrading effects of Doppler broadening on the reconstructed images of a point source at the low and medium gamma ray energies. More fruitful to the Doppler broadening problem were the approaches of Hirasawa and Tomitani (2003), and Wilderman *et al.* (2001) who proposed that the parameter must be properly accounted for in the reconstruction algorithms for the Compton camera to match or surpass the imaging resolution of the Anger counterpart at low gamma ray energies. A further increase in spatial resolution was achieved by LeBlanc et al by replacing Singh's high purity germanium scatterer with a silicon pixel detector (LeBlanc *et al.*, 1998, 1999; Leblanc *et al.*, 1999). LeBlanc's camera was intended for low to medium gamma ray energies. However, its reconstructed image quality was equal or worse than that of conventional Anger cameras. Other innovative models for the Compton camera include that of Zhang et al who demonstrated the camera's potential imaging capability for scintimammography (Zhang *et al.*, 2004). The group illustrated by Monte Carlo simulations, the possible imaging of breast cancer tumours of 5 mm diameter with a novel Compton camera, which the Anger camera is presently incapable of. An et al studied the effects of basic detector parameters such as the Doppler broadening, energy resolution, detector segmentation and energy discrimination on the image resolution at 140.5 keV (An *et al.*, 2007). They

used only 10 000 photon events to reconstruct the gamma source image, resulting in poor estimation of image resolution for the effect of energy discrimination. However, the group predicted that the use of a higher energy radiotracer such as ^{18}F as well as further reduction in the size of the absorber pixel elements to a few millimetres or less could achieve an image resolution of 5 mm required for medical imaging.

Several known, but inadequate reconstruction techniques, have been proposed for the medical Compton camera. The major challenge in developing a reliable and robust reconstruction algorithm is that the directional localization in medical Compton cameras requires complicated chains of steps to localize complex source structures with unknown source distributions, unlike in gamma astronomy where the imaging source is often point-like or an object of known and simple structure. The simplest reconstruction for the medical Compton camera is the direct back-projection of cones from each event onto an image plane. In this reconstruction technique, there is a cone associated with each photon that is counted. Therefore the intensity of a reconstructed voxel is the sum of integrals associated with the cones that intersect the voxel. Unfortunately, images produced with this reconstruction technique are often noisy and suffer from poor spatial resolution. To improve the image quality, Singh et al. developed iterative algorithms that work relatively better in terms of image resolution for the case of point sources and simple extended sources, but the time of convergence of the algorithms is clinically unacceptable (Singh and Doria, 1983; Hebert *et al.*, 1990). An alternative technique was proposed by Cree and Bones (1994), who developed two kinds of analytical algorithms for direct reconstruction in terms of integral transformations. The sensitivity of their camera is however, severely limited because only the scattered photons with direction perpendicular to a detector array are accepted as valid events. Comprehensive efforts that have been put forth to develop a robust reconstruction scheme can be found in (Wilderman *et al.*, 1998b; Basko *et al.*, 1998; Sauve *et al.*, 1999; Parra, 2000; Wilderman *et al.*, 2001; Tomitani and Hirasawa, 2002; Smith, 2005; Kim *et al.*, 2007; Maxim *et al.*, 2009; Kim *et al.*, 2010; Andreyev *et al.*, 2011). The development of a fully 3-D robust algorithm to reconstruct the acquired data from a medical Compton camera is an ongoing effort that is not addressed in this thesis. Rather, the basic principles of the reconstruction method, list-mode backprojection is explained in Chapter 2.

Medical imaging devices are usually very expensive. Consequently efficient simulation of system design and good optimization measures are often advantageous before the actual construction. There does not appear to have been an extensive effort by researchers to optimize the Compton camera performance. Few that attempted optimizing their specific designs did it in fragments and completely ignored the impact of the data acquisition system on the Compton camera data, thereby caused irreconcilable errors between their simulated results and experimental data. Previous attempts to optimize the Compton camera performance are discussed as follows. A report by Chelikani *et al.* (2004) described the optimization of a custom Compton camera geometry. They achieved, by manipulating the geometric parameters, a sensitivity gain of two orders for a Compton camera prototype whose geometric dimensions are similar to those of the conventional Anger camera. However, they

ignored the effects of finite energy and spatial resolutions leading to overestimation of the image resolution at 140 keV. An optimal geometrical study for a double-scattering Compton camera was carried out by Seo *et al.* (2008). The group showed a better improvement of the image resolution by the use of two parallel silicon detectors as scatterers, but at serious expense of the sensitivity. This is because sensitivity for their camera required that interactions must take place in the two scatterers and the absorber, thereby eliminating a significant fraction of useful events. Harkness *et al.* (2009) carried out an optimization study on a dual head semiconductor Compton camera. Their metric of optimization was the fraction of events that interacted with a single Compton scattering and a single photoelectric interaction in the scatterer and the absorber respectively, for various detector materials. However, their study did not include the effects of Doppler broadening, energy resolution and finite detector resolution. These research groups acknowledged that more work needs to be done to bring the Compton camera performance to an optimal level. Therefore, in response to the desire to optimize the Compton camera performance, this thesis has sought to explore extensive evaluation mechanisms using a complex Monte Carlo particle transport simulation toolkit, GEANT4 (Agostinelli *et al.*, 2003), to model and optimize a novel Compton camera system. Effort was put forth to relate a similar Compton camera prototype to clinical performance.

1.3 The GEANT4

GEANT4 is an acronym for GEometry ANd Tracking. The GEANT4 toolkit is a platform for the simulation of the passage of particles through matter, using Monte Carlo methods. It is the successor of the GEANT series of software toolkits developed by CERN, and the first to use object-oriented programming (in C++). Its development, maintenance and user support are taken care by the international GEANT4 Collaboration, and in this respect, GEANT4 acts as a repository that incorporates a large part of all that is known about particle interactions. Application areas include high energy physics and nuclear experiments, medical, accelerator and space physics studies. The software is used by a number of research projects around the world. It runs on operating systems such as Linux, Unix and Windows. The GEANT4 software and source code is freely available from the project web site (geant4.web.cern.ch, 2011). GEANT4 includes facilities for handling geometry, tracking, detector response, run management, visualization and user interface. For many physics simulations, this means less time need be spent on the low level details, and researchers can start immediately on the more important aspects of the simulation.

1.3.1 GEANT4 features

Following is a brief description of each of the facilities listed above:

- Geometry is an analysis of the physical layout of the experiment, including detectors, absorbers, etc., and considering how this layout will affect the path of particles in the

experiment.

- Tracking is simulating the passage of a particle through matter. This involves considering possible interactions and decay processes.
- Detector response is recording when a particle passes through the volume of a detector, and approximating how a real detector would respond.
- The 'PhysicsList' class consist of a set of physics packages to describe the interactions of photons, electrons, hadrons and ions with matter. The Low Energy Electromagnetic package extends the coverage of electromagnetic interactions of photons and electrons down to 250 eV, and of protons, ions and antiprotons down to less than 1 keV.
- Optical physics processes in GEANT4 allow the wave like property of the electromagnetic radiation to be associated to a photon. The tracking of an optical photon therefore includes scintillation, Cerenkov, Rayleigh scattering, refraction and reflection at medium boundaries, and optical photon absorption.
- Run management is recording the details of each run (a set of events), as well as setting up the experiment in different configurations between runs.
- GEANT4 offers a number of options for visualization, including OpenGL, and a familiar user interface, based on Tcsh.
- GEANT4 can also optionally perform histogramming, but it requires external software that implements the AIDA framework in order to do so.

A more detailed description of the GEANT4 features is presented in Section 2.10.

1.3.2 Reason for choosing GEANT4

The structure of GEANT4 allows for modifications and improvements to meet different application needs. It is preferred for the simulation work described in this thesis because it offers the flexibility of understanding the steps of the imaging process and identifying the changes that have impact on Compton camera performance. Its Low Energy Electromagnetic package is very relevant to medical applications. Hence most of the work described in this thesis was done by GEANT4.

1.4 Thesis goals and original contributions

Because of the limitations and inaccuracies of the previous studies, there is a necessity to develop a more satisfying approach to accurately estimate the Compton camera operation as well as optimizing its performance. Towards this aim, the goals of this thesis are outlined in the following:

- To investigate the impacts of the scatterer's parameters on Compton camera performance.
- To perform an extensive study on the role of the absorber in Compton imaging.
- To investigate the effects of charge collection times on the Compton camera data.
- To evaluate the potentials as well as the limitations of the Compton camera in scintimammography.

The original contributions made by this research are summarised as follows.

- Validation of the results of the new 'LowEnergy' physics model of GEANT4 with respect to Doppler broadening as well as quantification of the effect of the parameter in Compton cameras intended for medical applications.
- Contributions of the absorber parameters to the overall performance of the Compton camera.
- Inclusion of the Compton camera data acquisition unit by simulation. This study involved further improvement of the GEANT4 code to include the photon emission times. as well as careful documentation of its limitations.
- Realistic prediction of the performance of the Compton camera in scintimammography. Unlike in previous studies of the Compton camera, scintillation photons were simulated along with detector boundary effects. A relatively new scintillation detector, cerium doped lanthanum tri-bromide ($LaBr_3$:Ce) was evaluated as the Compton camera absorber.

The limitations of the above studies as well as possible future improvements are also documented.

Journal Publications

The following publications were prepared during the course of this research:

Uche, C. Z., W. H. Round, and M. J. Cree, (2011) Effects of energy threshold and dead time on Compton camera performance. *Nuclear Instruments and Methods in Physics Research A*, 641, pp, 114-120.

Uche, C. Z., W. H. Round, and M. J. Cree, (2011) GEANT4 simulation of the effects of Doppler energy broadening in Compton imaging. *Australasian Physical & Engineering Sciences in Medicine*, "In Press" DOI: 10.1007/s13246-011-0076-2.

Uche, C. Z., W. H. Round, and M. J. Cree, (2011) A Monte Carlo evaluation of three Compton camera absorbers. *Australasian Physical & Engineering Sciences in Medicine*, "In Press" DOI: 10.1007/s13246-011-0085-1.

Articles Under Journal Review

The following paper(s) currently under journal review were prepared during the course of this research:

Uche, C. Z., W. H. Round, and M. J. Cree, Evaluation of two Compton camera models for scintimammography. *Nuclear Instruments and Methods in Physics Research A*, NIMA-D-11-00365.

Presentations and Abstracts

The following conference abstracts were prepared and presented orally during the course of this research:

Uche, C. Z., W. H. Round, and M. J. Cree, (2008) Monte Carlo simulation of a novel silicon/cadmium zinc telluride Compton camera *Australian Physical & Engineering Sciences in Medicine,* 31, No.4, Christchurch, New Zealand.

Uche, C. Z., W. H. Round, and M. J. Cree, (2010) A quantitative study of the performance of absorber materials in computer imaging *Australian Physical & Engineering Sciences in Medicine,* 34, No.1, Melbourne, Australia.

Uche, C. Z., W. H. Round, and M. J. Cree, (2011) A quantitative study of two Compton camera first plane detectors *Australian Physical & Engineering Sciences in Medicine,* 'Accepted', Darwins, Australia.

Uche, C. Z., W. H. Round, and M. J. Cree, (2011) Effect of the time characteristics of the Compton camera on its performance *Australian Physical & Engineering Sciences in Medicine,* 'Accepted', Darwins, Australia.

Uche, C. Z., W. H. Round, and M. J. Cree, (2011) A Monte Carlo simulation of a novel Si/LaBr3:Ce Compton camera for scintimammography *11^{th} Asian-Oceania Congress of Medical Physics,* 'Accepted', Fufuoka, Japan.

Chapter 2

ABSTRACT DELIBERATIONS FOR COMPTON CAMERA DESIGN

In this chapter, the fundamental theories upon which the Compton camera operations are based are discussed. After a brief overview of the basic concepts of photon-matter interactions in Section 2.1, discussion on emission computed tomography is given in Section 2.2. Section 2.3 and Section 2.4 describe the Compton camera basic principles with relevant mathematical models. Different contributions to the Compton camera angular resolution are presented in Section 2.5. Section 2.6 deals with the concept of Compton camera sensitivity. To clarify the impact of system dead time on sensitivity, two models of dead time are introduced in Section 2.7. Section 2.8 provides a discussion on the applicability of different types of radiation detectors in Compton imaging. To understand the basics of Compton camera reconstruction, the list-mode reconstruction method is explained in Section 2.9. Section 2.10 provides an introduction to the structure of GEANT4. How the GEANT4 uses relevant electromagnetic physics principles for its operation is explained in Section 2.11.

2.1 General overview of photon interaction with matter

A gamma photon that enters an absorbing medium can pass through with no interaction at all, or it can interact in some way with the atoms of the medium. If the photon interacts, the interaction may involve either an atomic nucleus or an orbital electron of an atom within the medium. Photon-atom interactions result in ejection of orbital electrons from atoms or in the creation of positron-electron pairs. These electrons in turn can produce additional secondary electrons through ionization events. The electrons thus generated are detected in radiation detectors.

Photon interactions with atomic nuclei may be direct photon-nucleus interactions (photodisintegration) or interactions between the photon and the electrostatic field of the nucleus (pair production). The photon-orbital electron interactions can be between the photon and

either (i) a loosely bound electron or (ii) a tightly bound electron

A loosely bound electron is an electron whose binding energy E_B is very much smaller in comparison with the photon energy E_γ ($E_B \ll E_\gamma$), and an interaction between a photon and a loosely bound electron is usually approximated to an interaction between a photon and a free (unbound) electron.

A tightly bound electron is an electron whose binding energy E_B is comparable to, larger than, or even slightly smaller than the photon energy E_γ. For a photon interaction to occur with a tightly bound electron, the binding energy E_B of the electron must be of the order of, but slightly smaller than the photon energy ($E_B \lesssim E_\gamma$). An interaction between a photon and a tightly bound electron is considered an interaction between a photon and the atom as a whole. Two possible outcomes exist after photon interaction with an atom:

1. The photon is completely absorbed and its energy is transferred to the electrons (photoelectric effect).

2. The photon is scattered with two possible results:

   (a) The resulting photon has the same energy as the incident photon and no electron is released in the interaction (Rayleigh scattering).

   (b) The scattered photon has a lower energy than the incident photon and the energy excess is transferred to an electron (Compton scattering).

The electrons produced in the absorbing medium through photon interactions either deposit their energy to the medium through Coulomb interactions with orbital electrons of the absorbing medium (excitation and ionization losses), or radiate their kinetic energy away through Coulomb interactions with the nuclei of the absorbing medium (radiative loss) (Podgoršak, 2006).

2.2 Emission Computed Tomography

The concept of photon-matter interactions described in Section 2.1 has enormous applications in the branch of medicine known as emission computed tomography (ECT). With millions of imaging procedures being performed each year, ECT has made a great impact on the practice of medicine due to its ability to provide three-dimensional information of radioactivity within an object. This information is typically presented as cross-sectional slices through the patient, but can be freely reformatted or manipulated as required. ECT uses radiation as the emanations to probe the body. Due to the high energy of the gamma rays used (100 keV to 600 keV), the refractive index of the body is essentially unity, therefore the gamma rays travel in straight line paths. Diffraction effects can be ignored to a very high level of accuracy. The gamma rays are sourced within the body and detected by a detector positioned outside the body (Cree, 1994).

There are several potential advantages of performing ECT with the Compton camera compared with the conventional gamma camera that uses a collimator. One potential ad-

vantage is increased sensitivity. Studies suggest that the Compton camera may be able to count one or two orders of magnitude more photons than the conventional gamma camera, resulting in reduced acquisition times. Compton cameras also offer the potential to image more than two tracers simultaneously. Contemplating the research and clinical advancements that could be made possible by multi-tracer imaging are truly exciting (Chelikani *et al.*, 2004; Smith, 2005).

The basic principles of ECT can be described with the attenuation coefficient μ, used for characterization of photon penetration into absorbing media. This parameter depends on the energy E_γ of the emitted photon and atomic number Z of the absorber, and may be defined as the probability per unit path length of a photon having interaction with the absorber.

Consider a slab of absorber material of thickness x placed between a gamma ray source located within a tissue and a detector as shown in Figure 2.1. The absorber decreases the detector signal (intensity) from $I_0(E)$ that is measured without the absorber in place to $I(x, E)$ that is measured with absorber thickness x in the beam. A layer of thickness dx within the absorber reduces the beam intensity by dI and the fractional reduction in intensity, $-dI/I$, is proportional to the attenuation coefficient $\mu(x, E)$ and the layer thickness dx. The relationship for $-dI/I$ can thus be written as follows:

$$\frac{-dI}{I} = \mu(x, E)\, dx, \tag{2.1}$$

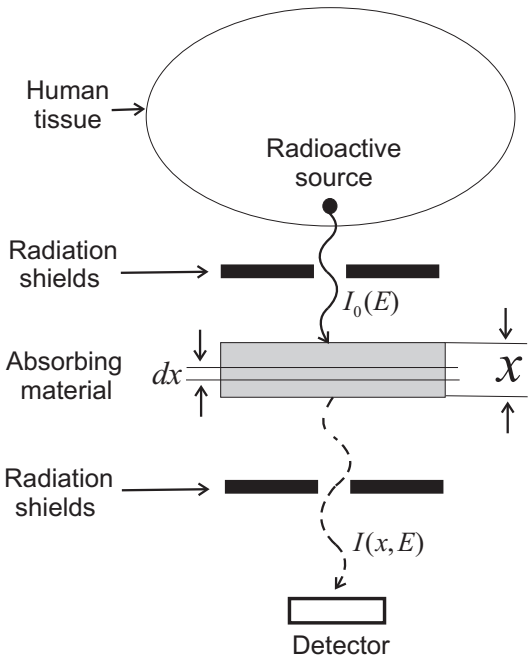

Figure 2.1: Photon attenuation in an absorbing material

Integrating Equation 2.1 with respect to x gives the expression for a monoenergetic

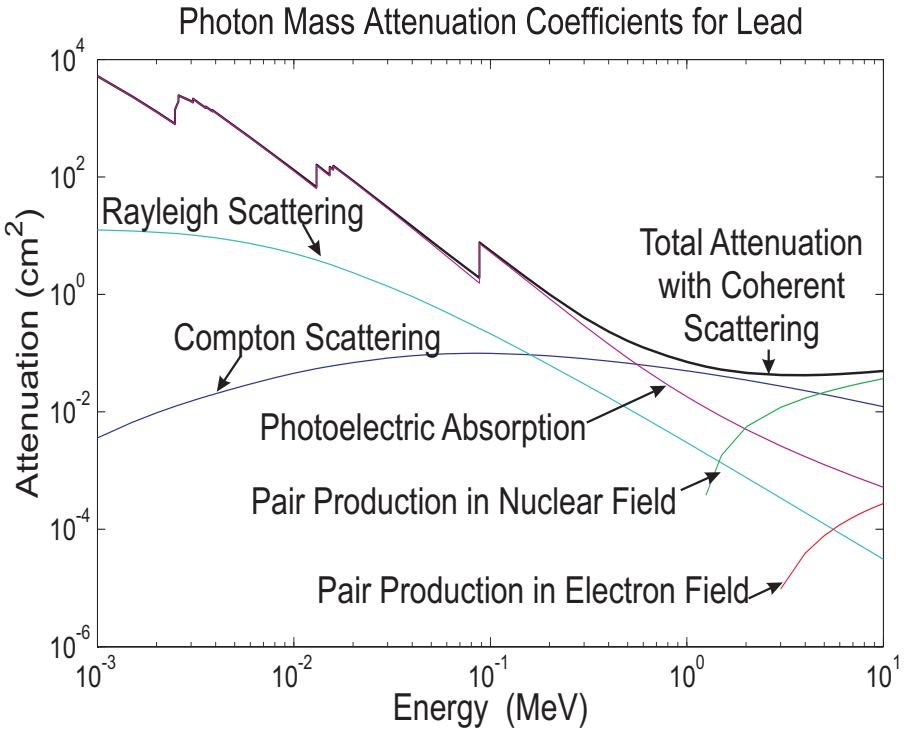

Figure 2.2: Total attenuation cross section for the interaction of photons with lead, and the contribution of each interaction to the total attenuation. (Graph data sourced from NIST's XCOM database (Berger *et al.*, 2010))

photon beam traversing a homogeneous medium with a attenuation $\mu(x, E)$,

$$I(x, E) = I_0(E)\, e^{-\int \mu(x,E)\, \mathrm{d}x}. \tag{2.2}$$

Note that Equation 2.2 is obtained with the consideration that μ, I_0 and I all depend on the gamma ray energy E. A plot of the various contributing interactions to linear attenuation coefficient for lead up to 10 MeV is shown in Figure 2.2. Of the various interactions shown, the most relevant processes to ECT are Compton scattering and photoelectric absorption. These interactions are also the key processes needed for Compton camera operation, hence, detailed descriptions of the interactions and relevant mathematical aspects as to how they affect the Compton camera operations are discussed in the following sections.

2.3 Compton Scattering

For the analysis following, it is convenient to define α to be

$$\alpha = \frac{E_\gamma}{m_0 c^2}, \tag{2.3}$$

where E_γ is the energy of the incident photon and m_0c^2 is the rest energy of the electron, which evaluates to 511 keV.

In 1923 Arthur Compton (1923) assumed the target electron of a material detector to be free and at rest and derived his famous photon scattering equations from the laws of energy and momentum conservation as:

$$\Delta E = E_\gamma - E'_\gamma = E_\gamma \frac{\alpha\,(1-\cos\theta)}{1+\alpha\,(1-\cos\theta)}, \tag{2.4}$$

$$\cos\theta = 1 - \frac{\Delta E}{\alpha\left(E_\gamma - \Delta E\right)}. \tag{2.5}$$

Here ΔE is the energy transferred to the target electron by the incident photon, E'_γ is the energy of the scattered photon and θ is the scattering angle. Unfortunately, in real detector systems the electrons are neither free nor at rest, but bound to their atomic nuclei with non-zero orbital momentum. In 1929 Jesse Du Mond (1929) interpreted a measured broadening of the Compton spectra as Doppler broadening induced by the velocity of the electrons (Zoglauer and Kanbach, 2003). Details of Doppler broadening as it concerns our application is discussed in Chapter 3.

The amount of energy transferred to the recoil electron ranges from almost zero for $\theta \approx 0°$ (grazing collisions) up to some maximum value at $\theta = 180°$. At $\theta = 180°$, the incident photon is backscattered toward the original direction, whereas the electron recoils along the direction of incidence and the energy transferred can be derived as:

$$\Delta E = E_\gamma \frac{2\alpha}{1+2\alpha}. \tag{2.6}$$

Equation 2.6 represents the maximum energy that can be transferred to the electron in a single Compton scattering, and is commonly known as the Compton edge. Figure 2.3 shows a schematic diagram of a Compton scattering between an incident gamma ray photon and an atomic electron. In this figure, a certain photon with an incident energy E_γ scatters off a free electron through an angle θ with respect to its incident direction and with a reduced energy E'_γ. The electron also deflected with an increased energy ΔE through an angle φ with respect to the incident photon direction.

The Compton scattering process is utilized in determining the directional information of incident gamma photons in Compton cameras. To achieve directional localization, part of the energy of the incident photon must be transferred to a loosely bound electron of the scatterer, which recoils and is ejected from its atom, and the photon is deflected through a scattering angle θ with respect to its original direction. If the photon still has enough energy left, the process may be repeated. The scattered photon is then detected by the second plane detector known as the absorber where it is completely absorbed. The energy, position and time measurements from each of the detectors are combined to reconstruct the initial photon direction.

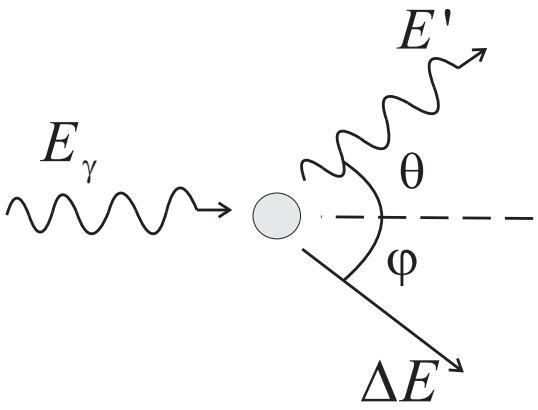

Figure 2.3: Compton scattering between an incident photon and an orbital electron (recoil electron)

2.3.1 The Compton scattering probability

The probability for a single Compton scattering followed by an escape of the scattered photon was derived by Oskar Klein and Yoshio Nishina in 1929 (Klein and Nishina, 1929), a few years after the Compton scattering discovery. This is referred to as the Klein-Nishina differential cross section. The Klein-Nishina differential cross section for an unpolarized electromagnetic radiation scattering off an unbound electron is uniquely given by the energy and angle relationship:

$$\frac{d_e\sigma^{KN}}{d\Omega} = r_0^2 \left(\frac{1}{1+\alpha\,(1-\cos\theta)}\right)^2 \left(\frac{1+\cos^2\theta}{2}\right) \left(1+\frac{\alpha^2\,(1-\cos\theta)^2}{\left(1+\cos^2\theta\right)\,(1+\alpha\,(1-\cos\theta))}\right), \tag{2.7}$$

where r_0 is the classical electron radius. Equation 2.7 is a measure of the probability $d_e\sigma^{KN}$ that an incident gamma ray will be deflected into the solid angle $d\Omega$ by a free electron. The validity of the above equation occurs when the incident photon energy is much greater than the binding energy of the target electron. Figure 2.4 shows the graphical representation of the relative probability of Compton scattering at different angles per unit of solid angle. This figure reflects the relative number of scattered photons that would be recorded by a detector of fixed area as it is moved about a fixed distance from the scattering object at different angles relative to the incident photons assuming attenuation and secondary scattering are ignored.

As scattering predominates, the total Compton scattering cross-section can then be evaluated as the integral of Equation 2.7 over all possible solid angles,

$${}_e\sigma^{KN} = \int_0^{\pi} \frac{d_e\sigma^{KN}}{d\Omega} 2\pi \sin\theta\, d\theta \tag{2.8}$$

$$= 2\pi r_0^2 \left[\frac{2\,(1+\alpha)^2}{\alpha^2\,(1+2\alpha)} + \frac{\ln\,(1+2\alpha)}{\alpha}\left(\frac{1}{2}-\frac{1+\alpha}{\alpha^2}\right) - \frac{1+3\alpha}{(1+2\alpha)^2}\right]. \tag{2.9}$$

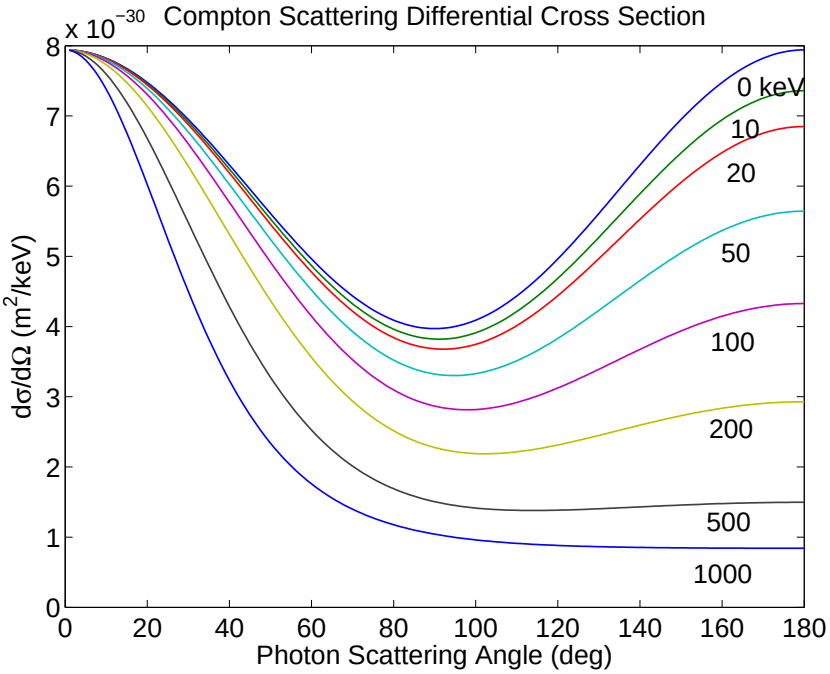

Figure 2.4: Compton scattering collision cross section of gamma rays at various incident energies scattering off free electrons at different angles. (Figure adapted from (Cree, 1994), used with permission)

Equation 2.9 is independent of atomic number Z of the detector, since in the Compton theory the electron is assumed free and stationary, implying that the electron's binding energy to the atom is assumed to be negligible.

2.3.2 Effect of electron binding on Compton scattering

Consider a homogeneous elemental scattering medium with a density of electrons defined as

$$n_e = \frac{N_A \rho Z}{A}, \tag{2.10}$$

where $N_A = 6.02 \times 10^{23}$ mol^{-1} is Avogadro's number, ρ is the density, Z is the atomic number and A is the atomic mass of the medium. Assuming that this medium is not affected by electron binding effects, all electrons will be free and participate equally in Compton scattering. The Compton linear attenuation coefficient for this system of free electrons can then be expressed as:

$$\mu_c = \frac{N_A \rho Z}{A} {}_e\sigma^{KN} \approx \frac{N_A \rho_e \sigma^{KN}}{2}, \tag{2.11}$$

where ${}_e\sigma^{KN}$ is the Compton electronic cross section. The approximation of the ratio Z/A to $1/2$ in Equation 2.11 implies a small variation in Compton linear attenuation coefficients for different elements. However, different shell electrons are have different binding energies which make them participate differently to Compton scattering.

A variety of theories have been proposed to account for the effects of electronic binding energy on Compton atomic cross sections (${}_a\sigma^{KN}$). Most notable is the method developed by Hubbell *et al.* (1975) from the National Institute for Science and Technology (NIST) in Washington, USA. This group treated the binding energy corrections to the Klein-Nishina relationships in the impulse approximation taking into account all orbitals electrons of the scattering atom. They achieved their success by applying a multiplicative correction function $S(x, Z)$, referred to as the incoherent scattering function, to the Klein-Nishina atomic cross sections as follows:

$$\frac{d\sigma_{inc}}{d\Omega} = \frac{d_a\sigma^{KN}}{d\Omega} S(x, Z), \tag{2.12}$$

where $x = (\sin\theta/2)/\lambda$ is defined as the momentum transfer variable with λ, the wavelength of the incident photon. The inclusion of $S(x, Z)$ into Equation 2.11 gives the modified expression of Compton linear attenuation coefficient

$$\mu_c = \frac{N_A \rho Z}{A} \sigma_{inc}. \tag{2.13}$$

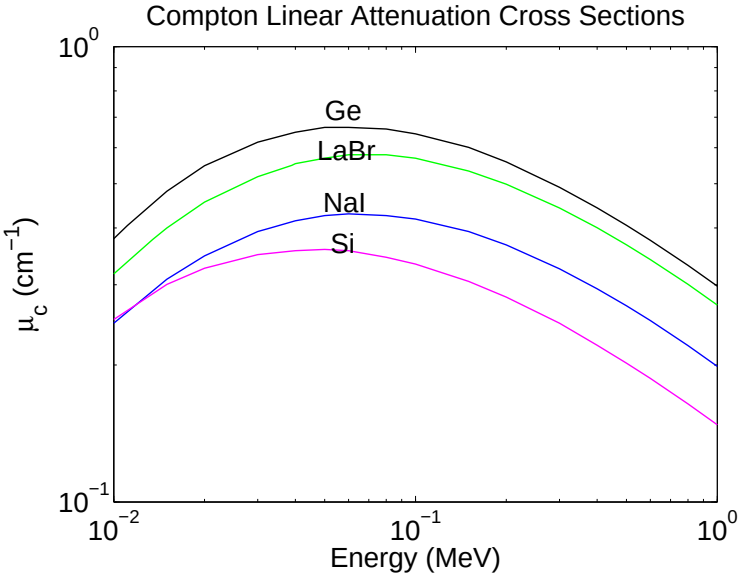

Figure 2.5: The linear attenuation coefficient due to Compton scattering for silicon, germanium, lanthanum bromide and sodium iodide

Figure 2.5 shows graphs of the Compton linear attenuation coefficient as a function of the photon energy for selected radiation detectors. It can be observed from the figure that the probability of Compton scattering between photons and electrons of these materials increases gradually as the photon energy increases up to about 100 keV and then falls off at higher energies. Figure 2.5, however, provides no information about the suitability of the materials as Compton camera scatterers. The materials' potential suitability as Compton camera scatterers can be determined by plotting the Compton to total interaction ratios, which are illustrated in Figure 2.6. According to Figure 2.6, silicon is the best candidate

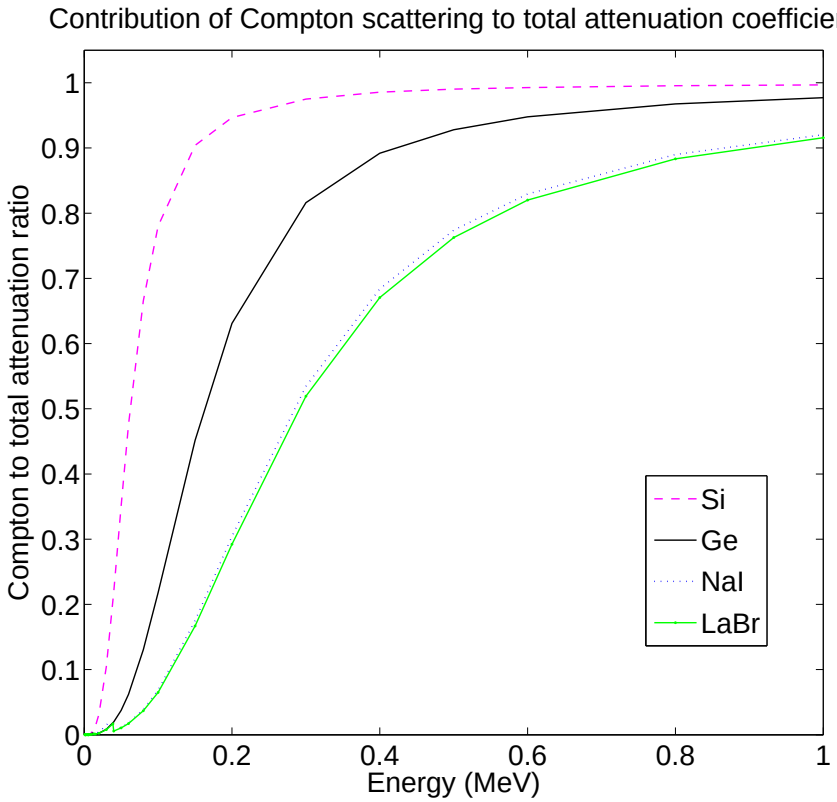

Figure 2.6: Compton to total cross section ratio as a function of energy in various for selected radiation detectors

for the scatterer considering only the Compton scattering probability.

2.4 Photoelectric Effect — a tool for position localization

To be accepted for image reconstruction, a Compton scattered gamma photon from the scatterer must fall into the solid angle subtended by the Compton camera absorber, and interact with a tightly bound orbital electron of the absorber via the photoelectric effect. The photon disappears and the orbital electron (photoelectron) is ejected with a kinetic energy E_K, equal to the difference between the scattered photon energy E'_γ and the binding energy E_B of the electron shell from which it was ejected. Cherry *et al.* (2003) suggest that the ejection of a K-shell electron is four to seven times more likely than ejection of an L-shell electron when the energy requirement of the K-shell is met, depending on the absorber element. This ejection creates a vacancy in the orbital electron shell, which is quickly filled through the capture of an electron and/or rearrangement of electrons from other shells of the atom. This may result in the emission of one or more characteristic x rays or Auger electrons which are generally reabsorbed near the emission point. The quantity of the energy deposited, position of interaction and time of the photoelectric interaction are measured and

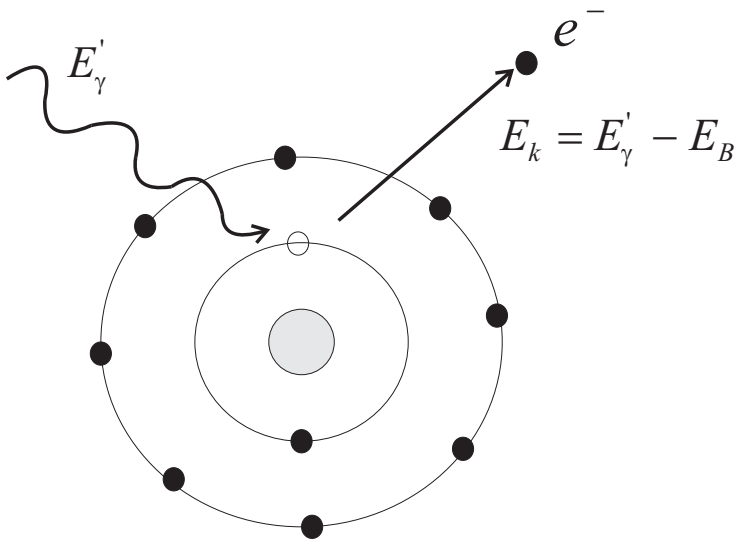

Figure 2.7: Schematic diagram of the photoelectric effect. A photon with energy E'_γ interacts with a K-shell electron. The photon is absorbed completely and the K-shell electron is ejected as a photoelectron from the atom with a kinetic energy $E_k = E'_\gamma - E_B$

stored for further analysis. A schematic diagram of the photoelectric interaction between a photon of energy E'_γ and a photoelectron is shown in Figure 2.7

2.4.1 Photoelectric cross section

The probability that the photoelectric effect will occur depends on the atomic number of the absorbing material Z and the energy of the incident photon E_γ (or scattered photon energy E'_γ for the case of Compton camera). At present, an exact analytical expression for the photoelectric probability has not been found. However, a rough approximation of Z and E_γ dependence on the photoelectric linear cross section μ_p can be written as (Knoll, 2000):

$$\mu_p = k\frac{\rho Z^n}{A\left(E_\gamma\right)^{3.5}}, \tag{2.14}$$

where the exponent n varies between 4 and 5, and k is a constant that depends on the shell involved, assuming a medium with atomic mass A, atomic number Z and density ρ. The severe dependence of photoelectric linear cross section (or photoelectric absorption probability) on atomic number Z in Equation 2.14 is the primary reason for the preponderance of high Z materials for Compton camera absorbers. A graph of photoelectric linear attenuation coefficient μ_p as a function of the incident photon energy E_γ for some detector materials is shown in Figure 2.8. In the low-energy region of the graph, absorption edges (discontinuities) in curves appear at photon energies that correspond to the binding energies of specific electron shells of the absorber atom. Sharp edges correspond to K absorption edge, whereas smooth edges correspond to L, M, etc, absorption edges.

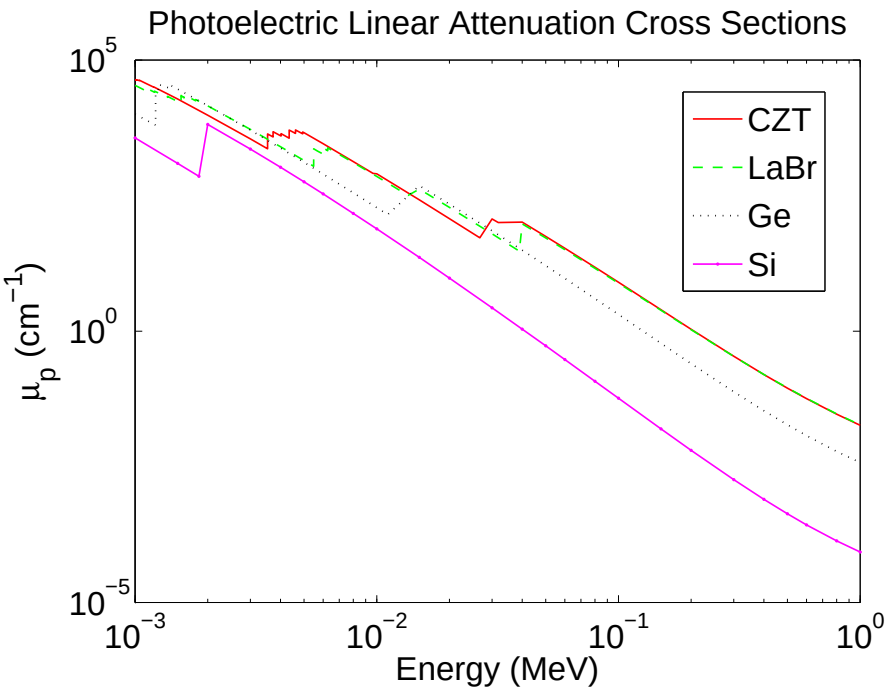

Figure 2.8: Photoelectric linear attenuation for silicon, germanium, lanthanum bromide and cadmium zinc teluride

2.5 Angular resolution

The accuracy of the Compton camera is based on the accuracy with which the cone parameters are determined from the measurements of the positions and the energies deposited in the detectors. For instance, measurement uncertainties to know the true positions and energies cause a spread about the true location of a point source. Thus the angular deviation of the reconstructed cone from the true source location characterizes the imaging performance of Compton cameras, and is evaluated using the angular resolution measure (ARM), $\Delta\theta$, which refers to the uncertainty in measuring the true scattering angle. In real Compton cameras, ARM can be evaluated with the following expression (Zoglauer and Kanbach, 2003; Watanabe *et al.*, 2005; Seo *et al.*, 2010):

$$\Delta\theta = \theta_{Geom} - \theta_{Comp}, \tag{2.15}$$

where θ_{Geom} is the scattering angle defined by the known position of the gamma ray source and the hit (or interaction) positions, and θ_{Comp} is the scattering angle computed with the Compton scattering formula. The full width at half maximum (FWHM) of the distribution of Equation 2.15 gives the angular resolution of the Compton camera. Major contributions to the Compton camera angular resolution can be identified as follows:

- the contribution of limited energy resolution of the scatterer,
- the inherent resolution given by Doppler broadening,

- the geometric contribution which is related to the determination of the scattered photon track.

Measurement errors in energy resolution and Doppler broadening cause the Compton scattering angle to be uncertain. These two parameters are significantly influenced by the choice of the selected radionuclide and detector material. The geometric contribution however, depends on the detector layout and the interaction position uncertainties of the detectors. The combined FWHM spread caused by these three factors combine can be computed in principle from the following quadrature addition (Singh, 1983; Du *et al.*, 2001):

$$\tan^2(\Delta\theta) = \tan^2(\Delta\theta_e) + \tan^2(\Delta\theta_d) + \tan^2\left(\Delta\theta_g\right), \tag{2.16}$$

where $\Delta\theta_e$ is the scatterer energy resolution contribution, $\Delta\theta_d$ is the Doppler broadening contribution and $\Delta\theta_g$ is the geometric contribution to the angular resolution. Note that the energy resolution of the absorber is not often used to calculate the uncertainty in angular resolution. It is rather considered useful for separating the true Compton scattering events from the background events within a desired energy window since it does not limit the angular resolution significantly as the scatterer energy resolution does. Hence it can be classified as of secondary importance in the image formation (Studen, 2005a). More details of the contributions of angular resolution $\Delta\theta$ in Equation 2.16 are presented in the following.

2.5.1 The contribution of the energy resolution to the angular resolution

The directional localization of a radiotracer distribution with a Compton camera involves the calculation of scattering angles from the measured energies. Consequently, errors in the energy measurements manifest as uncertainties in the calculated scattering angles. An expression for the uncertainty $\Delta\theta_e$ in the Compton scattering angles due to energy measurement errors can be obtained by taking the derivative of the Compton scattering equation (Equation 2.5) to yield:

$$\Delta\theta_e = \frac{m_0c^2}{\sin\theta\left(E_\gamma - E_s\right)^2}\Delta E_S, \tag{2.17}$$

where ΔE_s is the FWHM uncertainty in measuring the energy deposited in the scatterer E_s. The $\sin\theta$ term in the denominator results in a large uncertainty for small angle scattering as illustrated in Figure 2.9 for three incident photon energies. The E_γ^2 term in the denominator indicates that the uncertainty decreases rapidly with increase in incident photon energy. This is also observed in Figure 2.9 which shows that it is easier to achieve good angular resolution at 300 keV and above. Achieving a high angular resolution at 140.5 keV would require a state-of-the-art detector as the scatterer or rigorous accounting of the angle uncertainty due to the energy measurement errors in the reconstruction algorithm. The angular uncertainty, $\Delta\theta_e$ in Equation 2.17 has two contributions in reality. One is the energy resolution of the scatterer, and the other is Doppler broadening (a fact that is not accounted for in the equation). The energy resolution is limited by the statistical noise and the electronic

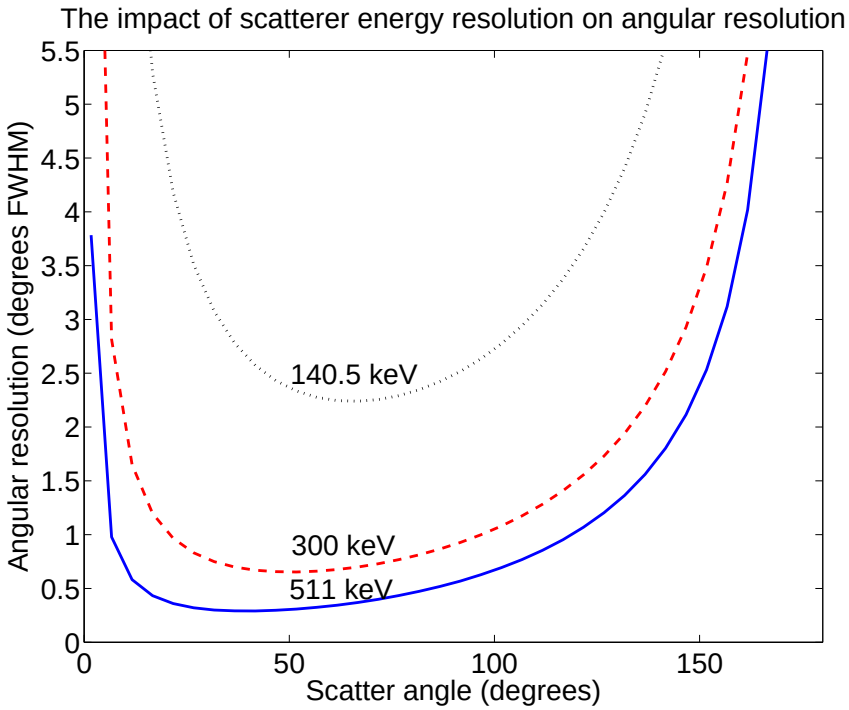

Figure 2.9: The contribution of the energy resolution to total angular resolution

noise within the scatterer. The statistical noise is related to the fluctuation in the number of discrete charge carriers generated by the interacting electron. The electronic noise is related to the signal noise generated in the course of signal processing. The latter can be minimized by using suitable electronics, but the former represents an irreducible intrinsic limit that will always be present in the detector signal no matter how perfect the remainder of the system is made.

2.5.2 The contribution of Doppler broadening to the angular resolution

In Equation 2.17, it was assumed that the scattering angle uncertainty can be calculated with only the energy resolution. However, when considerations are made on the reality that the electrons spin around the atomic nucleus, the impossibility of realizing the accurate prediction of the total Compton camera angular uncertainty with only Equation 2.17 becomes obvious. This is because, for a given value of energy measured in the scatterer (even if no measurement error is made), there is a distribution of angles that could have occurred; and at the energy level of the conventional SPECT (140 keV), this distribution of angles is substantial. This phenomenon is referred to as Doppler broadening. The problem of Doppler broadening is complicated by the fact that there does not seem to exist any direct relationship between the kinetic energy of the recoil electron and the scattering angle when the electron spin is considered. Hence, the most feasible solution is to adopt the concept of electron momentum distribution which can be described in the context of Compton camera

in the following way (Ribberfors, 1975).

The interacting electrons of the scatterer have a non-zero momentum distribution which depends upon the characteristics of the electron shell structures associated with the detector material. This distribution changes the kinematics and the relationship between the scattering angle and the energy transferred to the recoil electron. The Compton scattering formula (Equation 2.5) which assumes that the recoil electron is free and at rest, must then be modified to include the effects of the electron motion and binding, leading to additional uncertainty in calculating the scattering angle.

Ribberfors (1975) incorporated the electron's motion and binding effects into the Compton kinematics equation in a consistent way by using the relativistic impulse approximation. He achieved this feat by treating the motion of the electron as a plane wave so that the target potential is assumed to be constant during the collision. This implies that the energy transfer from the photon to the electron has to be at least one order of magnitude higher than the binding energy of the respective electron. Following their work, Ordonez *et al.* (1997) showed that the angular uncertainty due to Doppler broadening is non-negligible for Compton cameras intended for medical applications. The group accounted for the effects of the electron's non-zero pre-collision energy and momentum with the approximate formula:

$$P_z = -m_0 c \frac{E_\gamma - E'_\gamma - \alpha E_\gamma (1 - \cos\theta)}{\sqrt{E_\gamma^2 + E_\gamma'^2 - 2E_\gamma E'_\gamma \cos\theta}}. \tag{2.18}$$

P_z was defined as the projection of the electron's pre-collision momentum on the momentum transfer vector of the incident photon by the group. Accordingly, the Klein-Nishina formula for the differential cross section of Compton scattering was also modified as follows:

$$\frac{d^2\sigma_n}{d\Omega dE'_\gamma} = \frac{m_0 r_0^2}{2E_\gamma}\left(\frac{E_C}{E_\gamma} + \frac{E_\gamma}{E_C} - \sin^2\theta\right)\frac{E'_\gamma}{\sqrt{E_\gamma^2 + E_\gamma'^2 - 2E_\gamma E'_\gamma \cos\theta}} J_n(P_z), \tag{2.19}$$

where E_C is the Compton energy defined by Equation 2.4, $J_n(P_z)$ is the Compton profile for the nth sub-shell of the target atom and r_0 is the classical electron radius. Equation 2.19 is referred to as the double-differential cross section (DDCS), differential in the energy and direction of the scattered photon. DDCS is thus a bi-variate probability distribution function of the energy and direction of the scattered photon.

If the Compton profiles are separated out in terms of the valence and core electrons, the variation of the electron momentum due to Doppler effect is more clearly evident. This is illustrated in Figure 2.10 for the case of crystalline silicon. The long tail of the total profile is due to the core electrons and gives a poor estimate of the peak location of the energy spectrum whereas the peaked valence electron profile gives a better estimate of the peak location of energy spectrum (Brusa *et al.*, 1996; LeBlanc, 1999). The effect of the spread in the electron's momentum and energy by Doppler broadening is shown in Chapter 3 to

cause a blurring of the Compton camera image.

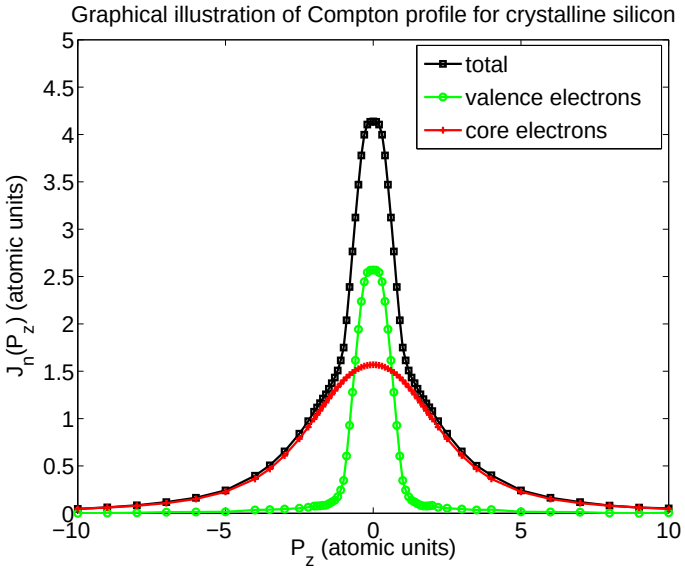

Figure 2.10: Compton profiles for crystalline silicon showing total, and contributions from valence electrons and core electrons

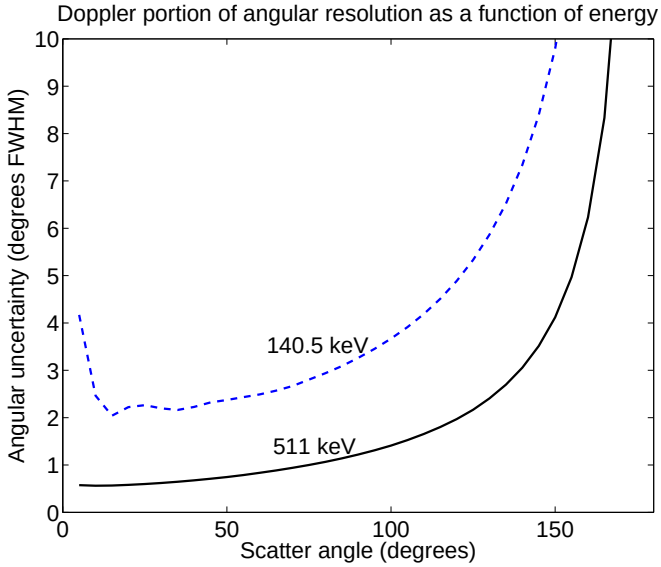

Figure 2.11: The contribution of Doppler broadening to the angular resolution at 140.5 keV and 511 keV

The contribution of Doppler broadening to the total angular resolution as a function of scattering angle is shown in Figure 2.11. The graph curves represent the FWHM of the Compton profile at 140.5 keV and 511 keV. It can be seen in Figure 2.11 that Doppler broadening dominates the Compton camera angular resolution at 140.5 keV more than at 511 keV. The figure also shows that the Doppler contribution to angular resolution varies

strongly with scattering angle such that it becomes worse for larger angles. This is an important fact that must be considered when designing a Compton camera model for clinical purposes. A GEANT4 study on how Doppler broadening affects the performance of Compton cameras intended for clinical purposes is presented in Chapter 3.

2.5.3 The contribution of geometric uncertainty to the angular resolution

Besides the uncertainties due to the energy resolution and Doppler broadening, the geometrical uncertainty is a severe limitation in determining the axis of the back-projected cone in Compton cameras. The reason lies on the fact that the uncertainty to estimate the 'true' positions of interactions in the detectors transforms into uncertainty in the placement of the back-projected cone. Two major contributions to the geometric uncertainty of the Compton camera are commonly reported in the literature (Ordonez *et al.*, 1999; Studen, 2005a). One is the finite spatial resolution of the detectors, and the other is the extended geometry of the detectors. The former relates to the pixel size or the statistical collections of the scintillation photons by the photomultipler tubes (PMTs), as well as the depth of resolution of the detector; the latter relates to the placement and geometric orientation of the detectors. A detailed analytical study on the geometric uncertainty of Compton cameras has been presented by Ordonez *et al.* (1999), hence discussions on this subject herein is limited to the Compton camera design described in this thesis, namely the two parallel planar detector design.

Consider a gamma ray emitted from a source located at origin $\vec{\mathbf{r}}$ (Figure 2.12) and Compton scattered at a point $\vec{\mathbf{r}}_\mathbf{S}$ in the scatterer, and the scattered gamma ray is fully absorbed at a point $\vec{\mathbf{r}}_\mathbf{A}$ in the absorber. From the vectors that connect these points of interactions in Figure 2.12, it is easy to derive the following equation:

$$\cos\theta = \frac{(\vec{\mathbf{r}} - \vec{\mathbf{r}}_\mathbf{S}) \cdot (\vec{\mathbf{r}}_\mathbf{S} - \vec{\mathbf{r}}_\mathbf{A})}{|\vec{\mathbf{r}} - \vec{\mathbf{r}}_\mathbf{S}|\,|\vec{\mathbf{r}}_\mathbf{S} - \vec{\mathbf{r}}_\mathbf{A}|}. \tag{2.20}$$

In Equation 2.20, it is obvious that the emission point must lie within the surface of a cone. If the angular resolution $\Delta\theta_g$ is taken into account, then the shift of the cone axis will be derived from the spatial resolutions of the scatterer and the absorber, as well as the detector arrangements, which correspond to $\Delta r_S\,(\Delta x_S, \Delta y_S, \Delta z_S)$ for the scatterer spatial resolution, $\Delta r_A\,(\Delta x_A, \Delta y_A, \Delta z_A)$ for the absorber spatial resolution, R_1 for the source-to-scatterer distance, R_2 for the distance between detector interaction points and R_C for the scatterer-to-absorber distance. In real Compton cameras, the effect of the spatial resolution is evaluated by utilizing the centre positions of the detector pixels in which the interactions occurred or by blurring the detection positions with distances sampled from Gaussian distributions whose widths (FWHM) correspond to the specified spatial resolutions. The direction vectors are then calculated with the use of the modified interaction positions and the known source position using Equation 2.20.

On the other hand, an analytical expression to calculate the geometrical contribution to

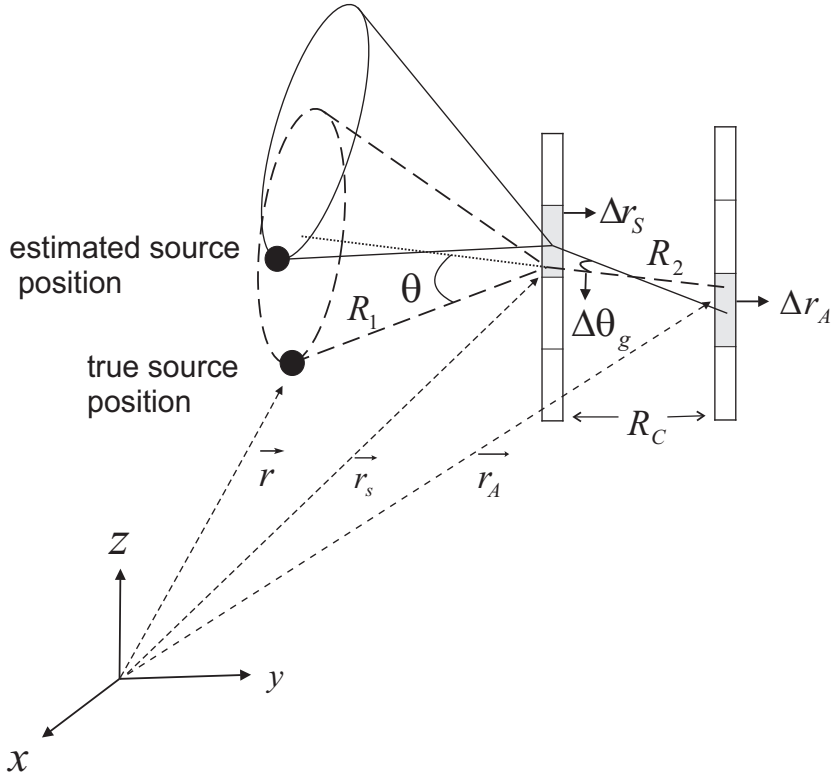

Figure 2.12: An illustration of how the use of detector pixel centres can affect the placement of the reconstructed Compton camera cone

angular resolution is given by Ordonez *et al.* (1999) as:

$$\Delta\theta_g = \frac{\Delta r_S}{R_1}\sqrt{1+\zeta^2\left(1+\beta^2\right)+2\zeta\cos\theta}, \tag{2.21}$$

where $\zeta = R_1/R_2$ and $\beta = \Delta r_A/\Delta r_S$. The parameter β denotes the spatial resolution of the absorber relative to that of the scatterer. In Equation 2.21, matched resolutions represent the condition, $\beta = 1$ or $\Delta r_S = \Delta r_A$. However, the spatial resolutions of most proposed Compton cameras are not always matched but are such that $\beta \geq 1$. Equation 2.21 also suggests that for a hypothetical Compton camera with the dimensions $\Delta r_S = 1$ mm, $\Delta r_A = 2$ mm and $R_1 = 10$ cm, the effect of the distance between detector interaction points on the angular resolution can be represented as in Figure 2.13(a). The largest separation (1000 cm) in Figure 2.13(a) exhibits asymptotic behaviour with respect to R_2. In fact, even at 30 cm, the angular resolution is already close to the asymptotic value for all scattering angles. Therefore, the detector separation need not be made too large in order to obtain an optimal angular resolution (Ordonez *et al.*, 1999). On the other hand, with the source-to-scatterer R_1 varied and R_2 fixed at 10 cm, the effect of R_1 on the angular resolution is shown in Figure 2.13(b). Figure 2.13(b) suggests a rapid increase in the angular resolution for sources close to the scatterer. In general, the variation in R_1 is similar to that observed for R_2.

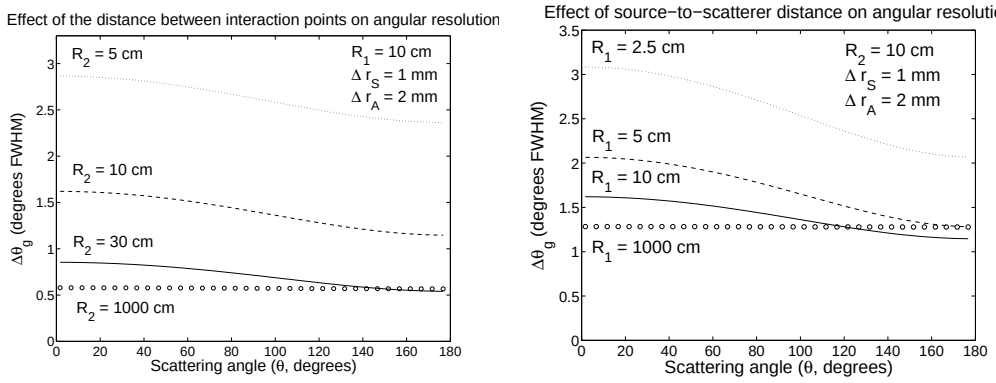

(a) (b)

Figure 2.13: (a) Angular resolution for a Compton camera with matched spatial resolutions (FWHM), $\Delta r_S = \Delta r_A = 1$ mm to 4 mm, source-to-scatterer distance $R_1 = 10$ cm and scatterer-to-absorber distance $R_2 = 5$ cm. (b) Angular resolution for a Compton camera with matched spatial resolutions (FWHM), $\Delta r_S = \Delta r_A = 1$ mm to 4 mm, source-to-scatterer distance $R_1 = 10$ cm and scatterer-to-absorber distance $R_2 = 10$ cm.

2.5.4 Position uncertainty and optimization considerations

In the image reconstruction of Compton camera data, the position uncertainty of the source located at a distance R_1 from the scatterer is a more meaningful constraint than the angular uncertainty. Assuming that each detector event conical surface has the same angular uncertainty, the point where all cones intersect (the source position) is approximately circular with a diameter of

$$\Delta x = R_1 \Delta\theta, \tag{2.22}$$

where Δx is the position uncertainty of the source and is approximately equal to the spatial resolution of the image generated with the conditions stated above. Here $\Delta\theta$ is the total angular uncertainty given by Equation 2.16 (Mundy and Herman, 2010; Ordonez *et al.*, 1999). Figure 2.14(a) shows the position uncertainties predicted by the major contributions to the angular resolution for a hypothetical Compton camera with the scatterer energy resolution $\Delta\theta_e = 1$ keV, scatterer pixel resolution $\Delta r_S = 1$ mm, absorber pixel resolution $\Delta r_A = 2$ mm source-to-scatterer distance $R_1 = 10$ cm and scatterer-to-absorber distance $R_C = 5$ cm at 140.5 keV. The figure suggests that the camera can achieve FWHM position uncertainties of approximately 8 mm to 10 mm for scattering angles between 20° and 100° for a point source object located 10 cm in front of the scatterer. A similar graph for the total position uncertainty is shown in Figure 2.14(b) for 511 keV with $\Delta\theta_e$ adjusted to 2 keV. This time, the figure predicts FWHM position uncertainties of about 4 mm to 5 mm for scattering angles between 20° and 100° for all the uncertainty contributions combined. If a Compton camera with the above configurations can achieve these results in reality, its performance would be rated as excellent! Nevertheless the calculation of the figures in both cases is based on the knowledge of the electron momentum. Note that of all the variables in Equa-

tion 2.18, only two (E_γ and E'_γ) are either known or can be measured. Therefore, unless the electron momentum is known, measured, or estimated, the scattering angle cannot be calculated unambiguously. The ambiguity in the calculation of the scattering angle is a crucial concern in the actual implementations of the Compton camera in medical applications because Equation 2.18 cannot be used to obtain the Compton scattering angle, the best that can be done is to use the Compton scattering formula, Equation 2.5 (Ordonez *et al.*, 1997).

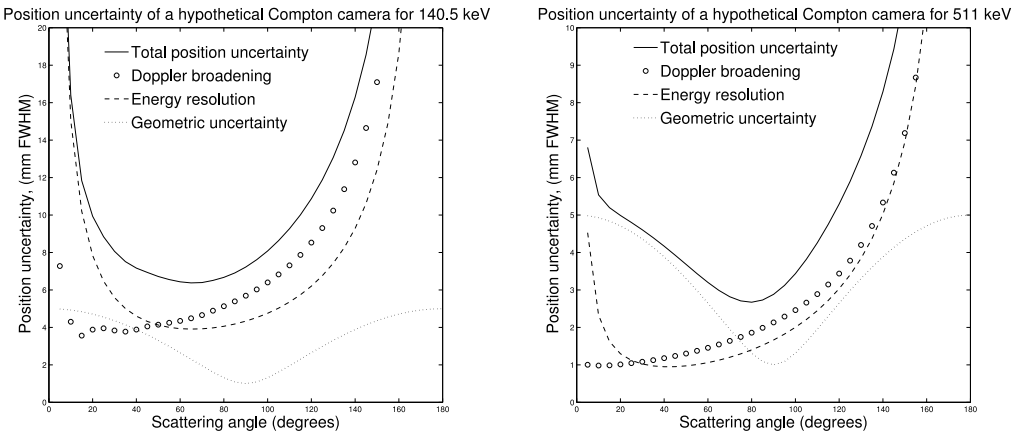

(a) (b)

Figure 2.14: The various contributions to total angular resolution of uncertainty.

It is obvious in Figure 2.14(a) that the geometrical effects are small compared to the energy resolution and Doppler broadening. The energy resolution dominates the position uncertainty at lower scattering angles (<50°), whereas Doppler broadening dominates the position uncertainty for higher scattering angles (>50°). Based on this, the sensitivity of the system can be increased by increasing the surface areas of the detectors without significant sacrifice in position resolution. It is also clear that any possible reduction in the energy resolution of the scatterer below 1 keV will do little to improve the overall position uncertainty due to the Doppler limit at 140.5 keV. On the other hand, the geometry effect contributes the largest fraction of the overall position uncertainty for low scattering angles (<70°) at 511 keV because of the reduction in the effects of the energy resolution and Doppler broadening. Absorbers with higher Z materials and good spatial resolution could then be used to limit photon penetration and subsequently reduce the geometric uncertainty component. Now given that the geometric uncertainty is easy to manipulate, the true physical limits on position uncertainty for a Compton camera system at a given radioisotope energy is set by the Doppler broadening effect and limiting energy resolution.

2.6 Sensitivity

The Compton camera sensitivity relates to its ability to produce a usable signal from photon interactions in the two plane detectors. Photon counts are acquired in a coincidence counting mode between the plane detectors with time parameter as the physical observable. The time window should therefore be reasonably small to discriminate random coincidence events, and at the same time, not so small to discriminate the good events as that could lead to poor photon counting. Poor photon statistics have serious implications for image reconstruction. Reconstruction algorithms often fail to produce reliable information on source images when the signal-to-noise ratio is small. Direct reconstruction algorithms are, in particular, noted for poor reconstruction in noisy situations.

A good template for the Compton camera sensitivity was given by LeBlanc (1999) in the following way. To be counted as part of good photon history or event, a photon emitted by a source must

- travel within the solid angle range of the scatterer
- undergo a Compton scattering in the scatterer
- escape from the scatterer following the Compton scattering
- the scattered photon must fall into the solid angle range of the absorber
- and undergo full photoelectric absorption in the absorber.

Ideally, the scatterer and absorber must be able to provide information on the deposited energy, time and positions of interactions. With this information, a time coincidence mode and an energy criterion are applied to ensure that the two interactions observed are caused by a single photon.

The above details given for a successful photon history relates to five efficiencies which can be maximized for optimal Compton camera sensitivity. The first term relates to the geometric efficiency, which can be increased by increasing the surface area of the scatterer and/or decreasing the source-to-scatterer distance (a fact that is not evaluated in this thesis). The second term is related to the Compton efficiency of the scatterer. Multiple Compton scattering events in the same scatterer pixel can be allowed in the sensitivity analysis since there is no way of filtering them out in real situations. The third term includes the effect of self-attenuation of the scattered photon within the scatterer, which depends on the scatterer thickness, material characteristics and scattered photon energy. The fourth term is a function of the overall camera geometry, and can be optimized by reducing the scatterer-to-absorber distance and/or maximizing the absorber surface area. The fifth term relates to the intrinsic peak efficiency of the absorber. This component strongly depends on the energy of the scattered photon. It can be maximized by choosing high Z materials and increasing the absorber thickness.

In addition to the above photon event criteria that must be met, the Compton camera sensitivity also depends on the inherent detector noise, and depending on the detector design, the protective material surrounding the sensitive volume of the detector. For the first case, a certain minimum amount of energy deposition is necessary for the signal to be usable. This lower limit is determined from the noise from the detectors and the associated electronics. The noise appears as a fluctuating voltage or current at the camera output. For the second case, the material that covers the entrance window to the sensitive volume must allow only photons with sufficient energy to penetrate its thickness. The thickness thus, sets a lower limit on the energy that can be detected.

It follows from the above that the Compton camera sensitivity may be defined as the percentage of the photon events that produced usage reconstruction information in a fixed set of photon histories (Chelikani *et al.*, 2004). The evaluations of the above efficiencies to optimize the Compton camera is a significant part of this thesis.

2.7 Dead time

Depending on the camera design, information on the energy of the radiation may or may not be preserved as the signal is being processed. This is because the amount of ionization caused by radiation in the detectors is collected as the integral of the deposited energy (electrical pulse) with respect to time. This signal integration time is of great importance in data acquisition (DAQ). It relates to the finite time required by the detector to process an event, which is known as the dead time. Depending on the type, a detector may or may not remain sensitive to other events during this period. If the detector is insensitive, any further events arriving during this period are lost. But if the detector retains its sensitivity, the second event may pile-up on the first resulting in the distortion of the signals and subsequent loss of information from both events. These losses affect the observed count rates and distort the time distribution between the arrival of the events so that events from a random radioactive source no longer have the expected Poissonian time distribution. To avoid large dead time effects, photon count rate should be kept sufficiently low such that the probability of a second event occurring during the dead time is small (Leo, 1994).

When calculating the effects of dead time, the entire camera system must be taken into account. Each detector component of the Compton camera system has its own dead time. In some cases the limiting time may be set by processes in the camera's detectors, and in other cases the limit may arise in the associated electronics. However, combining the dead time effects often becomes difficult when the several elements have comparable dead times. Consequently, a simple method for combining the dead time effects in such cases does not exist at present (Knoll, 2000; Leo, 1994).

2.7.1 Types of dead time

Two models of dead time behaviour have come into common usage: paralyzable and non-paralyzable dead time models. In the paralyzable case, the arrival of the second event during the dead time period extends this period by adding its dead time τ starting from the moment of its arrival. This occurs in detector elements which remains sensitive during the dead time. Thus if the event rate is sufficiently high, events can arrive such that their respective dead time periods all overlap, resulting to a prolonged period during which no event is accepted. The element is thus paralyzed. The nonparalyzable case, in contrast, corresponds to an element which is insensitive during the dead time period. The arrival of a second event during this period simply goes unnoticed and after a time τ the element becomes active again. In Figure 2.15, a constant dead time τ is assumed to follow each true event that occurs during the active period of the detector. The nonparalyzable detector records four counts from the six true events. In contrast, the paralyzable detector, shown along the top line of Figure 2.15 records only three counts for the six true events.

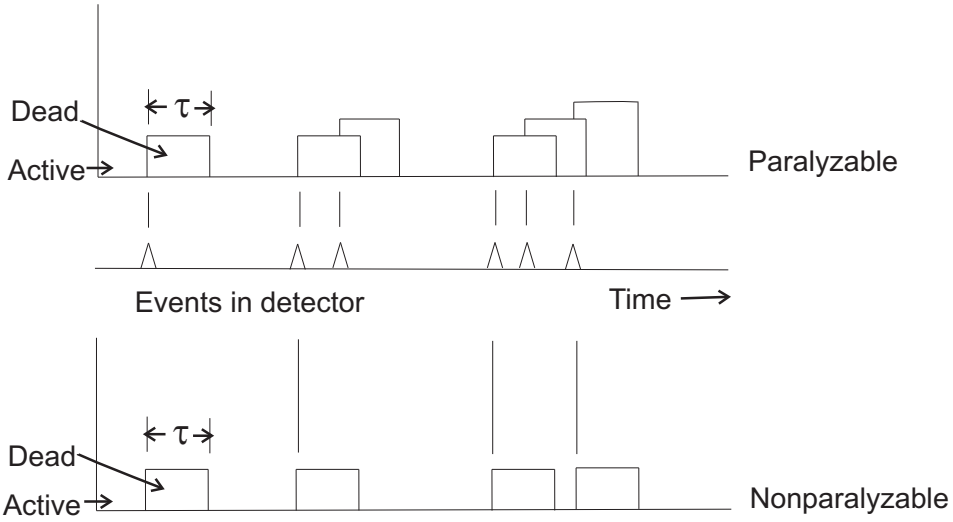

Figure 2.15: An illustration of two models of dead time behaviour for radiation detectors. "Dead" stands for the dead period of the detector, whereas "Active" stands for the active period of the detector.

A simple expression for the nonparalyzable dead time can be derived in the following way. Suppose R_t is the true count rate of a detector system that registers m counts in a given period T. Assuming that each detected count engenders a constant dead time τ, a total dead time $m\tau$ is accumulated during the counting period T. During this dead period, a total of $R_t m\tau$ counts are lost. The true number of counts is therefore

$$R_t T = m + R_t m\tau. \tag{2.23}$$

Solving for R_t in terms of m gives

$$R_t = \frac{R_o}{1 - R_o\tau}, \tag{2.24}$$

where R_o is the observed count rate and defined as $R_o = m/T$. Note that Equation 2.24 can also be written for the observed count rate, namely,

$$R_o = \frac{R_t}{1 + R_t\tau}. \tag{2.25}$$

For the paralyzable case, dead periods are not always of fixed length, so the same method cannot be applied. Rather the observed count rate R_o for the total counting period T is the fraction of the true events that satisfy the condition

$$R_o = R_t e^{-R_t\tau}. \tag{2.26}$$

There is no analytic equation for R_t as a function of R_o for the paralyzable case. A plot of the observed count rate R_o versus the true count rate R_t is shown in Figure 2.16 for both models. When the rate is low the two models give virtually the same result, but the behaviour is markedly different at high rates. The observed count rate for a nonparalyzable system is seen to increase asymptotically toward a maximum value $R_o^{max} = 1/\tau$, which represents the situation in which the counter barely has time to finish one dead period before starting another. For paralyzable behaviour, the observed count rate is seen to go through a maximum value $R_o^{max} = 1/e\tau$, where e is the base of natural logarithms, and then decreases with further increase in true count rate. This is because additional events serve only to extend the already long dead time intervals without contributing to additional events in the observed count rate. At very high true count rate, the observed count rate can approach zero. This is called counter paralysis. These two dead time models are adequate for most practical nuclear medical imaging systems, however, they are only first order approximations. More rigorous treatments and discussions on dead time problems are beyond the scope of this thesis (Cherry *et al.*, 2003; Knoll, 2000; Leo, 1994).

2.7.2 Methods of dead time measurement

A prior knowledge of the dead time τ is required to make system dead time corrections with either of the dead time models. Most often however, the dead time is not known, or varies with detector operation conditions and therefore must be measured directly. Two methods of measuring the dead time of imaging devices as explained by Knoll (2000) include the *two-source method* and the *decaying source method*. The former is based on observing the count rate from two sources individually and in combination, whereas the latter is based on analyzing the count rates of a short-lived radioisotope source acquired over a period of time. A detailed investigation with the *decaying source method* performed for a Compton camera model is reported in Chapter 5.

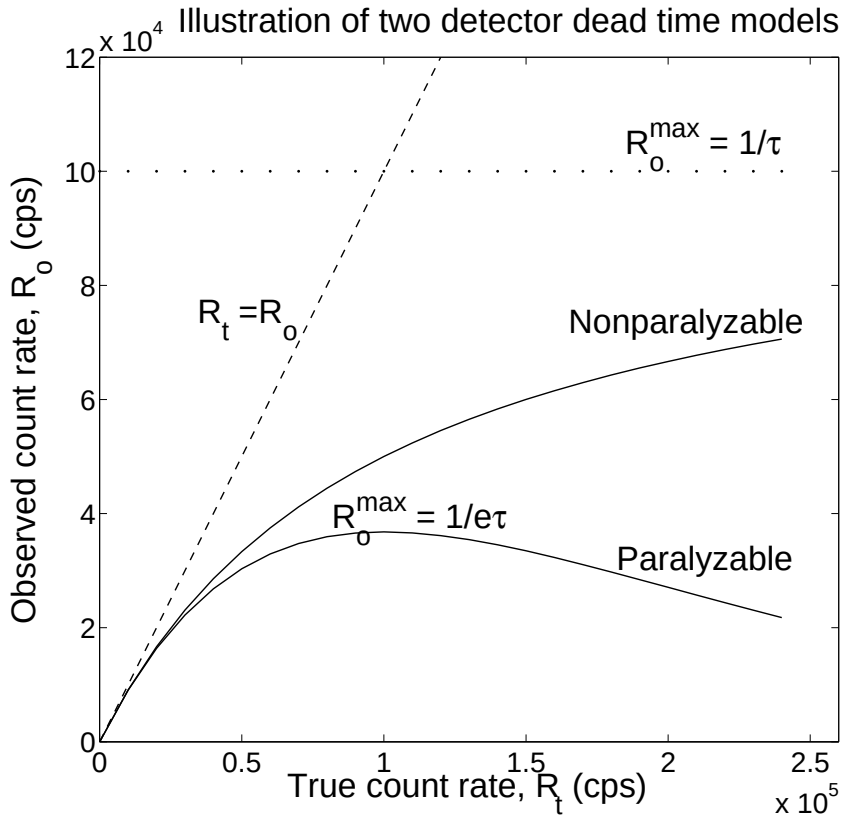

Figure 2.16: The variation of the observed count rate R_o with the true count rate R_t for paralyzable and nonparalyzable dead time models. Note that $\tau = 10^{-5}$ second.

2.8 Radiation detectors for Compton imaging

A variety of radiation detector materials present themselves as potential detectors for the Compton camera. In general, suitable detectors for Compton cameras must be able to detect, track and measure ionizing radiation. As indicated in Section 2.1, ionizing radiation interacts with detectors (or matter) by causing ionization and/or excitation of atoms and molecules. The ionized and excited products undergo recombination or de-excitation to produce energy. Most of these energies are dissipated by various means that include molecular vibrations in gases, lattice vibrations in a crystal and visible light emission in a scintillation material. The first category of energy dissipation relates to the gaseous ionization detectors, the second to the semiconductor detectors and the third to the scintillation detectors. Ideally, the Compton camera scatterer and absorber should have high spatial and energy resolution, with the scatterer having a high Compton scattering cross section and the absorber a high photoelectric cross section. In this section, the basics principles of the three detector types above and their applicability to Compton imaging are discussed.

2.8.1 Gaseous ionization detectors

Gaseous ionization detectors belong to a class of detectors that respond to radiation by means of ionization-induced electrical currents. The basic configuration of gaseous ionization detectors consists of a container with conducting electrodes (walls) that are separated by a volume of gas with a voltage difference (and by implication, an electric field) between the electrodes (see Figure 2.17). The strength of the electric field between the electrodes determines the level of the detector's response to ionizing radiations. If a photon passing through the gas has enough energy to ionize a gas atom or molecule, the resulting electrons are attracted to the positive electrode and the ions to the negative electrode, causing a momentary flow of a small amount of electrical current. Common examples of the gaseous ionization detectors include the ionization chambers, the proportional counters and the Geiger-Müller (GM) counters. The use of this class of detectors for Compton cameras is, however, very restricted because their stopping power and detection efficiency are quite low (Cherry *et al.*, 2003; Leo, 1994).

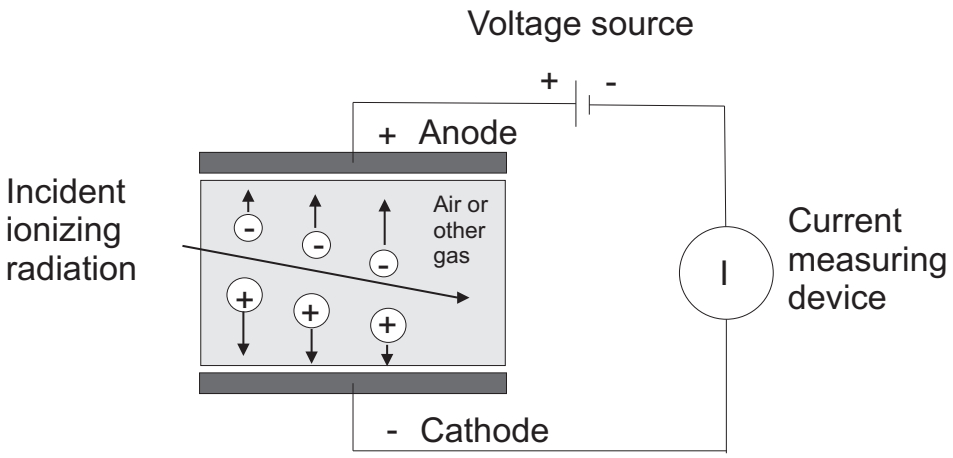

Figure 2.17: Basic principles of a gas-filled detector. Electrical charge released by ionizing radiation is collected by the positive electrode (anode) and the negative electrode (cathode). (This figure is adapted from (Cherry *et al.*, 2003))

2.8.2 Semiconductor detectors

The basic configuration of the semiconductor detectors is analogous to that of the gaseous ionization detectors, except for their condensed atomic structure which gives them increased efficiency, energy and spatial resolution for imaging radiation. In a semiconductor detector, ionizing radiation is measured by means of the number of charge carriers set free in the detector, which is arranged between two electrodes. The process of ionization produces free electrons which are transferred from the valence band to the conduction band, and an equal number of holes is created in the valence band as well. The number of electron-hole pairs is proportional to the energy transmitted by the radiation to the semiconductor. Under

the influence of an electric field, the electrons and holes travel to the electrodes, where they are collected as electrical pulses that can be measured in an outer circuit. Thus, by measuring the number of electron-hole pairs, the energy of the incident radiation can be found (Cherry *et al.*, 2003).

Several semiconductor materials have been investigated for use in Compton camera systems. These include silicon (Si) (Studen *et al.*, 2004), germanium (Ge) (An *et al.*, 2007) and cadmium zinc telluride (CZT) (Du *et al.*, 2001). Si and Ge semiconductors dominate the choice of the scatterer materials in most proposed Compton camera designs. The choice of these materials is primarily due to their excellent charge transport properties, ease of fabrication, high Compton scattering cross section, relatively low cost and good energy resolution in comparison to other semiconductor materials (Knoll, 2000). In the presence of electronic noise, the FWHM energy resolution of semiconductors is limited statistically according to the following equation (Dogan and Wehe, 1994)

$$\Delta E_s^2 = 2.35^2 FW E_s + (\Delta E_s)_{noise}^2 + (\Delta E_s)_{leakage}^2 , \tag{2.27}$$

where F is the Fano factor accounting for departure of ion pair production from Poisson statistics (0.084–0.160 for Si and 0.057–0.129 for Ge), W is the average ionization energy (3.6 eV for Si and 2.9 eV for Ge), E_s is the energy deposited in the semiconductor material by the recoil electron, $(\Delta E_s)_{noise}^2$ is the equivalent noise added by the preamplifier-amplifier combination and is expressed in terms of the equivalent noise charge (ENC) (8.5 × ENC (electrons) for Si and 6.8 × ENC (electrons) for Ge), and $(\Delta E_s)_{leakage}^2$ is the equivalent spread due to detector leakage current and charge collection variations in the detector. The noise term plays an important role for determination of energy resolution. The effects of this term on the energy resolution of a Si material at an incident photon energy of 140.5 keV is illustrated in Figure 2.18(a). In this figure, it can be observed that increase in the electronic noise will increase the effect of the energy resolution on the Compton camera's angular resolution considerably, which is more prominent for low and high scattering angles. However, there would be advantages in operating with electronic noise below 2 keV FWHM, possibly as low as 1 keV, to give good resolution down to 5° scattering angles for the case of 511 keV (see Figure 2.18(b)).

It is worth-mentioning that not all the properties of Si and Ge semiconductors are ideal. The material has low photoelectric linear attenuation coefficient and consequently suffers from poor detection efficiency. Hence fabricating detectors out of higher atomic number compounds such as CZT will increase detection efficiency.

CZT crystals have attracted a lot interest in various fields. The material in essence is a CdTe material in which some of the Te atoms, typically between 10% to 20% are replaced by Zn atoms (Cherry *et al.*, 2003; Chen *et al.*, 2007, 2008). Thus, CZT has very similar properties to CdTe. Admittedly, this semiconductor material is of poorer energy resolution than Si and Ge, and is presently less used in nuclear medical imaging, but it overcomes two of the major drawbacks of Si and Ge: it can be operated at room temperature

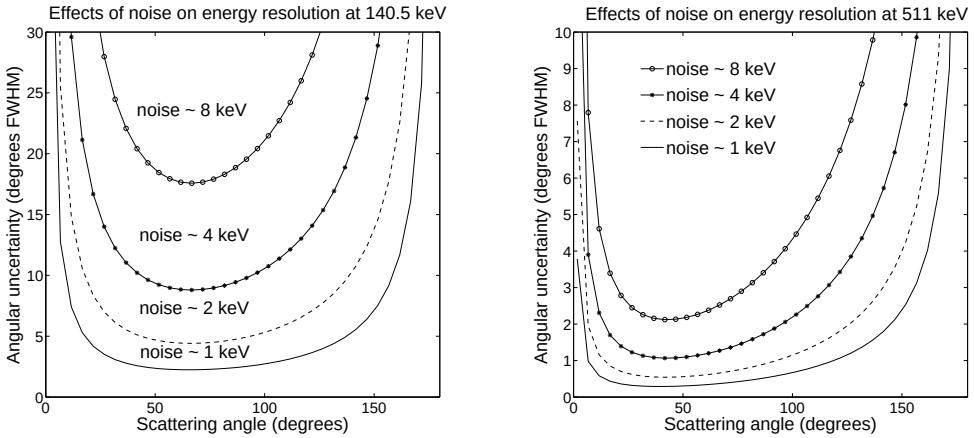

(a) (b)

Figure 2.18: An illustration of how equivalent noise from the preamplifier-amplifier can affect the Compton camera angular resolution at (a) 140.5 keV and (b) 511 keV.

without excessive electronic noise, and the higher atomic number of the material means that it can be a good Compton camera absorber. Nevertheless, CZT crystals are mostly available in small sizes due to the difficulty and expense of growing large pieces with acceptable purity. However, a recent CZT crystal growth method, "Traveller Heater Method", proposed by Chen *et al.* (2007, 2008) offers the possibility of overcoming these drawbacks of the material in the near future.

2.8.3 Scintillation detectors

The basic principles

The scintillation detectors make use of the fact that certain materials, when excited (struck) by ionizing radiation absorbs energy, and reemit the absorbed energy in the form of light. This property is called *luminescence*. The amount of light produced in an excitation process is proportional to the energy deposited by the incident radiation in the detector. If the re-emission occurs immediately after absorption or more precisely within 10^{-8} s, the process is called *fluorescence*. But sometimes, the excited state is metastable, so that the relaxation time from the excited state varies from a few microseconds to even hours depending on the material. In this case, the process is called *phosphorescence* (afterglow). These situations imply that the interaction between a radiation and a scintillation detector depends on the type of transition and the wavelength of the emitted optical (light) photon. Note that the terms *scintillation detector* and *scintillator* will be used interchangeably from now on. While many scintillation materials exist, not all are suitable as Compton camera detectors. Suitable scintillators should exhibit a variety of properties which should include:

Sensitivity to energy: Above a certain minimum energy, the light output of the scintillator should be directly proportional to the exciting energy.

Fast time response: The response and recovery time of the scintillator should be short to allow for short detector dead time, leading to obtaining the time difference between two events with greater precision.

Pulse shape discrimination: The scintillator should distinguish between difference types of particles by analyzing the shape of the emitted light pulses. This is possible by the fact that particles of different ionzing power exhibit different fluorescence mechanisms.

At least six types of scintillation materials are in use. These include: organic crystals, organic liquids, plastics, inorganic crystals, gases and glasses. However, discussions will be limited to the type of scintillation materials investigated in this thesis, which fall into the class of inorganic crystals. The basic configuration of a scintillation detector consists of a scintillator coupled to an electronic light sensor known as a photomultiplier tube (PMT) or a photodiode (Cherry *et al.*, 2003; Knoll, 2000; Leo, 1994). A PMT is illustrated in Figure 2.19.

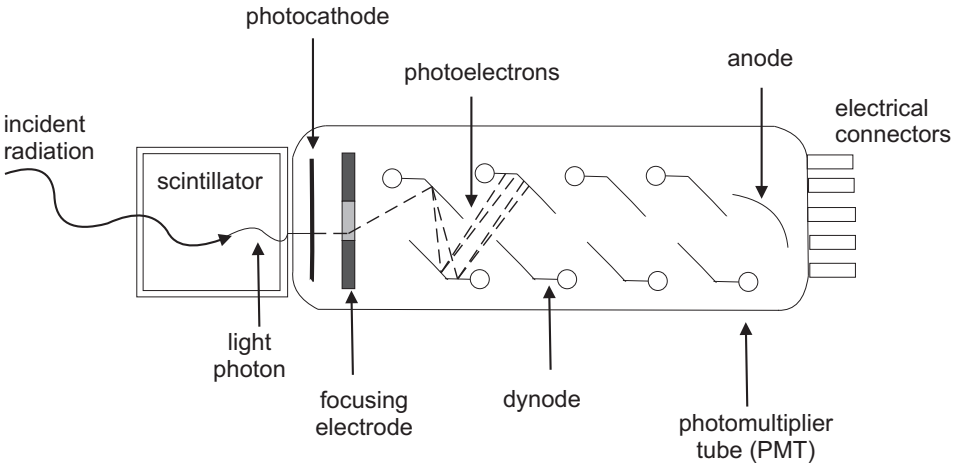

Figure 2.19: The basic configuration of a scintillation detector with the basic operation mechanisms of PMT illustrated.

A typical PMT consists of a photocathode (or photoemissive cathode) followed by a focusing electrode, metal channel dynodes (electron multipliers) and an anode (electron collector) in a vacuum tube as shown in Figure 2.19. When a light (optical) photon from the scintillator enters the photocathode, the photocathode emits photoelectrons into the vacuum. These photoelectrons are then directed by the focusing electrode voltages towards the metal channel dynodes where electrons are multiplied by the process of secondary emission. The multiplied electrons are collected by the anode as an output electrical signal which can be analyzed to give meaningful information about the incident radiation. Because of secondary-emission multiplication, PMTs provide extremely high sensitivity and exceptionally low noise which make them ideal for the detection of extremely low light or short pulses of light. This notwithstanding, research is still underway to produce a photon-counting light detection device that is much more efficient because most practical photocathodes are less than 30% quantum efficient, meaning that 70% of the light photons im-

pacting on the photocathode do not produce a photoelectron and are therefore not detected (Hamamatsu Photonics, 2006).

An important feature of the scintillation detector is its energy resolution, $\Delta E/E$. According to Moszyński (2003), the parameter can be defined as follows:

$$(\Delta E/E)^2 = (\delta_{int})^2 + (\delta_{tr})^2 + (\delta_{st})^2 , \tag{2.28}$$

where δ_{int} is the intrinsic resolution of the scintillator, δ_{tr} is the transfer resolution and δ_{st} is the PMT contribution to the resolution. The term δ_{int} is related to the non-proportional response of the scintillator. However, the experimentally determined intrinsic resolution is affected also by many effects such as inhomogeneities in the scintillator causing local variations in the light output and non-uniform reflectivity of the reflecting cover of the crystal. The term δ_{tr} is described by the variance associated with the possibility that a photon from the scintillator results in the arrival of a photoelectron at the first dynode and then is fully multiplied by the PMT dynode chain. δ_{tr} depends on the quality of the optical coupling of the scintillator to the PMT input window, the homogeneity of the quantum efficiency of the photocathode and the efficiency of photoelectron collection at the first dynode. In modern scintillation detectors the term δ_{tr} is negligible compared to the other components of the energy resolution. The term δ_{st} can be defined as (Moszyński, 2003; Moszyński *et al.*, 2006):

$$\delta_{st} = 2.35\sqrt{\frac{(1+\varepsilon)}{N}}, \tag{2.29}$$

where N is the number of photoelectrons and ε is the variance of the electron multiplier gain, typically 0.1 to 0.2 for modern PMTs (Dorenbos *et al.*, 1995; Moszyński *et al.*, 2002; Moszyński, 2003; Moszyński *et al.*, 2006).

Inorganic scintillation crystals

A great deal of effort has been put forth to improve the performance of inorganic scintillation crystals (precisely, alkaline halide crystals) as radiation detectors. This is due to their comparatively good detection efficiency for hard radiation. Although a few of them may operate as scintillators in their pure state —for example, pure sodium iodide (NaI) crystals at liquid nitrogen temperatures —a vast majority are "impurity activated". The impurity atoms of these crystals had been found to be responsible for the scintillation effect, therefore are sometimes called *activator centres* (Cherry *et al.*, 2003).

Sodium iodide crystals doped with 0.1% to 0.4% thallium as an activator, NaI(Tl), are the standard detector used for comparisons with other radiation detectors. The notable features of NaI(Tl) are its good light output (38 000 photons/MeV), moderate energy resolution, low cost and good linear response over a large energy range of incident radiation. However, it is also hydroscopic, which requires the crystal to be hermetically sealed, usually together with the PMT. If not sealed the crystal quickly deteriorates due to the absorption of moisture in the air. Also, it has a relatively long scintillation time of 230 ns, which may be a

problem for high count rates, and a phosphorescence component with decay time of 0.15 s. In most applications, phosphorescence is not important, since each phosphorescence photon is detected as a single event giving rise to a single photoelectron. Such a small signal can be ignored by using a discriminator set to the appropriate level. NaI(Tl) is also fragile and can be easily damaged by mechanical or thermal shock. However, no scintillator satisfies all imaging conditions well, therefore some compromises are struck in most cases depending on the imaging modality. But recent lanthanide bromide crystals doped with 0.5% to 5% cerium atoms, $LaBr_3$(Ce), appear to have gained a new interest due to their superior scintillation properties (Dyer, 2001).

Continuous $LaBr_3$(Ce) crystals, developed by Delft University of Technology, The Netherlands (van Loef *et al.*, 2002), have been characterized by sub-millimetre spatial resolution (Pani *et al.*, 2008), and superior energy resolution of $\leq 3\%$ (FWHM) at 662 keV (Kumar *et al.*, 2009). This is by far, the best for any scintillator at present. The crystals' fast light pulse decay time is estimated at 16 ns, with no intense slow components and afterglow; which allows for high count rates. This combined with a large light output, above 60 000 photons/MeV, assures an excellent time resolution of 300 ps (Moszyński *et al.*, 2008). Another interesting feature of $LaBr_3$(Ce) crystals is their negligible variation of light output within the temperature range $-20°C$ to $60°C$, which limits the problem of the detector temperature instability to that of the PMT (Kumar *et al.*, 2009; Moszyński *et al.*, 2006, 2008). The high density of $LaBr_3$(Ce) and high atomic number of lanthanum also results in higher detection efficiency than NaI(Tl) (Kumar *et al.*, 2009). All these properties have opened up a very wide usage of $LaBr_3$(Ce) crystals for a variety of applications. On this note, several studies have been conducted to evaluate the viability of $LaBr_3$(Ce) crystal as a gamma camera detector for scintimammography (Pani *et al.*, 2006b, 2007). A similar investigation of $LaBr_3$(Ce) crystal's performance as a Compton camera absorber for scintimammography is presented in Chapter 6.

2.9 Reconstruction

A careful review of the literature reveals that numerous reconstruction methods have been used to estimate images of gamma emitter distributions obtained from measured Compton camera data. In general, the input to the reconstruction algorithm is a list of data obtained from photon interactions in Compton camera detectors which includes: the photon interaction positions (determined by the volume flux density of photons at the detection sites) and the corresponding deposited energies. The output of the reconstruction algorithm is a three dimensional voxel intensity proportional to the strength of the radionuclide emitter. The quality of the final source image and the reconstruction time allow evaluation of the quality of the reconstruction method used, as well as the accuracy of the measured Compton camera data (Studen, 2005a).

Although several reconstruction algorithms have been proposed for the Compton camera data, this section will discuss only the basic principles of the reconstruction method used

to produce the results reported in this thesis, which is the list-mode backprojection method. Therefore, this is not an exhaustive discussion on Compton camera reconstruction methods.

2.9.1 The system matrix

The reconstruction of images from the Compton camera projection data involves solving the equation

$$g = Af, \tag{2.30}$$

where g is the Compton projection data, considered to be conical surface integrals or integrals of cone beam line integrals that have been weighted by the Klein-Nishina distribution of scattering angles and blurred by the Doppler effect, f is the source distribution and A is the system matrix.

Equation 2.30 can be represented in discrete notation as:

$$g_{P_1P_2\theta} = \sum_{ijk} A_{ijk}^{P_1P_2\theta} f_{ijk}. \tag{2.31}$$

In this case, the distribution of radioactivity is partitioned into voxels. Here the system matrix $A_{ijk}^{P_1P_2\theta}$ represents the probability that a photon emitted from a voxel (i, j, k) is scattered at a position P_1 of the scatterer with a scattering angle θ and detected at a position P_2 of the absorber. For efficient computation, the system matrix can be factorized into sub-probabilities as follows:

$$A_{ijk}^{P_1P_2\theta} = M_{ijk}^{P_1P_2\theta} M_\theta. \tag{2.32}$$

According to Equation 2.32, elements of the system matrix can be computed by the probability $M^{P_1P_2\theta}$ with which a voxel (i, j, k) belonging to a conical surface is determined by P_1 P_2 and θ, and the probability M_θ relating to Compton scattering in the scatterer. If the interaction in the scatterer is Compton scattering, the probability M_θ is the differential cross-section for the Compton scattering which can be calculated with the Klein-Nishina formula (Smith, 2005; Kim *et al.*, 2007).

2.9.2 Limitations on computing the system matrix

The direct inversion of the system matrix A to solve for f in Equation 2.30 exists in theory. But in reality, no exact analytical solution for the inversion of A has been implemented in real Compton cameras, neither has the conventional iterative reconstruction methods proven easy to handle. The reasons for these limitations can be summarised as follows:

- The inversion of A is computationally demanding, even for $64 \times 64 \times 64$ image voxels.
- A^{-1} may not be unique.
- A is ill-conditioned (very small changes in projection data g may produce large differences in the result f).

In real systems, the matrix A is ill-conditioned which is complicated by noise in the projection data g. The problem is made even worse by the fact that the number of the detected photon events in real Compton cameras is often of several orders magnitude smaller than the number of elements of A in most cases. To see why this is true, let us consider the size of the matrices and the vectors that are involved. If it is assumed that, in terms of order of magnitude, there are 10^4 elements in each of the detectors and 10^2 energy levels that are measured in the first detector, then there are 10^{10} measurement bins associated with one positioning of the camera. In contrast, in one positioning of a conventional SPECT camera there are typically no more than 10^4 measurement (Smith, 2005). Based on these reasons, the direct inversion solutions of A are not widely employed (Bruyant, 2002). Instead, event-based reconstruction methods which treat each detected photon event as a point in a continuous measurement space, rather than as a contributing count to a position and energy bin may be preferable (Wilderman *et al.*, 1998b). Along these lines, several investigators such as Wilderman *et al.* (1998a,b), Kim *et al.* (2007) and Andreyev *et al.* (2011) have presented in the context of Compton camera, a variety of list-mode reconstruction algorithms. These algorithms are distinguished by the capability of preserving the accuracy of the measured data that would otherwise be lost in the discretization of energy and position. List-mode algorithms can be implemented as part of a back-projection reconstruction method or as part of an iterative reconstruction method.

2.9.3 List-Mode Backprojection

The list-mode backprojection method is applicable to any Compton camera configuration requiring the projection data in the form of lists of photon detection positions and energy losses for all the recorded coincident events (Wilderman *et al.*, 1998b). Details of each single photon coincident event should include the detected position in the scatterer $P_1 = (s_x, s_y, s_z)$, the detected position in the absorber $P_2 = (a_x, a_y, a_z)$ and the energy transferred to the scatterer E_s used to determine the scattering angle θ from the Compton equation. Figure 2.20 illustrates the operation of this algorithm for a single photon coincident event. Note that since a three-dimensional image of a gamma source distribution is usually obtained by piling up many slices of two-dimensional reconstructed images, the discussion on the list-mode backprojection reconstruction herein is limited to a single image slice for simplicity.

Consider a certain photon that is emitted from a source and is travelling along the z-axis as shown in Figure 2.20. If this photon Compton scatters at P_1 located in the scatterer and is fully absorbed at P_2 in the absorber, the vector connecting P_1 to P_2 defines a cone axis, and the energy deposited at P_1 can be used to determine the cone angle from the Compton equation, with the cone peak originating from P_1. The intersection of the conical surface with an orthogonal x-y image plane forms an ellipse on the plane, and subsequent accumulation of multiple ellipses gives the possible position of the source voxel denoted by (f_x, f_y, f_z).

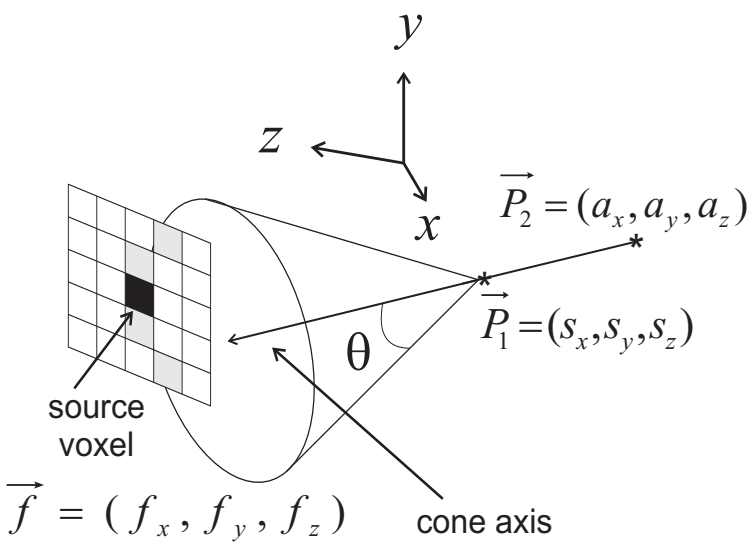

Figure 2.20: An illustration of a backprojected cone of a Compton scattering event. Positions indicated with an asterisk represent positions of interactions in the scatterer $P_1 = (s_x, s_y, s_z)$ and the absorber $P_2 = (a_x, a_y, a_z)$. The positions of interactions and the scattering angle θ can be measured, and together determine the origin point of the incident photon to lie on the cone-surface somewhere within an image grid, as shown.

If a voxel f is on the cone surface, the ellipse equation can be derived from the inner product of the vector $\overline{P_1P_2}$ and the vector from the voxel on the ellipse f to P_1. That is,

$$|f\,P_1| = |P_1P_2| \cos\theta. \tag{2.33}$$

Variables are f_x, f_y and f_z in Equation 2.33 for a three dimensional image reconstruction. However, reconstruction on one image slice (in two dimensions) requires setting f_z equal to the source-to-scatterer distance (this assumption is reasonably accurate if the source location is known). This implies the sampling of the intersecting ellipse at a fixed distance f_z along the $x - y$ plane. The drawing of the ellipse requires finding the solutions (f_x, f_y) of Equation 2.33. These solutions are approximately calculated by projecting along the x- and y-axis. By inserting a sampled f_x, the corresponding f_y can be calculated and vice versa.

2.10 Monte Carlo simulation by GEANT4

Monte Carlo experiments are a class of computational algorithms that rely on repeated random sampling to compute their results. They are most suited to calculation by a computer and tend to be used when it is not feasible to compute an exact result with a deterministic algorithm. They are also considered to possess the capability of addressing the challenging requirements of new-generation experiments (Anderson, 1986).

The GEANT4 toolkit provides an excellent platform for the simulation of the transport and interactions of particles with detectors using Monte Carlo methods. The simulation

toolkit was developed in response to the needs of modern experiments. The GEANT4 toolkit can contain various components such as event generation, detector simulation, reconstruction and analysis which can be used separately or in combination. Other design requirements make it modular and flexible and thus its implementation of physics is transparent and open to user validation. The toolkit's modular architecture allows the user to pick only those components he/she needs (Agostinelli *et al.*, 2003). An overview of the descriptions of the functionalities GEANT4 provides follows.

2.10.1 GEANT4 kernel

The GEANT4 kernel manages the simulation runs, events and tracking. The Event package provides an abstract interface to external physics event generators for the creation of the primary particles. The kernel handles the tracking of particles taking account of the geometry, fields and physics processes. GEANT4 Tracking steers the invocation of physics processes in a general way for all particle types, thus allowing great flexibility in the implementation of a variety of physics processes, as well as openness to further extensions. The management of particles is based on Particle Data Group (Nakamura, 2010) compliant definitions and data, including their decay processes and modes.

2.10.2 Geometry and materials

The GEANT4 geometry package provides tools to describe the geometrical structure of a detector and the patient's organs in detail and realistically. This makes it possible to describe the experimental set-up accurately (Foppiano *et al.*, 2005). It also handles the equation of motion solvers in different fields and geometrical boundary conditions for the propagation of particles. The GEANT4 materials package allows the description of materials consisting of a single element or a composition of elements, which in turn can consist of a single isotope or a mixture of isotopes. The *Hits* and *Digi* domains provide the functionality to reproduce the readout structure of a detector and its electronic response, independently from the geometry used for tracking particles.

2.10.3 Interactive facilities

GEANT4 visualisation packages provide the capability to visualise detector geometry, particle trajectories, tracking steps, hits and text. Its design, based on abstract interfaces, makes GEANT4 independent from any particular graphics system. At the same time it allows multiple implementations of drivers to interface the simulation with a variety of such systems. The *User Interface* domain adopts a similar approach, allowing the usage of a variety of user interfaces, from simple command-line driven ones to sophisticated Graphic User Interfaces (GUI)s. To avoid any internal dependence on any specific analysis tool, GEANT4 supports the adoption of Abstract Interfaces for Data Analysis (AIDA (Barrand *et al.*, 2001)), which are used internally in the physics tests and in the advanced examples distributed together with the toolkit.

2.10.4 Other features

A *Fast Parameterisation* facility is integrated with the full simulation, allowing independent and simplified detector descriptions and direct production of hits. The *Persistency* category provides an interface for storing and retrieving runs, events, hits and geometry information. Extensive possibilities for interaction with the GEANT4 system are offered to the user via a set of dedicated user-action classes (Pia, 2003).

2.11 The GEANT4 low energy physics models for particle interactions

The GEANT4 toolkit consists of a series of packages for electromagnetic physics, specialized for different particle types, energy range or approach in the physics modelling. But the most important to this thesis is the GEANT4 Low Energy Electromagnetic package which is very relevant to medical applications. This package includes a variety of models for electromagnetic processes of electrons, photons, hadrons and ions, taking into account advanced features, such as shell effects and effects due to charge dependence. The object-oriented design of GEANT4 provides the ability to implement or modify any physics process without changing other parts of the software. Processes for photons inherit from *G4VDiscreteProcess*, while processes for electrons, hadrons and ions inherit from *G4VContinuousDiscreteProcess*. Both categories of processes are handled transparently by the GEANT4 kernel through their abstract interfaces.

The implementation of Low Energy electron and photon processes covers the energy range from 100 GeV down to 250 eV for elements with atomic number between 1 and 99. Processes in this category include the Compton scattering, photoelectric effect, Rayleigh scattering, bremsstrahlung, ionization and Auger effect. Fluorescence emission from exited atoms and polarization of radiation are equally handled in this category.

The GEANT4 Low Energy package can also handle the ionization by hadrons and ions. For this, different models are implemented depending on the energy range and the particle charge. In the high energy (E >2 MeV) domain the Bethe-Bloch formula is implemented, whereas in the low energy domain (E <1 keV for protons) the free electron gas model is applied. In the intermediate energy range, parameterized models based on experimental data from the Andersen and Zieger (1977) and ICRU review (Allisy *et al.*, 1993) are implemented. Corrections due to the molecular structure of materials and to the effect of the nuclear stopping power are taken into account. The Barkas effect is also accounted for, and a specialized quantum harmonic oscillator model for negative charged hadrons is provided, down to 50 keV.

For accurate implementation of Doppler broadening in Compton scattering process, two alternative sets of models are available in GEANT4 Low Energy Electromagnetic package. One is based on the EPDL97 (Cullen *et al.*, 1997) evaluated data library and the other, on analytical models (Baro *et al.*, 1995) originally developed for the PENELOPE Monte Carlo

system.

The library-based physics model makes ample use of public evaluated databases, distributed by a variety of sources. Notably, the data libraries, EPDL97 (Cullen *et al.*, 1997), EEDL (Perkins *et al.*, 1997b) and EADL (Perkins *et al.*, 1997a), which provide data for the determination of cross-sections and the sampling of the final state. This physics model was recently upgraded to incorporate Doppler broadening in Compton scattering by Longo *et al.* (2008), which has contributed to the reliability and the transparency of the physics implementation.

In the PENELOPE physics model, the implementation of Doppler broadening and binding effects in Compton scattering events are included by means of the cross-section obtained from the relativistic impulse approximation (Ribberfors, 1975). Contributions from different atomic electron shells are considered separately. After a Compton interaction with the *i*–th shell for instance, the participating target electron is ejected to a free state with kinetic energy

$$\Delta E = E_\gamma - E'_\gamma - U_i > 0, \tag{2.34}$$

where E_γ is the incident photon energy, E'_γ is the scattered photon energy energy, U_i is the ionization energy of the considered shell, and the residual atom is left in an excited state with a vacancy in the *i*–th shell. The total atomic cross-section of Compton scattering process is then evaluated using an analytical parameterization approach, which involves integration over the final photon directions and energies (Brusa *et al.*, 1996). The total cross-section as given in GEANT4 physics manual is (GEANT4 Collaboration, 2011)

$$\sigma_{inc} = 2\pi \int \frac{r_e^2}{2} \left(\frac{E_C^2}{E_\gamma^2} \right) \left(\frac{E_C}{E_\gamma} + \frac{E_\gamma}{E_C} - \sin\theta \right) \sum_{shells} Z_i \Theta \left(E_\gamma - U_i \right) n_i \left(p_{i,max} \right) \, d\left(\cos\theta\right). \tag{2.35}$$

Here r_e is the classical electron radius, E_C is the Compton energy defined by Equation 2.4, θ is the scattering angle, Z_i is the number of electrons in the *i*–th atomic shell, U_i is the ionization energy of the *i*–th atomic shell, Θ is the Heaviside step function, n_i is normalized approximate one-electron Compton profile of the active shell and $p_{(i,max)}$ is the highest possible value of p_z (projection of the initial momentum of the electron in the direction of the scattering angle) which is equivalent to Equation 2.18. The derivation of the above equation is beyond the scope of this thesis; interested readers should consult Brusa *et al.* (1996) and GEANT4 Collaboration (2011).

Chapter 3

GEANT4 EVALUATIONS OF THE COMPTON CAMERA SCATTERER

Detectors are the heart of a SPECT system and are, thus, responsible for collecting the high-energy photons emitted from the patient, estimating the photon energy and locations of interactions, and generating the count data for subsequent image reconstruction. The ability to perform these functions depends on their design, materials, and electronics (Holly *et al.*, 2010). In this chapter, a GEANT4 description and analysis of the first detector (scatterer) parameters of the Compton camera as to how they affect the camera's performance in medical applications is provided. For maximum benefit, a brief overview of different proposed Compton camera configurations is first given because, while it can be argued that the general functions of the detectors are more or less the same, the configuration of the Compton camera plays a major role in different applications.

3.1 Camera designs and considerations

A variety of configurations and detector materials have been proposed for the Compton camera. The most common design for the Compton camera dates back to an early paper by Todd *et al.* (1974) in the field. Each of the two detectors was planar, and the two detectors were configured so that they were parallel to each other. Other shapes and configurations for the detectors have also been considered. Planar detectors that were perpendicular to each other (Kroeger *et al.*, 1994) and a planar first detector in front of a cylindrical second detector have been considered (Hua *et al.*, 1999). A spherical-shaped second detector was considered in a computer simulation (Sauve *et al.*, 1999). In any case, a paper by Seo *et al.* (2008) suggests that the parallel detector design may be the best configuration for the Compton camera with respect to sensitivity and resolution.

In addition to the shapes and configurations of Compton cameras, investigators such as Smith (2005) are of the opinion that the Compton camera may not be fully capable of

capturing a complete three-dimensional image of a gamma ray source from one position, therefore the motion of the detectors needs to be considered in the camera's design as well. Despite different views on the Compton camera design, predicting the system performance accurately is the most critical aspect of any Compton camera design.

When designing a Compton camera, considerations must be given to the fact that the factors that govern the camera's imaging performance are intrinsically different from those of other SPECT systems. For instance, unlike the Anger camera, a collimator is not used, therefore the two detectors are exposed to a higher photon flux. Hence they must be able to handle the increased count rate and good temporal resolution is required to accurately identify and accept coincident hits on the two detectors, and reject all other photon detections. Also, accurate estimation and accounting of the variables which affect the camera's performance due to the additional detector (scatterer) used in imaging would be beneficial if the Compton camera is to compete or surpass the Anger camera with respect to image resolution.

3.2 Performance parameters of the Compton camera scatterer

A detailed study of the Compton camera scatterer would allow the limitations introduced by the detector to be determined. A list of variables that affect the imaging performance of the scatterer can been itemized as follows: source-to-scatterer distance, scatterer energy resolution, Doppler broadening, scatterer geometry, scatterer spatial resolution and scatterer temporal resolution. Each of these variables contributes to the accuracy with which the cone associated with a detector event can be defined regardless of the voxel size of the reconstructed image. The impact of each variable on the overall uncertainty is dependent on the geometry of the Compton camera system. A number of these variables are determined by the system application and placement relative to the imaged object, for example, the initial photon energy and source-to-detector distance, whereas others are dependent on detector materials and configuration, for example, the scatterer energy resolution, Doppler broadening and scatterer geometry (Mundy and Herman, 2010). The aspects of the scatterer design that are considered in this thesis are the energy resolution, Doppler broadening and scatterer geometry. The modelling of these parameters is discussed in the following.

3.2.1 Energy resolution

The analyses of the scatterer parameters with GEANT4 began by looking at the accuracy with which the scatterer can measure the energy that is transferred to the recoil electron by the interacting gamma ray. This, of course, depends on the material's energy resolution. According to Figure 2.6, silicon and germanium have the highest Compton scattering probability, therefore the performance of these materials were assessed differently with respect to energy resolution. At present, unfortunately, the functionality to simulate the detector energy resolution in GEANT4 is not well developed. An alternative method is therefore used,

which includes approximating the detector energy resolution by sampling the deposited energies in the scatterer with a Gaussian random number generator (G4RandGauss function) provided in GEANT4, with mean equal to the deposited energy and width (FWHM) equal to an experimentally obtained energy resolution value from the literature. Since only an approximation is used to determine the energy resolution, no detailed results of the detector energy resolution are given in this thesis.

3.2.2 Doppler broadening

Doppler broadening adds to the inherent limitations of Compton cameras to produce images of high resolution at low photon energies. This effect originates from the Compton scattering between a gamma ray and a moving electron bound to an atom of a target detector rather than of a stationary electron as is assumed by the familiar, simple Compton scattering equation (Ordonez *et al.*, 1997). The details of how GEANT4 accounts for Doppler broadening were given in Section 2.11, but will be briefly recounted here for convenience. In order to include Doppler broadening of Compton scattered photon energy due to electron pre-collision motion, GEANT4 samples each Compton scattered photon energy from a cross section formula based on the Compton profile, and the Compton scattering is sustained if the energy imparted to the electron is less than its binding energy. The electron binding effect modifies the scattered photon energy and angular uncertainty distribution as shown in Section 3.2.5.

3.2.3 Previous study on Doppler broadening using the GEANT4

Already introduced in Section 1.2.2 is the variety of other techniques that have been applied to Doppler broadening, hence only the previous studies conducted on Doppler broadening with the GEANT4 will be discussed in this section. The first study of Doppler broadening with GEANT4 simulation toolkit is by An *et al.* (2007). The group utilized the GEANT4 PENELOPE electromagnetic physics model (this physics model is no longer supported in GEANT4) to study the effect of Doppler broadening on the reconstructed image. In their work, a point source was imaged at 6 cm in front of a silicon scatterer and the image resolution was reported as 7.99 cm (FWHM). However, they could not show with GEANT4 how Doppler broadening affects the energy spectra and angular uncertainty. Following, Longo *et al.* (2008) incorporated Doppler broadening into the LowEnergy electromagnetic physics model of GEANT4. This was done by utilizing a computational approach, with the Doppler data obtained from EPDL97 libraries and the tabulated Compton profiles (Cullen *et al.*, 1997; Perkins *et al.*, 1997a,b) as explained in Section 2.11. Preliminary results of the new LowEnergy physics model were compared with those of the PENELOPE physics model and were found to have similar accuracy, but with an enhanced simulation performance.

3.2.4 Present study of Doppler broadening using the GEANT4

Two sets of simulations are presented here. One is to validate the results of the new LowEnergy physics model of GEANT4 with respect to Doppler broadening, and the other is to quantify the effect of Doppler broadening on the performance of medical Compton cameras.

The first task was implemented by relating the impact of Doppler broadening on the Compton camera angular uncertainty and energy spectra. Consequently, the TestEM14 extended example of GEANT4 (release 9.2 patch 01) was modified to utilize Si and Ge detectors as the scatterers. The TestEM14 example generally deals with how to compute cross sections from the direct evaluation of the mean free path, and how to plot the final state of a process (e.g., Compton scattering and photoelectric effect). This example provides a set of macros that define various run conditions. Processes can be activated or inactivated in order to study the processes individually. To study only Compton scattering for example, an event is killed at the first interaction of the incident particle if the interaction is Compton scattering process. The absorption length (mean free path) is computed as the mean value of the track length of the incident particle. The result is compared with the 'input' data, that is, with the cross sections stored in the 'PhysicsTables' and used by GEANT4. The details of simulations to validate the results of the new LowEnergy physics model of GEANT4 with respect to Doppler broadening are as follows.

An isotropic, non-attenuating radioactive source was assumed, and incoming gamma rays were constrained to the direction of the scatterer to increase simulation efficiency. Point sources of two common nuclear medicine energies (140.5 keV and 511 keV) were simulated. A minimum of 10 million events was used for each simulation run. To reduce complexities, multiple scattering events within the scattering medium were eliminated from the analysis and the Compton scattering angles were directly obtained using the GetMomentumDirection function in a derived SteppingAction class.

To study the effect of Doppler broadening on the reconstructed Compton camera image, a camera that consists of a 9 cm × 9 cm Si scatterer separated by 5 cm from a 10 cm × 10 cm CZT absorber was simulated. A gamma ray point source was set at 10 cm in front of the scatterer. Other detector factors such as energy resolution and spatial resolution are not considered in this study and an otherwise 'perfect' camera was assumed. Exact interaction positions and energy depositions in the two detectors for successful photon events were saved to output data files and images of the point source were reconstructed from the simulated data using the list-mode backprojection reconstruction method whose algorithm is given in Section 2.9.3.

3.2.5 Validation of GEANT4 simulated Doppler data

By validating the simulation software with theoretical prediction, confidence can be gained in the results obtained from it. Hence, the simulated estimates of the contribution to angular uncertainty due to Doppler broadening with respect to incident photon energy and scattering

medium were compared with the prediction by Biggs *et al.* (1975), and are shown in Figure 3.1. Here, uncertainty has been defined as the full-width-at-half-maximum (FWHM) of

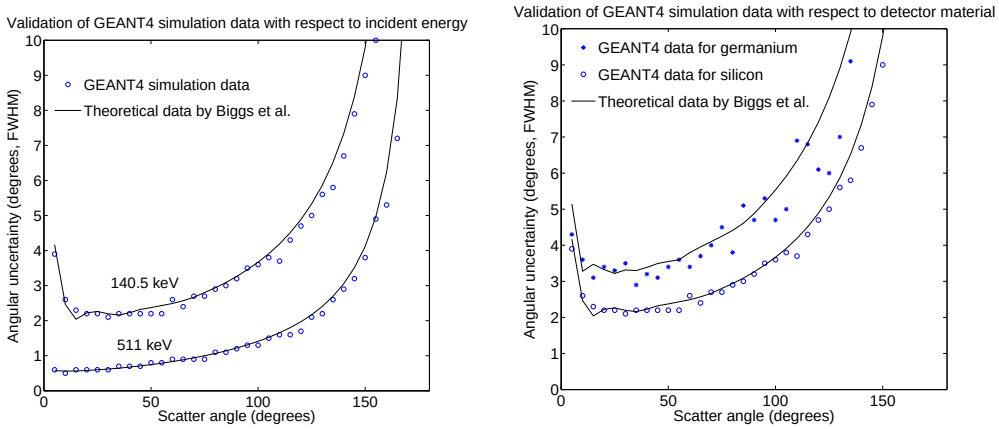

(a) (b)

Figure 3.1: (a) Angular uncertainty due to Doppler broadening for different incident energies using a Si detector, (b) for different scattering materials when the incident energy is 140.5 keV .

the corresponding angular distribution. The histograms of each angle distribution are calculated by binning all the angle counts within 0.1° intervals across the distribution. The solid curves represent the theoretical data by Biggs *et al.* (1975) whereas the circle and asterisk data points represent GEANT4 simulated data. In general, there is a reasonable agreement between the theoretical data and the simulated data by GEANT4. At high scattering angles however, the angular uncertainty by GEANT4 simulations are slightly less than those calculated from Biggs *et al.* (1975). In any case, the simulated uncertainty data points are generally within the error bounds of 5 % with the theoretical data by Biggs *et al.* (1975). Note that Si is the scattering medium in Figure 3.1(a), and increasing the simulation events could reduce the greater spread of the simulated data points for Ge in Figure 3.1(b).

The graphs in Figure 3.1(a) indicate the Compton camera angular uncertainty is greatest at very low and at higher Compton scattering angles. It is also shown in the figure that angular uncertainty decreases with increasing incident photon energy. Figure 3.1(b) suggests that angular uncertainty due to Doppler broadening will increase with higher atomic number Z of the scattering medium. These are important points that must be considered when designing a Compton camera.

To quantify the degree of broadening at different incident energies, two-dimensional histograms of the energy transferred to the recoil electron by the incident photon were plotted with respect to the scattering angle (see Figure 3.2). As expected, there is more broadening of the energy spectrum at 140.5 keV (Figure 3.2(a)) than at 511 keV (Fig 3.2(b)). This gives credence to the fact that better imaging resolution is more probable at high incident energies than at low energies with respect to Doppler broadening.

Figure 3.3 shows similar histograms as Figure 3.2 but this time, for two scattering me-

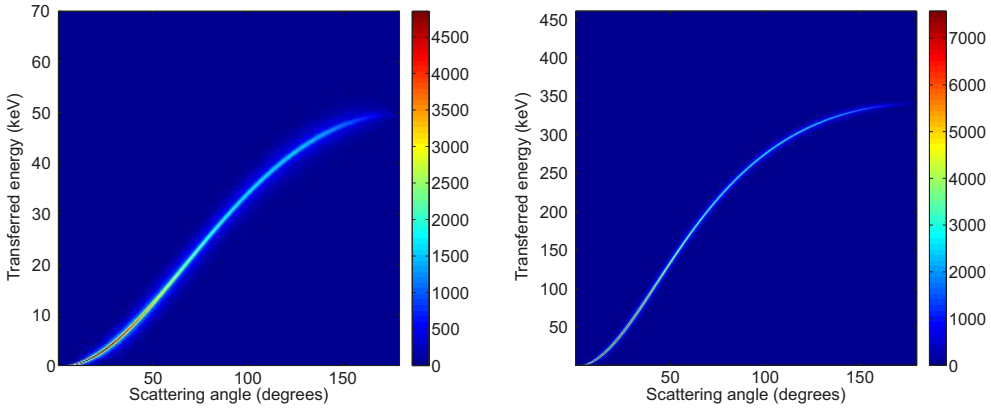

(a) (b)

Figure 3.2: (a) Illustration of the degree of Doppler broadening at 140.5 keV and (b) 511 keV .

dia (Si and Ge) and incident photon energy of 140.5 keV. More broadening is observed for germanium than silicon due to the increased number of electron momentum states available for Compton scattering. This trend of results suggests that low-Z materials are more suit-

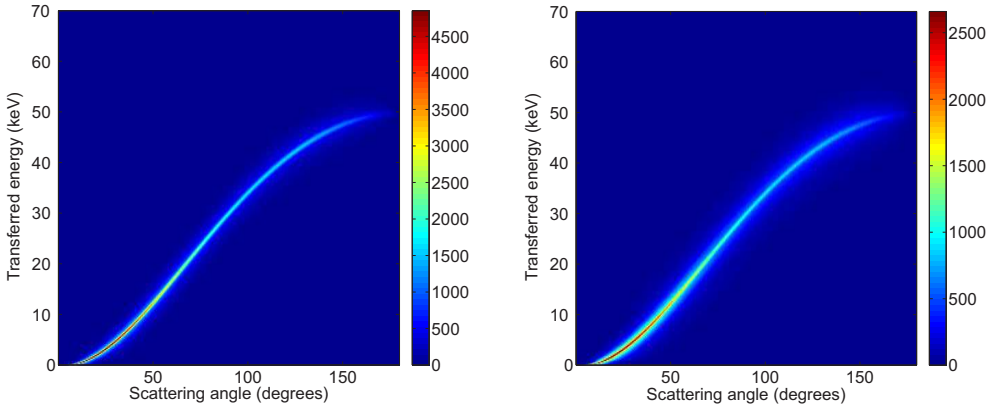

(a) (b)

Figure 3.3: (a) Illustration of the degree of Doppler broadening in Si detector and (b) Ge detector.

able as Compton camera scatterers in terms of Doppler broadening. However, studies have shown that the atomic number-to-Doppler broadening dependence for some materials does not follow this trend when the effects of the core and valence electron ratio are taken into consideration (Reed and Eisenberger, 1972; Biggs *et al.*, 1975).

The effect of Doppler broadening on Compton camera energy spectra is shown in Figure 3.4. The graphs were obtained from a simulation performed for a 140.5 keV source. Figure 3.4(a) shows the spectra of energies transferred to the recoil electrons when the gamma rays are Compton scattered through 90° with and without Doppler broadening be-

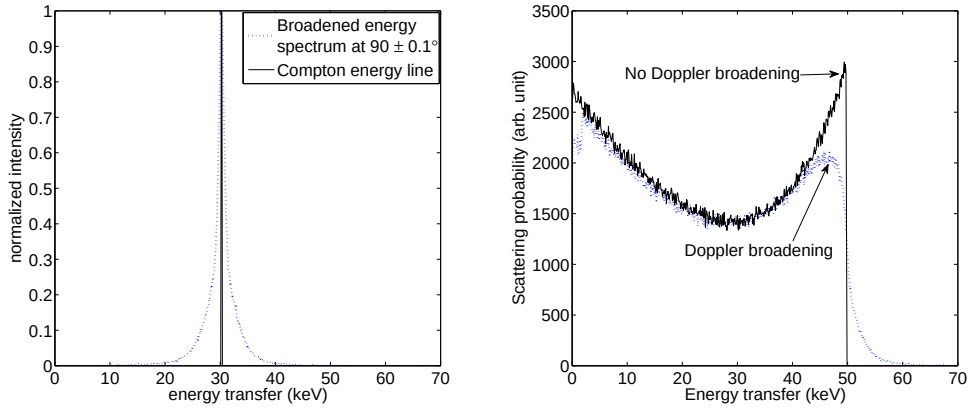

(a) (b)

Figure 3.4: (a) Spectrum of the energies transferred to the recoil electrons for photon scattering angles in the range 90 ± 0.1° in a Si scatterer, (b) Spectrum of the energies transferred to the recoil electrons over all photon scattering angles in a Si detector, with and without Doppler broadening.

Table 3.1: Estimates of image resolutions of a source imaged with two scattering media (silicon (Si) and germanium (Ge)) at two incident photon energies. All image resolution measurements are in mm.

Incident energy (keV)	No Broadening (Si)	Broadening (Si)	No Broadening (Ge)	Broadening (Ge)
140.5 keV	0.58 ± 0.05	7.3 ± 0.3	0.59 ± 0.05	12.3 ± 0.5
511 keV	0.58 ± 0.05	2.4 ± 0.1	0.58 ± 0.05	4.2 ± 0.2

ing taken into account. These graphs actually show the spectra for Compton scattering angles over the range 89.9° to 90.1° as in a Monte Carlo simulation it is unlikely any single event will be found to result in a scattering angle of exactly 90°. Sufficient photons were scattered in the 0.2° range to form the spectra. This range is much smaller than was used by Longo *et al.* (2008) so that a more precise estimate is obtained. It can be seen that the resulting electron energies transferred are spread out such that almost all of them are in the range 20 keV to 40 keV rather than the predicted 30 keV for the case where the electrons are at rest and Doppler broadening is not taken into account. Figure 3.4(b) shows the spectra of the energies transferred to the recoil electrons over all the scattering angles. The broadening of the energy spectrum around the Compton edge region for the case of Doppler broadening implies that some of the electron kinetic energies are greater than the theoretical Compton edge in reality. This is a deviation from the prediction by the Klein-Nishina formula (Klein and Nishina, 1929).

Table 3.1 shows the estimates of the effect of Doppler broadening on reconstructed Compton camera image resolution. Two results are shown for silicon and germanium for two incident energies, one for the resolutions of a point source modelled with the effect of Doppler broadening excluded and the other for the resolutions of a point source modelled

with Doppler broadening. Image resolution is defined as the FWHM of the reconstructed image profile. In Table 3.1, each figure represents an average value of three image resolutions of a point source obtained at three different angles (0°, 30° and 60°) of the absorber with respect to the scatterer. The idea is to evaluate the Doppler effect for different Compton camera designs. Preliminary simulations show that the image resolutions of a point source by Doppler broadening for different angles of the absorber are very similar. Hence the averages of the resolutions are reported in Table 3.1.

The case of "No broadening" for Si and Ge represents the image resolutions of the point source which would be obtained by a camera that is capable of measuring the exact energy depositions and positions of interactions in the scatterer and absorber without any detector uncertainty. This camera can be thought of as an 'ideal camera'. The resolution for this camera is very high and estimated as 0.58 mm FWHM. The high resolution of the ideal camera is greatly reduced by the inclusion of Doppler broadening at 140.5 keV. For the case of the silicon detector ("Broadening (Si)"), the FWHM is now 7.3 mm. This result is in good agreement with that published by An *et al.* (2007), that is, 7.3 mm vs. 7.99 mm. The resolution is further degraded to 12.3 mm FWHM when the scatterer is germanium ("Broadening (Ge)") rather than silicon. However, if a 511 keV source is used instead of a 140.5 keV source, then the FWHM is improved to 2.3 mm when using a silicon detector

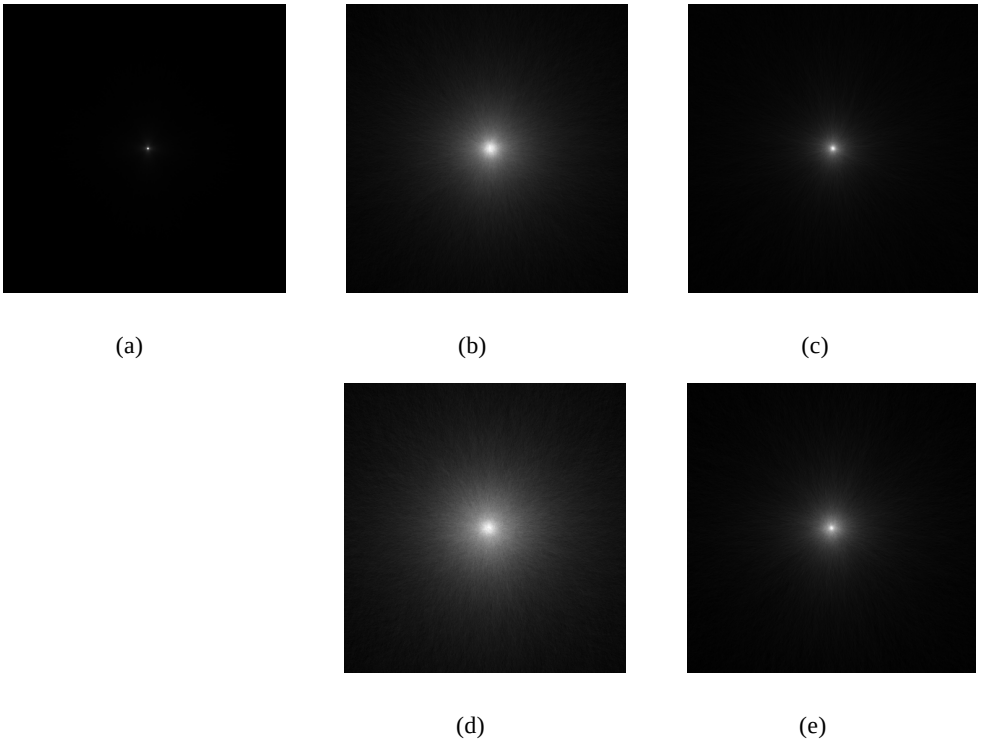

Figure 3.5: Reconstructed point source images from simulated Compton camera (a) with ideal camera. (b) with Doppler, scatterer is Si and incident photon energy 140.5 keV (c) with Doppler, scatterer is Si and incident photon energy 511 keV (d) with Doppler, scatterer is Ge and incident photon energy 140.5 keV (e) with Doppler, scatterer is Ge and incident photon energy 511 keV

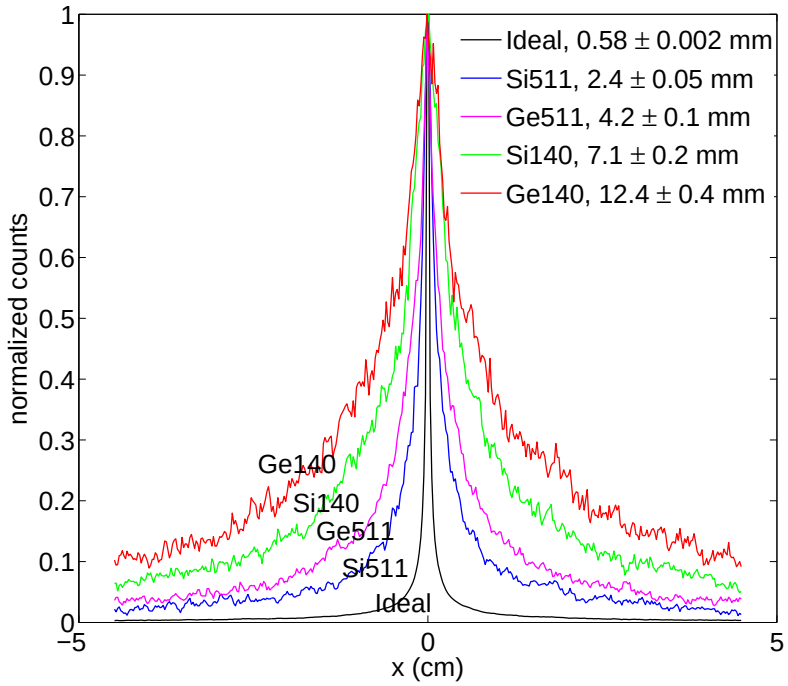

Figure 3.6: The cross section profiles of reconstructed images of a point source obtained for different scattering media and incident photon energies.

("Broadening (Si)") and 4.2 mm when using a germanium detector ("Broadening (Ge)").

Figure 3.5 shows the effect of Doppler broadening on the reconstructed Compton camera images for the case where the absorber is parallel (i.e., at 0°) with the scatterer. Note that the point source image in Figure 3.5(a) can only be seen by careful observation. Figure 3.6 shows the respective image profiles of the reconstructed point source images. In this figure, one image profile is used to represent the case of the ideal camera because, as indicated in Table 3.1, they all have similar profiles. The terms Ideal, Si511, Ge511, Si140 and Ge140 represents the case of the ideal camera, with silicon and germanium detectors at 511 keV and 140.5 keV.

The results above give credence to the fact that the Compton camera scatterer parameters need to be well accounted for, in order for the camera to match or surpass the Anger camera with respect to image resolution. It is acknowledged that tremendous effort has been invested to account for the Doppler effect in the reconstruction algorithms. An example is the analytic solution proposed by Hirasawa and Tomitani (2003). However, the group's reconstruction algorithm does not appear to take detector configuration into account. Wilderman *et al.* (1998b) attempted to overcome this limitation by using the list-mode expectation maximization reconstruction method. Nevertheless, the time of convergence for this reconstruction method is presently clinically unacceptable for Compton cameras. Hence more robust reconstruction algorithms are still needed.

3.3 Analyses to determine the optimal scatterer geometry

A scatterer geometry that allows high fraction of one Compton scattering in the detector would make an optimal geometry for the Compton camera. Hence, investigations have been carried out to determine the optimal scatterer geometry with respect to the percentage of incident gamma rays that interacted with two scatterer materials (Si and Ge) with only one Compton scattering. Information gained from these analyses would allow the prediction of the optimal geometry for the scatterer model. Note that these evaluations do not include the source-to-scatterer distance and the surface area of the scatterer which are not needed to achieve the goal of this thesis. Thus, the scatterer thickness that produces the highest percentage fraction of one Compton scattering is the optimum set-up.

For this investigation, the Compton camera geometry is maintained as described in Section 3.2.5, but this time, the thickness of the scatterer material was varied between 0 cm and 2 cm. Simulations were performed such that the major parameters of the scatterer such as energy resolution and Doppler broadening were taken into account while excluding the parameters of the absorber. Hence, only the relative efficiencies of the scatterer materials with respect to one Compton scattering in the detector were assessed for the accepted coincident events. It was also essential to ensure that only one photoelectric effect took place in the absorber. In the second evaluation, the relative fractions of multiple scatterings in the scatterer materials were assessed to determine the merits of using the materials as Compton camera scatterers. The results of these evaluations are discussed in the following section.

3.3.1 The relative efficiencies of the scatterers with respect to geometry

The graphs in Figure 3.7 show that increasing the thickness of the scatterer increases the absolute detection efficiency of the Compton camera. Figure 3.7(a) shows that the single Compton scattering efficiency of Si exhibits asymptotic behaviour with increasing detector thickness. In fact, at the thickness of 1 cm, the absolute detector efficiency is already close to its maximum asymptotic value (0.19% vs. 0.23%). Hence, beyond this thickness value there is little merit increasing the detector thickness at 140.5 keV since multiple scatterings in the detector continue to increase almost linearly as shown in Figure 3.7(b). According to these two figures, the optimum thickness for Ge is about 5 mm at 140.5 keV. This thickness is also consistent with the prediction by Harkness *et al.* (2009). Nevertheless, Ge does not appear to be the choice scatterer of choice for the Compton camera at 140.5 keV due to its lower single Compton scattering ratio resulting from its strong photoelectric interaction tendency.

On the other hand, Figure 3.7(c) shows that Ge has a better efficiency than Si at 511 keV. This time, there is no merit in increasing the thickness of the detector (Ge) beyond 1.5 cm due to its higher multiple scatterings tendency (Figure 3.7(d)). A careful look on the figures shows that an approximate thickness of 2 cm would be required for Si to match the performance of Ge at 1 cm. In any case, Si would be preferred when issues such as cost and room temperature operating conditions are taken into consideration.

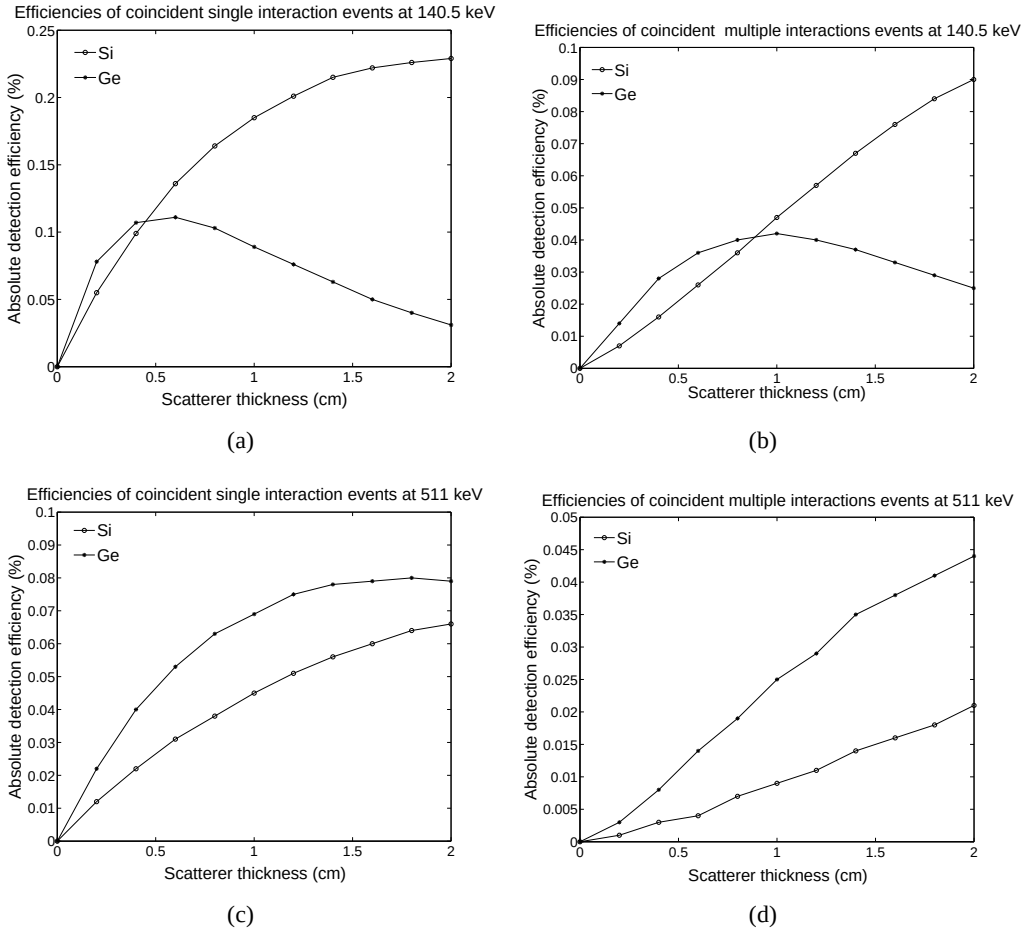

Figure 3.7: (a) The absolute detection efficiencies of Si and Ge considering only one Compton scattering in the detector at 140.5 keV, (b) considering only the multiple scatterings in the detector at 140.5 keV, (c) considering only one Compton scattering at 511 keV and (d) considering only the multiple scatterings in the detector at 511 keV.

Chapter 4

GEANT4 EVALUATIONS OF THE COMPTON CAMERA ABSORBER

Analyses in Chapter 3 have shown that Si would make an excellent scatterer for the Compton camera. Its advantages include high Compton ratio, good energy resolution and lower Doppler broadening in comparison with other detector materials. Having considered the parameters that govern the performance of the scatterer, it is also beneficial to investigate the contribution of the absorber in Compton imaging. On this note, a quantitative investigation of three detector materials, cadmium zinc telluride (CZT), thallium-doped sodium iodide ((NaI(Tl)) and germanium (Ge) as potential Compton camera absorbers is presented in this chapter. Discussions begin by highlighting the relevance of the absorber study in Section 4.1, followed by the description of the properties of the selected potential absorber materials in Section 4.2. The initial geometry of the simulated Compton camera set-up is described in Section 4.3. In Section 4.4, the description of further modifications of the camera geometry due to various absorber parameters included, as well as details of evaluations performed on the absorber materials are provided. Comprehensive results of the effects of the absorber parameters on efficiency and image resolution are presented in Section 4.5. The discussion of the results is given in Section 4.6 and Section 4.7. To assess the contribution of the absorber detector to the overall Compton camera performance, a complete Compton camera system is then modelled in Section 4.8.

4.1 The relevance of the absorber study

Seo *et al.* (2008) suggest that the selection of the absorber for the Compton camera is not a critical issue. However, there do not appear to be extensive studies on the effects of the absorber on Compton camera performance. While it could be argued that the Compton camera performance depends significantly on the operational parameters of the scatterer, an investigation (An *et al.*, 2007) suggests that there might be some merits to study the effect of the absorber parameters at higher gamma ray energies. Complete optimization of a Compton camera system must include proper evaluation of the effects of the absorber.

Table 4.1: Detector material properties, μ is the linear attenuation coefficient

Property	Si	CZT	Ge	NaI(Tl)
effective atomic number	14	50	32	49
density (g cm^{-3})	2.33	5.81	5.32	3.67
$\mu_{100\ \mathrm{keV}}$ (cm^{-1})	0.33	9.14	2.95	6.62
$\mu_{600\ \mathrm{keV}}$ (cm^{-1})	0.19	0.46	0.40	0.30

Most proposed Compton camera absorbers are based on the Anger camera scintillation detectors (Chelikani *et al.*, 2004; Zhang *et al.*, 2004) or an array of solid state detectors with pixel sizes in the range of 1 mm to 10 mm (Du *et al.*, 2001; An *et al.*, 2007). To be successful, the requirements of a Compton camera absorber should surpass those of the Anger camera because the Compton camera absorber faces challenges that result from detector uncertainties in the scatterer apart from the usual radiation background from tissues under examination. Since the higher sensitivity of the Compton camera over the present gamma systems is well established (Singh, 1983; Chelikani *et al.*, 2004), optimization procedures should focus on ways of improving resolution without compromising sensitivity. Apart from the geometrical optimization, better resolution in Compton camera systems can be achieved in two ways: accounting for the energy resolution and Doppler broadening of the scatterer at lower diagnostic energies using signal processing (Wilderman *et al.*, 2001; Hirasawa and Tomitani, 2003), and using a high performance absorber at higher diagnostic energies, although at some sensitivity compromise. The latter is the primary focus of this chapter.

4.2 The physical properties of the selected detector materials

The relevant physical properties of the detector materials used for this study are shown in Table 4.1. Si is used as the scatterer, while CZT, Ge and NaI(Tl) are potential absorbers. NaI(Tl) is a potential absorber because of its good light output, whereas Ge has an excellent spatial resolution. CZT has been proposed as having the capability to create revolutionary advances in medical imaging (Du *et al.*, 2001), but for the small size and high cost of CZT crystals. Recently, however, reports (Chen *et al.*, 2007, 2008) have shown that large-sized and cheaper CZT crystals with even better signal output can be grown in commercial quantity using the "Travelling Heater Method". How the parameters of these absorber materials contribute to the overall performance of a Compton camera is studied herein. The goals are to estimate the contribution of the Compton camera absorber to the performance of the overall camera, as well as to propose a suitable Compton camera absorber design.

4.3 Initial camera geometry

An isotropic gamma ray source placed at 10 cm in front of a Compton camera was modelled. The prototype camera consists of a single planar 9 cm × 9 cm scatterer and a single planar

10 cm × 10 cm absorber. The material and thickness of the scatterer were set as Si and 0.5 cm whereas those of the absorber were varied depending on the type of investigation performed. The inter-detector distance between the two detectors was set at 5 cm; this distance is commonly quoted for Compton cameras with parallel planar detector designs (Zhang *et al.*, 2004; An *et al.*, 2007).

4.4 Absorber investigations

An appropriate choice of the absorber detector is very critical when designing a Compton camera because the detector parameters affect the sensitivity and resolution significantly. Consequently, a series of investigations have been performed to determine a suitable absorber material with respect to efficiency and image resolution. Investigations were done considering photon interaction type, multiple interaction occurrences and pixel size of the selected absorber materials for a variety of incident photon energies. Details of these investigations are described in the following.

4.4.1 Efficiency and thickness issues

For radiation detectors, intrinsic efficiency, ε, can be defined as

$$\varepsilon = \frac{\text{no. of interaction events with energy loss}}{\text{total no. of photons incident on the detector}} \times 100\%. \tag{4.1}$$

Ignoring the effect of dead time on detector efficiency, it is possible to estimate the suitable absorber thickness from Equation 4.1; hence, the absorber thicknesses, t, were calculated as

$$t = -\ln\left(1 + (0.01)\,\varepsilon\right)/\mu, \tag{4.2}$$

where μ is the linear attenuation coefficient obtained from data provided by National Institute of Standards and Technology (NIST) photon cross section database (Berger *et al.*, 2010). Intrinsic efficiency, ε, was assumed to be at least 60% to ensure that a reasonable fraction of incident photons interact with the absorber materials in a given set of photon emission histories (Stickel and Cherry, 2005). This criterion was implemented in Equation 4.2 and the results show that the thicknesses of 0.3 cm to 3 cm would be suitable for the selected absorber materials in the energy of 100 keV to 600 keV, representing the nuclear medicine energy range. These thicknesses provide a guide for a suitable absorber.

To perform the efficiency analysis, the scatterer was removed (for this evaluation only) from the camera arrangement, allowing incident photons of an isotropic point source which is now positioned in front of the absorber material to impinge on the absorber directly. Intrinsic efficiencies were analyzed in terms of the energy and types of interactions an incident photon could undergo in the absorber in the energy range of 100 keV to 600 keV. Note that this energy range was just used to determine the appropriate absorber thicknesses in the nuclear medicine energy range. Every other analysis was performed at two real nuclear

medicine energies, 140.5 keV and 511 keV, representing the photon energies of technetium-99m and fluorine-18 radioisotopes respectively.

4.4.2 Resolution issues

In order to fully characterize the degrading effects of the absorber spatial resolution on the image resolution, modelling was first done such that no detector (scatterer and absorber) parameter was taken into account, that is, a 'perfect' scatterer and a 'perfect' absorber were assumed. This Compton camera model, as has been stated in Chapter 3, Section 3.2.5 can be thought of as an 'ideal Compton camera'. That is, a camera that is able to record exact positions of interactions and exact energy depositions of only the photon events that interacted with one Compton scattering in the scatterer and one photoelectric absorption in the absorber. The idea is to estimate the performance of the camera before the inclusion of detector parameters that degrade the resolution of the source image.

Next, two different simulations were performed to determine the effect of the absorber spatial resolution on the image resolution. The first simulation was performed such that only the effect of the multiple scatterings in the absorber was taken into account. By multiple scatterings, we mean Compton scattering(s) followed by photoelectric absorption and all other energy deposition processes ended with complete photon absorption in the absorber. The simulated energies and positions of interactions were then recorded to an output file for image reconstruction. For the second simulation, the absorber detector was segmented into equal pixel sizes to study the effect of the pixel size on image resolution. The size of the pixels was varied from 1 mm to 3 mm. Certain assumptions were also made based on currently available technologies, notably the depth of interaction resolution which refers to the accuracy with which the detector is able to measure the true position of interaction within the thickness of the detector was assumed to be 5 mm for NaI(Tl) (Majewski *et al.*, 2003) and 0.5 mm for CZT and Ge (Du *et al.*, 2001; Ghogali *et al.*, 2004). The positions of interactions were then extracted as the centre positions of the pixels where the interactions occurred. Note that for these simulations the scatterer was still assumed perfect. The simulated energy and position data were then processed on an event basis using a list-mode back-projection algorithm explained in Section 2.9.3. The algorithm analyzed each parameter of the event data to reconstruct a source image. Image resolutions were estimated using the average of full-width-at-half-maximum (FWHM) values of the horizontal and vertical image profiles of the reconstructed source image. The reconstructed resolution of the source was then evaluated for each of the absorber materials on the basis of multiple interaction occurrences and different pixel sizes.

4.5 Results of absorber simulations

The results of the absorber studies are presented in the following order. The efficiencies of the selected absorbers are first presented in Section 4.5.1 and then, the resolution results in

Table 4.2: The efficiencies of the absorber materials obtained from GEANT4 simulations. ε stands for the intrinsic efficiency and ε_{phot} stands for the photo-peak efficiency.

					Assume $\varepsilon = 100\%$		
Energy (keV)	Thickness (cm)	Material	ε (%)	ε_{phot} (%)	Compton (%)	Photoelectric (%)	Multiple scatter (%)
100	0.3	CZT	93	86	8	86	6
		NaI(Tl)	83	74	11	84	5
		Ge	56	48	14	72	14
	0.5	CZT	99	91	8	86	6
		NaI(Tl)	95	85	10	84	6
		Ge	74	65	12	72	16
600	2.0	CZT	59	35	40	13	47
		NaI(Tl)	44	22	49	14	37
		Ge	53	20	65	3	32
	3.0	CZT	73	51	31	13	56
		NaI(Tl)	58	34	41	14	46
		Ge	68	31	54	3	43

Section 4.5.2 (presented in terms of effects of multiple scatterings and pixel size).

4.5.1 Efficiency results of the absorber

The efficiencies of the absorber materials as determined from GEANT4 simulations are shown in Table 4.2. For the purpose of analysis, the fraction of the photons incident on the absorber that interacted with energy loss is normalized and recorded as 'Compton', 'Photoelectric' and 'Multiple scatter' which represent the fractions that underwent Compton scattering, single photoelectric interaction and multiple scatterings, respectively.

As Table 4.2 highlights, the intrinsic efficiency, ε, decreases with an increase in energy and CZT demonstrates the highest intrinsic efficiency. However, the intrinsic efficiency comparison between NaI(Tl) and Ge is not straightforward. The former demonstrates higher intrinsic efficiency at 100 keV while the opposite is true at 600 keV. However, Compton camera sensitivity is not assessed with respect to intrinsic efficiency but photo-peak efficiency, ε_{phot}, defined for Table 4.2 as:

$$\varepsilon_{phot} = \frac{\text{sum of single photoelectric and multiple scattering events}}{\text{total no. of photons incident on the detector}} \times 100\%. \qquad (4.3)$$

Note that the sum of the denominator excludes the events by Compton scattering only. It is then obvious in Table 4.2 that, unlike the intrinsic efficiency, the photo-peak efficiency of NaI(Tl) is greater than that of Ge for both incident photon energies. These efficiency results are consistent with the theoretical prediction by Berger *et al.* (2010) as illustrated in Figure 4.1. Hence at 100 keV and 5 mm thickness, the photo-peak efficiency, ε_{phot}, of CZT is slightly higher than that of NaI(Tl), and about 1.4 times that of Ge, but increases to about 1.6 and 1.8 times at 600 keV and 2 cm thickness of the materials respectively, as calculated

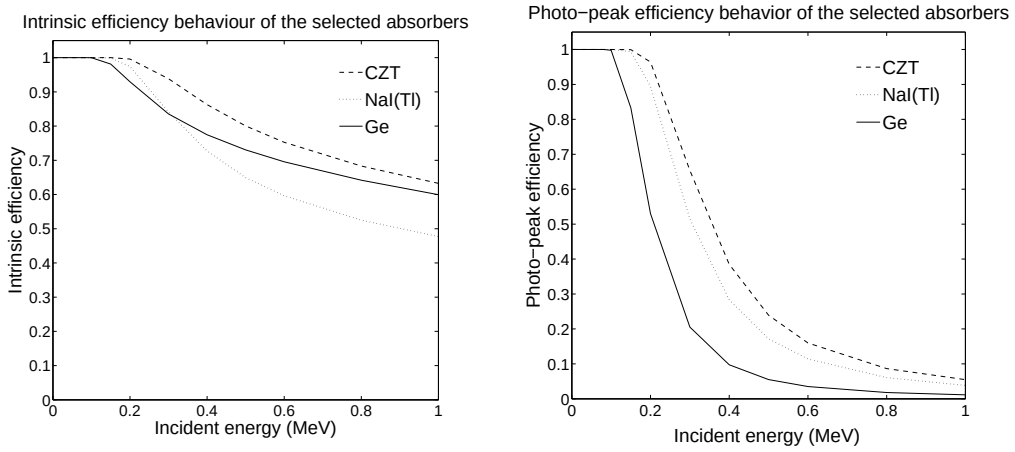

(a) (b)

Figure 4.1: (a) A theoretical graph of the intrinsic efficiencies of the selected absorber materials, (b) A theoretical graph of the photo-peak efficiencies of the selected absorber materials.

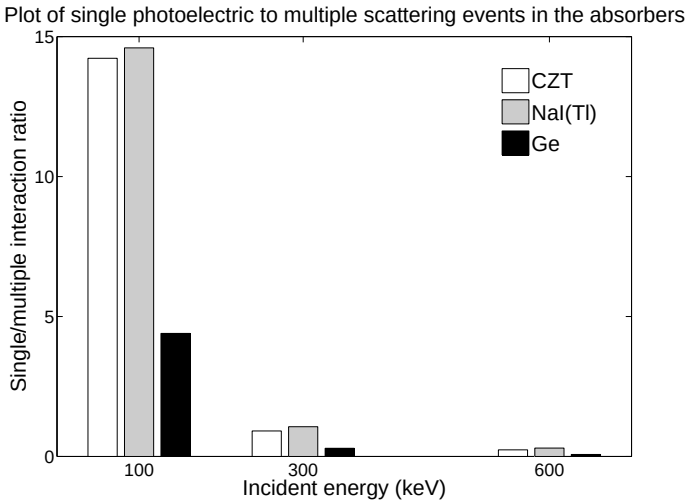

Figure 4.2: The plot of single/multiple event ratio as a function of energy.

from Table 4.2. Since CZT and NaI(Tl) have comparable single-photoelectric fractions over the energy range, it is also instructive to maximize the ratio of single photoelectric to multiple events for each set of photon histories. This is illustrated in Figure 4.2 and the implications for the Compton camera sensitivity are discussed in Section 4.6.

Figure 4.3 shows the number of photons that interacted with the absorber materials with respect to interaction depth. The graphs in the left column are based on the intrinsic efficiency defined by Equation 4.1 and the graphs in the right column are based on the photo-peak efficiency defined by Equation 4.3. The graphs are based on 1×10^6 incident photons, and each point is calculated by binning all photon absorption counts within $\pm$ 0.25 mm of the nominal depth (100 keV) or $\pm$ 0.5 mm of the nominal depth (600 keV).

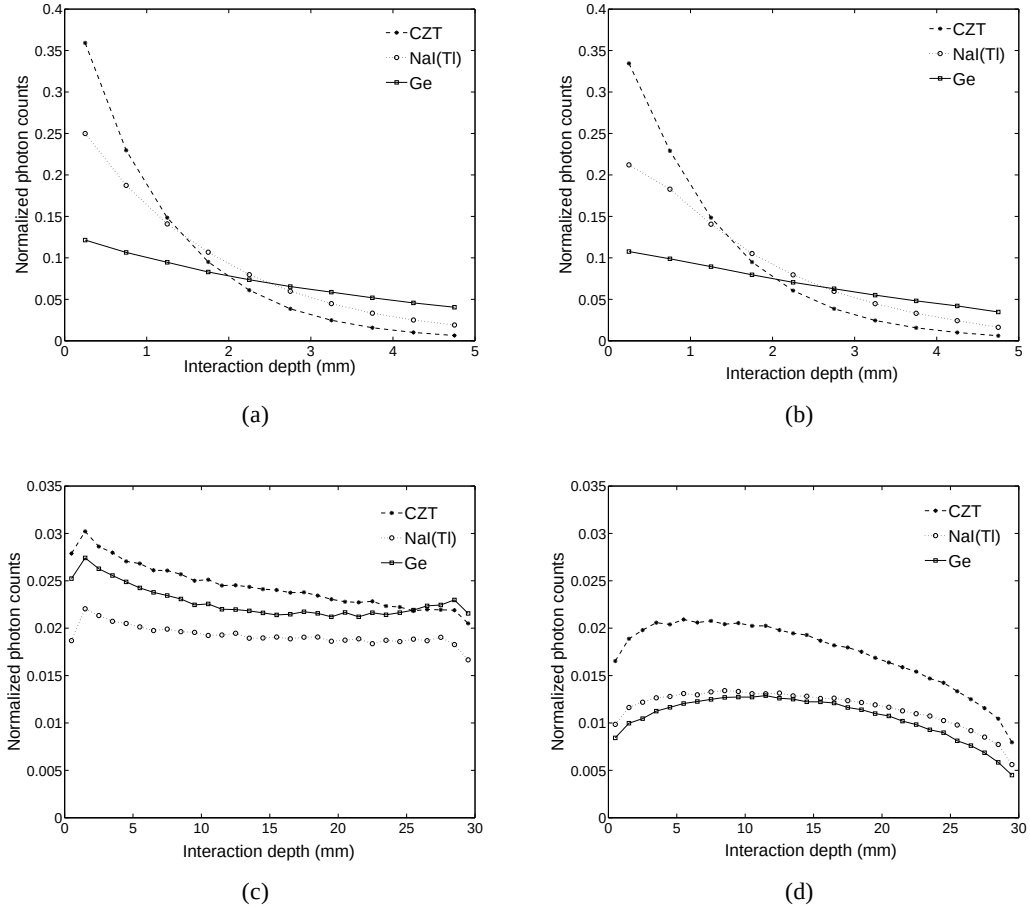

Figure 4.3: The number of photon interactions as a function of interaction depth. Left column graphs are for the intrinsic efficiency and right column graphs are for the photopeak efficiency. (a) and (b) represent the absorber thickness of 0.5 cm and incident energy of 100 keV whereas (c) and (d) represent the absorber thickness of 3 cm and incident energy of 600 keV. Note that the y-axis of (c) and (d) is rescaled to 0.035 to show clear differences in efficiencies).

4.5.2 Resolution results of the absorber

In order to appreciate the degrading effects of the absorber parameters on the reconstructed image resolution, the image resolutions of a point source produced with the ideal Compton camera at 140.5 keV and 511 keV are first shown in Figure 4.4. Note that all the reconstructed images in this chapter cover a region of 9 cm × 9 cm about the point source. FWHM value of the image resolution is shown at the top of each image. As can be seen in Figure 4.4, the image resolution of the ideal camera is estimated as 0.58 mm FWHM for both energies. Additional uncertainties in image resolution due to the absorber parameters are presented in the following.

Figure 4.5 shows the reconstructed images of a point source based on multiple scatterings in the absorber materials at 140.5 keV. As can be observed in the figure, there is virtually no change in the FWHM values by increasing the absorber thickness from 0.3 cm

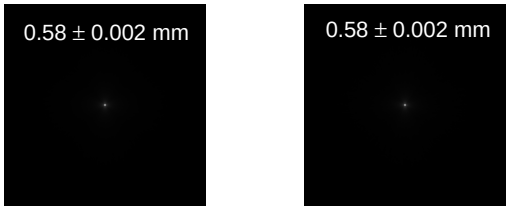

(a) (b)

Figure 4.4: The achievable reconstructed resolution of a point source image of an ideal Compton camera at (a) 140.5 keV and (b) 511 keV.

(a)

(b)

Figure 4.5: The achievable reconstructed resolution of a point source image at 140.5 keV when considering the effect of multiple scatterings in the absorber, left: CZT, middle: Ge, right: NaI(Tl). (a) Absorber thickness of 0.3 cm and (b) 0.5 cm.

to 0.5 cm, therefore the full width tenth maximum (FWTM) values were calculated and tabulated as Table 4.3 to illustrate the resolution differences more clearly. It is evident in Table 4.3, that CZT has the best resolution, followed by NaI(Tl) and then, Ge.

Figure 4.6 shows the effect of multiple scatterings on the image resolution at 511 keV. In comparison with 140.5 keV, the resolution degrades considerably with increase in the absorber thickness.

Table 4.4 shows the image resolution (FWHM) results due to the effect of pixel size of the absorber. The data is derived by varying the pixel size of the absorber from 1 mm to 3 mm. Ge shows the best resolution. Nevertheless, its performance is comparable with that of CZT, and the same at 1mm pixel size. The resolution of Ge is approximately between

Table 4.3: The achievable reconstructed resolutions of a point source image at 140.5 keV when considering the effect of absorber thickness on the image resolution. All measurements are in mm.

Image resolution	Absorber thickness					
	3mm			5mm		
	CZT	Ge	NaI(Tl)	CZT	Ge	NaI(Tl)
FWHM	1.1	1.4	1.2	1.1	1.7	1.2
FWTM	7.7	13.2	9.1	8.6	17.8	9.8

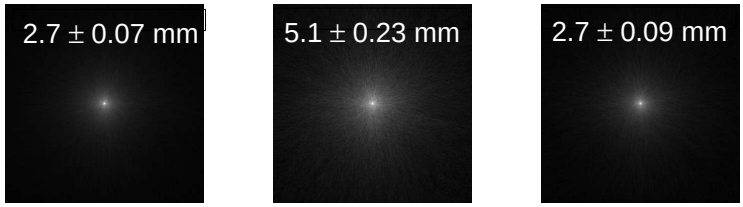

(a)

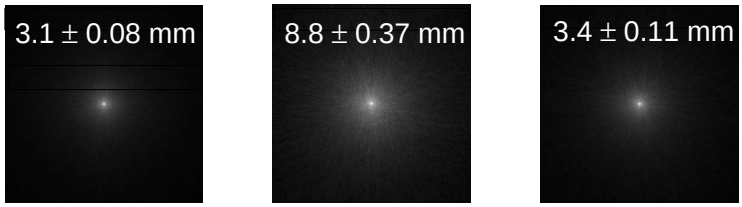

(b)

Figure 4.6: The achievable reconstructed resolution of a point source image at 511 keV when considering the effect of multiple scatterings in the absorber, left: CZT, middle: Ge, right: NaI(Tl). (a) Absorber thickness of 2 cm and (b) 3 cm.

1.5 to 3 times better than that of NaI(Tl) across 1 mm to 3 mm pixel size. On the average, detector pixelation degrades the image resolution more than the multiple scatterings but the degradation is more pronounced at 140.5 keV. It is also evident that the trend of image degradation for the two incident energies due to the detector is opposite, but less severe in magnitude than that of multiple scattering. The implications of these effects on the absorber performance are discussed with respect to efficiency and resolution in Sections 4.6 and 4.7.

4.6 Discussion of the absorber efficiency

The efficiency results of this study indicate that at 100 keV, the photo-peak and intrinsic efficiencies of the selected absorber materials are similar. But at 600 keV, the photo-peak efficiency is smaller than intrinsic efficiency due to the strong shift towards Compton scat-

Table 4.4: The achievable reconstructed resolutions of a point source image at 140.5 keV and 511 keV when considering the effect of absorber pixel size on the image resolution. All measurements are in mm.

Energy (keV)	Pixel size								
	3 mm			2 mm			1 mm		
	CZT	Ge	NaI(Tl)	CZT	Ge	NaI(Tl)	CZT	Ge	NaI(Tl)
140.5	5.3	5.2	7.5	3.6	3.4	6.5	1.9	1.9	5.4
511	4.7	4.4	6.2	3.1	3.0	5.5	1.7	1.7	4.4

tering and multiple scatterings (Table 4.2). This suggests that all the materials potentially could make good absorbers at lower radiation energies. However, the highest Compton scattering and lowest photoelectric absorption trend for Ge is a clear efficiency disadvantage relative to CZT and NaI(Tl). This trend is also illustrated in Figures 4.2 and 4.3 which confirm that Ge is not an absorber of choice for the Compton camera in terms of sensitivity, while CZT and NaI(Tl) have comparable performance. Nevertheless CZT with the highest photo-peak efficiency shows the tendency of stopping most photons close to the detector surface (Figure 4.3), which is an advantage due to its better depth of interaction resolution.

4.7 Discussion of the absorber resolution

In order to evaluate the possible impact of the absorber spatial resolution on a Compton camera, it is beneficial to examine first the performance of the camera by taking no detector parameter into consideration. This has been illustrated in Figure 4.4. The high and equal image resolutions recorded for the ideal Compton camera at 140.5 keV and 511 keV indicate that point spread function is strongly dependent on detector characteristics and incident photon energy. It is then easy to infer that the high resolution value recorded for the images is only limited by the accuracy of the reconstruction method.

Multiple scatterings in the absorber degrade image resolution as shown in Figures 4.5 and 4.6. However, it is clear in Figure 4.5 that this quantity is not a dominant image degrading factor at 140.5 keV. But at 511 keV, there is considerable increase in image degradation due to multiple scatterings in the absorber (Figure 4.6). Of the three materials considered, Ge shows the poorest resolution due to multiple scatterings. This fact is also supported in Figure 4.2 which also shows that Ge has the lowest ratio of single/multiple events. This limitation makes Ge least attractive as a higher energy absorber since the material is most prone to inter-pixel cross-talk. On the other hand, CZT shows the least positioning error because, its high photoelectric contribution to mass attenuation coefficient, and density translate to high stopping power, stopping the primary photons and secondary particles at relatively short distances between interaction sites.

Incorporating the effect of the absorber pixel sizes shows that Ge has the best image resolution (Table 4.4). This, in some way, could compensate for its poor multiple scattering resolution in the situation where the multiple scatterings occurred within the same pixel.

Nevertheless, the material's best resolution is still comparable with that of CZT, and even the same for 1 mm pixel size. The commonly used NaI(Tl) gives the worst resolution due to its poorer depth of interaction resolution.

4.8 Simulation of a Compton camera

It is instructive to relate the contribution of the absorber parameters to the performance of the whole Compton camera system. To perform this assessment, a complete Si/CZT Compton camera was modelled with all the major detector parameters of the scatterer and absorber included. The included parameters are the energy resolution, Doppler broadening and spatial resolution. Thus, how these parameters affect the image resolution of the Compton camera was evaluated separately and in combination. The choice of CZT for this evaluation is due to the outstanding qualities the material displayed in the earlier evaluations as are shown in Section 4.5. A simple diagram of the complete Compton camera is shown in Figure 4.7 and the details of the simulation are described in the following.

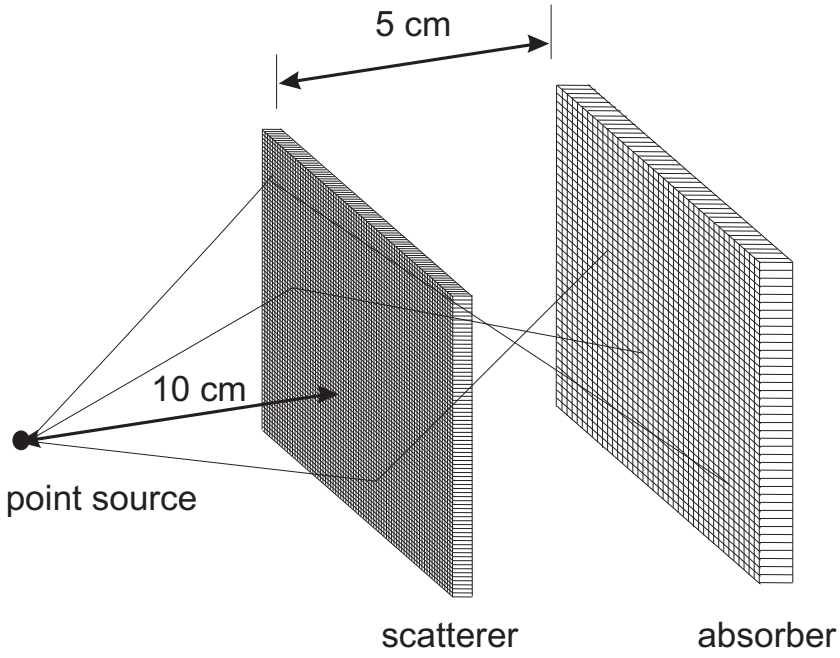

Figure 4.7: A simple diagram of the Compton camera set-up.

To simulate the complete Compton camera, the geometry and materials of the camera system were defined in the 'DetectorConstructor' class of the GEANT4 with details of the set-up described as follows: the scatterer consists of a single planar 9 cm × 9 cm × 0.5 cm Si detector, segmented into a 75-by-75 array of elements. Each pixel element is 1.2 mm × 1.2 mm in dimensions. Energy resolution was parameterized using the Gaussian distribution, and was assumed to be 1 keV at 140.5 keV and 2 keV at 511 keV (Meier *et al.*, 2002; Studen *et al.*, 2003) for Si. Position measurements in the scatterer were estimated as the centre location of the pixels in which the interactions occurred. The absorber de-

tector consists of 10 cm × 10 cm × 1.8 cm CZT detector segmented into 40-by-40 array of elements. Each pixel element is 2 mm × 2 mm in dimensions. Energy resolutions of CZT were assumed to be 3.7 keV at 140.5 keV and 5.1 keV at 511 keV respectively (Chen *et al.*, 2008). The size of the absorber pixels (denoting x- and y- positions) and its depth of interaction resolution (z- position, found within 0.5 mm accuracy (Du *et al.*, 2001)) were used to estimate the spatial resolution. The simulated energy and position data were then processed with the list-mode backprojection reconstruction method whose algorithm has been described in Section 2.9.3. A comparison was then made to assess the performance of the absorber with that of the whole camera system.

4.8.1 Effects of the Compton camera parameters on image resolution

The image resolutions due to the effects of the major detector (scatterer and absorber) parameters of the simulated Compton camera are shown in Figure 4.8. In the figure, the effects of the disturbing camera parameters to an otherwise ideal Compton camera are shown separately. It is shown that Doppler broadening, energy resolution and spatial resolution account for 7.10 mm, 8.53 mm and 6.10 mm FWHM image degradation respectively at 140.5 keV. It is also evident that while the spatial resolution accounts for the least image degradation at 140.5 keV, the contribution due to this parameter is quite significant (5.52 mm FWHM) at 511 keV. At this energy, the contributions due to Doppler broadening and energy resolution are only about 2.43 mm and 1.85 mm. The image resolutions for all these detector parameters combined is shown in Figure 4.9. The comparisons between the results of the present study with previous studies are made in Section 4.8.2.

4.8.2 Camera assessment in terms of the image resolution

Table 4.5 compares the results of this study with those of An *et al.* (2007) and Wilderman *et al.* (1998b). The low resolution values due to Doppler broadening and energy resolution

Table 4.5: The achievable reconstructed resolutions of a point source image due to the detector (scatterer and absorber) parameters at 140.5 keV and at 511 keV.

Incident energy (keV)	Research group	Doppler broadening (mm)	Energy resolution (mm)	Spatial resolution (mm)	All parameters combined (mm)
140.5	present study	7.10	8.53	6.10	18.36
	An (2007)	7.99	8.74	16.50	20.30
	[a]Wilderman (1998b)	-	-	-	14.00
511	present study	2.43	1.85	5.52	8.22

[a] Wilderman *et al.* (1998b) presented the results of all the detector parameters combined with and without Doppler broadening in their study.

suggest that accounting for the inherent scatterer parameters would significantly improve image resolution at 140.5 keV. These resolution results agree reasonably with those published by An *et al.* (2007). But there is a strong disparity between the resolution results

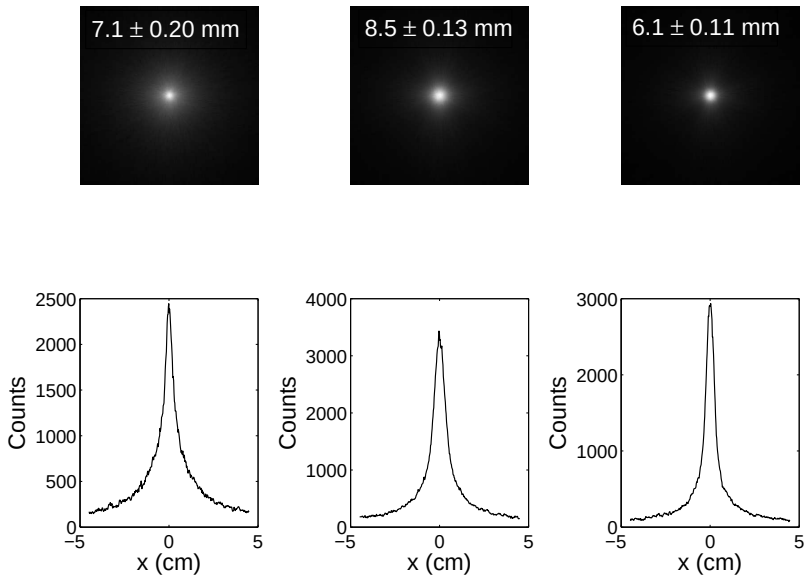

(a)

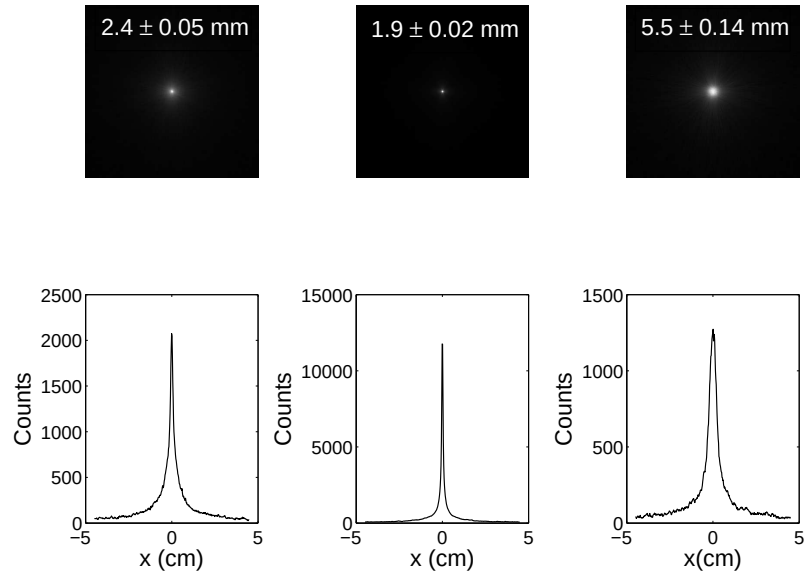

(b)

Figure 4.8: The effect of detector parameters on the image resolution, left: with Doppler broadening, middle: with energy resolution, left: with pixelation. (a) at 140.5 keV and (b) at 511 keV.

due to spatial resolution obtained from both studies. The reason is due to the smaller-pixel detectors used in this work against the large pixels, 3.125 mm × 3.125 mm for the scatterer and 10 mm × 10 mm for the absorber used by An *et al.* (2007). The overall im-

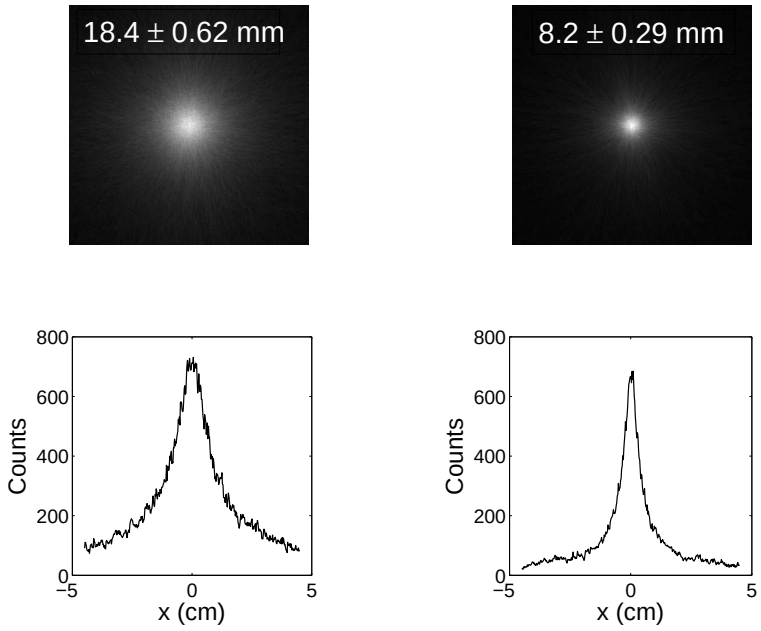

Figure 4.9: The effect of all the detector parameters combined on the image resolution, left: at 140.5 keV and right: at 511 keV.

age resolution of our design is therefore slightly better than An *et al.* (2007) camera (i.e. 18.36 mm vs. 20.30 mm). Nevertheless, the fact that the relatively smaller detector pixels used in this work could not improve the present camera's overall image resolution significantly is a strong indication that the scatterer has much more influence on image resolution at lower diagnostic energies than the absorber. On the other hand, the present camera's overall image resolution is worse than the result published by Wilderman *et al.* (1998b) (18.36 mm vs. 14 mm respectively) for a similar experimental setup except for a different absorber geometry and material (cylindrical and NaI respectively). Certain conditions could contribute to the group's better resolution result. They assumed a better energy resolution value for their scatterer (0.25 keV) which implies a better angular resolution, and accordingly, a better image resolution for their model.

It is noteworthy that while the spatial resolution accounts for the least image degradation at 140.5 keV, the reverse is the case at 511 keV. At this energy, the effects of Doppler broadening and energy resolution are significantly reduced and the overall image resolution is 8.22 mm. Recall that it has been shown in Table 4.4, that the 2 mm × 2 mm pixelated CZT alone contributes as much as 3.1 mm FWHM to image degradation for CZT, which indicates that the image resolution at 511 keV is significantly affected by the absorber parameters. Now considering that the effects of the Doppler broadening and energy resolution are smaller, inherent and cannot be improved easily by manipulating the detector electronics, it is then instructive to infer that an improvement of the absorber spatial resolution

would significantly improve the overall image resolution at 511 keV. This confirms the predictions by An *et al.* (2007) who state that the use of a higher energy gamma source such as ^{18}F emitting 511 keV annihilation photons, together with further reduction of segmentation of the absorber down to few millimetres or less, could achieve the image resolution of 5 mm required in medical imaging. Nevertheless the achievement of such image resolution may also require a better reconstruction algorithm than the simple backprojection algorithm used in this study.

4.8.3 Camera assessment in terms of the angular resolution measurement (ARM)

It is also advantageous to validate the performance of the camera with respect to the angular resolution measurement (ARM) since this metric is independent of the reconstruction method used in producing the image. As is stated in Section 2.5, ARM refers to the accuracy with which the cone parameters are determined from the measurements of the positions and the energies deposited in the detectors (Seo *et al.*, 2010). The metric was evaluated for each gamma ray event by comparing the difference between the true scattering angle θ_{Comp}, derived with the Compton formula and the measured scattering angle θ_{Geom}, defined by the location of the gamma ray source and the hit positions. The FWHM of the distribution of θ_{Comp} - θ_{Geom} provided the angular resolution of the camera (Watanabe *et al.*, 2005).

The contributions of Doppler broadening, energy resolution and spatial resolution to the angular resolution are estimated as well. The Doppler contribution is estimated by performing simulations with the LowEnergy physics package of GEANT4 with the other parameters excluded. To estimate the contribution due to the energy resolution, the deposited energies in the scatterer were sampled with a Gaussian random number generator (G4RandGauss function) provided in GEANT4, with mean equal to the deposited energy and width (FWHM) equal to the detector energy resolution. Note that the energy resolution of the absorber of the camera was not considered in this case as it does not limit the angular resolution as the energy resolution of the scatterer does. This idea is also implemented by Studen (2005a) in his PhD thesis and by Lee *et al.* (2009). The authors approximated the angular resolution due to the energy resolution only from the energy resolution of their scatterers. However, this idea cannot be used in cases where the incident radiation energy is not known. In such cases, the energy resolution of the absorber is very relevant (Mundy and Herman, 2010). The contribution of the spatial resolution is estimated by analyzing the difference between the true hit positions and the centre positions of Si and CZT pixels.

Table 4.6 shows the simulated results of the three contributions to ARM at 140.5 keV and 511 keV. The table is categorized into incident gamma ray energy, research group and detector parameter under consideration. Two results are shown for the present study, one calculated with small angle bins of 0.1° width and the other with large angle bins of 1.0° width. As already shown in Section 3.2.5, Figure 3.1, the angular resolution estimates derived with the small angle bins of 0.1° show good agreement with the theoretical prediction

Table 4.6: Angular resolution estimates of an isotropic gamma point source located at 10 cm in front of the scatterer. Incident photon energies are assumed to be 140.5 keV and 511 keV for various detector parameters.

Incident energy (keV)	Research group	Doppler broadening (deg.)	Energy resolution (deg.)	Spatial resolution (deg.)	Combined parameters (deg.)	Measured result (deg.)
140.5	a	2.0	5.2	2.0	8.6	-
	b	3.0	5.3	2.5	9.1	-
	c	8.0	4.4	2.4	9.6	9.1
	d	3.4	4.6	-	-	-
511	a	0.6	0.6	1.9	2.7	-
	b	2.3	1.1	2.4	3.4	-
	c	2.4	1.1	2.7	3.8	3.9
	d	1.8	0.9	-	-	-

[a] Present study: Angle distributions of the contributions to ARM are binned with 0.1° width bins for these results.
[b] Present study: Angle distributions of the contributions to ARM are binned with 1.0° width bins for these results.
[c] Watanabe *et al.* (2005)
[d] Studen (2005b)

by Biggs *et al.* (1975) for Doppler broadening. Hence the smaller the bins used for analysis, the more accurate the result (because the blurring effect of binning is less marked) but less precise (since fewer counts per bin). The large bins allow comparison with previous studies by Watanabe *et al.* (2005) and Studen (2005b), however, these results are less accurate due to the large size of the bins. Figure 4.10 shows how the size of the angle bin varies with the simulated angular resolution estimate. It is apparent in the Figures, that the angular resolution value of the simulated camera varies from 1° down to 0.1°, below which the value is approximately the same. For the purpose of comparison, the energy resolution of the scatterer was adjusted to 2 keV for both incident energies and the previous results in Table 4.6 are estimated from the graphs presented by the authors (Studen, 2005b; Watanabe *et al.*, 2005).

The comparisons of the results obtained with the large angle bins with previous studies are discussed in the following. In Table 4.6, it is shown that the uncertainties due to Doppler broadening and energy resolution at 140.5 keV account for the angular resolutions (FWHM) of 3.0° and 5.3° separately. The results agree reasonably with the previous results except for Doppler broadening where the estimate by Watanabe *et al.* (2005) is more than twice the value. However, Watanabe *et al.* (2005) commented that their Doppler broadening value could be reduced by using a Compton camera detector arrangement that allows more gamma ray events with smaller scattering angles, which is the case for the present camera model where most of the scattering angles are below 80°. The small spatial resolution result for the camera model, 2.5°, implies that the image quality can be improved at 140.5 keV by accounting for the scatterer parameters in the reconstruction algorithm (Hirasawa and

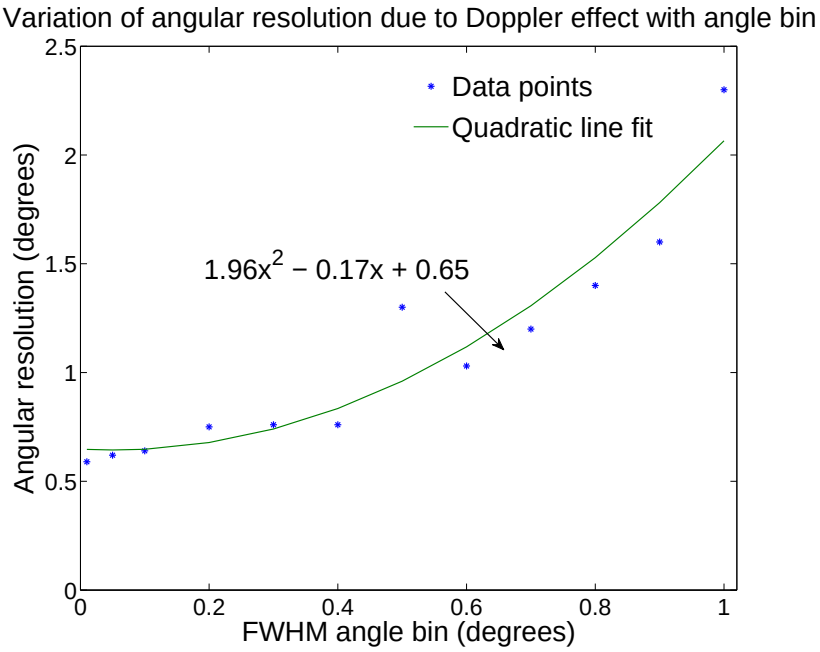

(a)

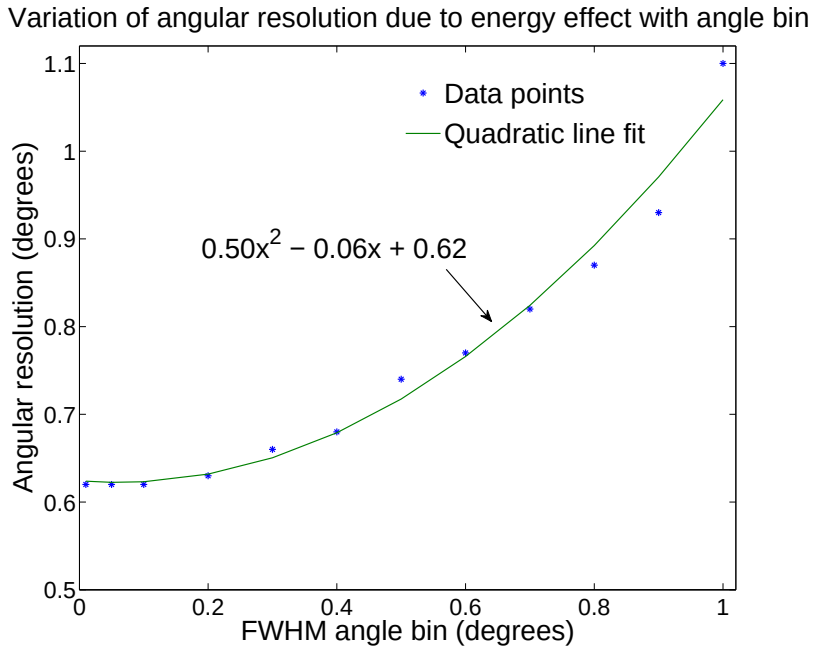

(b)

Figure 4.10: The effect of angle binning on the simulated angular resolution for (a) for Doppler broadening and (b) for energy resolution.

Tomitani, 2003). The combined effect of the parameters gives the angular resolution of 9.1° for the present camera.

At 511 keV, the uncertainty due to Doppler broadening is higher than that of the energy resolution. However, a graph of the uncertainties due to these parameters as functions of the

scattering angle by Lee *et al.* (2009) suggests an opposite trend. Certain conditions could be responsible for the disagreement. Their scatterer ($LaCl_3Ce$) is very much inferior to Si with respect to energy resolution. While the uncertainty due to the spatial resolution is smallest at 140.5 keV, the effect of the parameter is quite significant at 511 keV. At this incident energy, the effects of Doppler broadening and energy resolution are reduced, suggesting that the reduction of detector pixels at 511 keV would improve the angular resolution. However, the practical implementation of the electronic readout system for very small pixel dimensions as suggested by An *et al.* (2007) in a large volume detector would be very challenging.

Chapter 5

MODELLING OF TIMING CHARACTERISTICS OF THE COMPTON CAMERA

This chapter explores the limitations imposed by the detector energy threshold and dead time on the Compton camera performance, using a simplified model of the general electronic architecture. This is done by utilizing straightforward approximations to estimate the charge collection times and their relationship to finding coincident events, setting thresholds to reject noise, and the resultant impacts on the Compton camera performance. Note that the primary goal is not to model a complete Compton camera data acquisition (DAQ) system, but to study the limitations imposed by the physical effects mentioned above.

The first simulation paper on the timing characteristics of the Compton camera is by Park *et al.* (2010), followed by a more elaborate paper by Uche *et al.* (2011). Both studies were done without the knowledge of each other as they were published within a short time interval. This chapter is thus based on the description of these studies. Three major sections are considered. Section 5.1 provides an overview of the readout scheme. Section 5.2 details the study by Park *et al.* (2010), and Section 5.3 presents a more detailed study of the Compton camera timing characteristics by Uche *et al.* (2011).

5.1 The detector readout

In addition to simulating the radiation transport and interactions with detectors, the optimization of the Compton camera requires accurate modelling and predicting of the behaviour of the detector readout schemes. The operation of these schemes is dependent on the timing characteristics since the emitted gamma rays are detected with respect to time. The information obtained from successful gamma ray events is recorded as 'hits'. GEANT4 defines a hit as "a snapshot of the physical interaction of a track within a sensitive region of a detector". The information provided by a hit is the position and time of a step, energy deposition of the step, momentum and energy along a track, interaction type of the hit and

volume name containing the hit. A step corresponds to the trajectory of a particle between discrete interactions such as photoelectric, Compton, pair production and so on. During a step the changes to the particle's energy and momentum are calculated. The length of a step depends upon the nature of interaction, the type of particle and material and so on. If a step occurs within a volume corresponding to a sensitive detector, the interaction information between the particle and the material is stored. The entire series of steps form a simulated trajectory of a particle, that is called a 'Track' in GEANT4 (GEANT4 Collaboration, 2011).

The primary function of the readout schemes is to acquire the electrical charge pulses generated by the radiation detectors, to extract hit information and to convert them into a digital format that are then acquired, saved and analyzed by a computer. The quantities of interest are the particle energy (proportional to the charge released by the particle in the detector), position of interaction and the time of arrival. Traditionally, the electronic readout systems for particle detectors are made up of readout modules (or units). Each module has a specific function, so that one needs to interconnect several modules in order to make the system able to extract all the quantities of interest. The final value obtained after filtering by a set of these modules is called a 'Single'. Singles can be saved as output. Each transient value, between two modules, is called a 'Pulse'.

As already described in Section 2.7, depending on the characteristics of the detector readout, there is a minimum amount of time that must separate two events, detected on the same readout component, for them to be recorded as two separate pulses. This is known as the dead time. Two models of dead time behaviour, nonparalyzable and paralyzable, can be implemented on an event basis for this purpose (Knoll, 2000). The nonparalyzable model is one for which, if an event occurs during the dead time of a preceding event, then the second event is simply ignored, with no further effect on subsequently occurring events. The paralyzable model is one for which each event introduces a dead time whether or not that event actually was counted. Thus an event occurring during the dead time of a proceeding event is not only ignored but introduces its own dead time during which subsequent events cannot be recorded. How this time effect influences the Compton camera operation is described in the following.

5.2 Time characteristics of the Compton camera – the approach by a previous study

The first paper on the timing characteristics of the Compton camera is by Park *et al.* (2010) who also used the GEANT4 software as programming tool. The group accounted for the stochastic nature of the gamma ray's emission time by the formula

$$T_{i+1} = -\ln(\xi)\,\frac{1}{\gamma A(T_i)} + T_i, \tag{5.1}$$

where T_{i+1} and T_i are the $(i+1)$th and the ith gamma ray emission times, respectively, ξ is a random number from a random number generator *G4UniformRand*, γ is the emission

yield of the gamma ray in use for Compton imaging, and $A(T_i)$ is the activity (in Bq) of the source at time T_i. The exponential decay of the radiation source during imaging was modelled by calculating the activity each time before sampling T_{i+1}. The time information was stored in the *G4Step* object using the *SetGlobalTime* function. The global time was updated whenever a particle interacted with the camera's detectors. The time information was retrieved whenever necessary using the *GetGlobalTime* function of the *G4Step* object. The interaction time was sampled, considering the time resolution of the component detector, with the Gaussian distribution:

$$T' = T + \sigma_T \xi, \tag{5.2}$$

where T' and T are the measured and true interaction times, respectively, σ_T is the time resolution of the component detector, and ξ is a random number that is produced by a random number generator of standard normal distribution (*G4RandGauss*).

To model the dead time, the nonparalyzable model was used. Their detector dead time was assumed to be 1.6 μs for the scatterer and 5 μs for the absorber. The time resolutions of the scatterer and absorber were taken to be 65 ns and 10 ns respectively. Coincidence counting was determined by defining the coincidence time window of 200 ns after the application of the dead time to the signals. The digitization dead time was taken to be 30 μs. The measured interaction times at the component detectors were retrieved from the *G4Step* object using the *GetGlobalTime* function. The measured interaction times of the detectors were then compared and, if they are within a given coincidence time window, it was assumed that the interactions were caused by the same gamma ray and are then stored as an effective event for subsequent image reconstruction.

According to Park *et al.* (2010), their simulated efficiencies are in very good agreement with experiments; that is, within 1% to 2% error difference and their reconstructed image resolutions are within 7% to 13% for two point gamma ray sources at 511 keV and 1275 keV respectively, imaged at 3.7 cm in front of a prototype double-scattering Compton camera.

5.2.1 Drawbacks of the previous study

The study by Park *et al.* (2010) is however not flawless. Their use of a fixed digitization dead time value makes their simulation model less robust for wide range of event rates. Again, it has not been established that the nonparalyzable dead time model can fully characterize the dead time behaviour of the Compton camera system. The numbers of effective events also used by the group for their reconstruction are too low to give reliable results, 679 events for 511 keV and 1063 events for 1275 keV. It is also not clear why the group's simulated efficiencies without the dead time are lower than the simulated efficiencies with dead time (2.90×10^{-8} against 4.20×10^{-8} for 511 keV and 6.12×10^{-8} against 6.64×10^{-8} for 1275 keV respectively). These efficiency results imply that there are no limitations imposed by the timing characteristics of the Compton camera, which is in disagreement with earlier predictions by Leblanc *et al.* (1999) for a real C-SPRINT Compton camera. Hence a simulation study has been conducted by Uche *et al.* (2011) to address these issues.

5.3 Time characteristics of the Compton camera - the approach by the present study

The GEANT4 toolkit was used to model the camera geometry and performance for the two common nuclear medicine energies that correspond to ^{99m}Tc (140.5 eV) and ^{18}F (511 keV) radiotracers. In addition to the GEANT4 provisions, however, modifications were made to account for the photon emission times which were used to account for the detector response.

5.3.1 Simulation of detector response

To simulate the detector response, physical observables (hit information) which include energy, position, and time of detection of each interacting gamma ray were first extracted using a derived sensitive detector class in GEANT4. The energy depositions in the detectors and their corresponding detection times were then summed on a photon event basis for each detector pixel where the interactions occurred. The Poisson distribution was used to approximate the decay rates of the radiotracers (^{99m}Tc and ^{18}F), notably, decay instants drawn from the *G4Poisson* class with the appropriate decay constant, considering a source activity of 10 MBq was used to approximate the decay times. It was assumed that no atomic decay occurred before the simulation commenced, hence the initial decay time was set at zero. A derived 'RunAction' class was then used to sum subsequent decay times, which were added to the times of particle interactions in the detectors to determine the times of the energy pulses. In real detection systems however, the discrete pick-up times of pulses are also governed by noise in the system and statistical fluctuations of the signals from the detector. This timing uncertainty is known as time jitter. To account for the detector energy resolution and detection time jitter, Gaussian blurring was introduced to the pulses and their corresponding times respectively.

In order to count the pulses reliably, the concept of energy discrimination threshold was introduced. Note that the implementation of this woncept could affect the efficiency results of Chapters 3 and 4 since low energy depositions below the noise level in the scatterer will be eliminated from the data. In many counting situations, the energy theshold level is set just above the system noise so that the maximum sensitivity for

counting detector pulses is realized. Along this line, lower and upper energy thresholds of 8 keV and 50 keV were applied to the scatterer, whereas 80.5 keV and 150.5 keV were applied to the absorber at 140.5 keV respectively. The lower threshold of the scatterer is in line with the predictions by previous researchers (Studen *et al.*, 2004; Watanabe *et al.*, 2005), which suggest that a minimum energy threshold of 8 keV is required for the Compton camera scatterer (i.e. silicon) for its stable operation, and the upper threshold was to allow a greater fraction of events with single Compton scattering up to the Compton edge. The decision on the absorber energy thresholds is to allow all possible energy depositions that would add up with those in the scatterer to fall within the coincident window. The energy thresholds were adjusted to 8 keV and 341 keV for the scatterer, and 160 keV and 521 keV

for the absorber at 511 keV. The time jitters of the scatterer and the absorber correspond to experimentally measured values of 12 ns and 5 ns respectively (Studen *et al.*, 2004; Bolotnikov *et al.*, 1999). The simulated energy, position and time measurements were then saved to an output data file for the system dead time processing with MATLAB code.

5.3.2 Application of detector dead time

To simulate the detector dead time, the scatterer was functionally segmented into modules (or units) of 128 pixels each for easy identification of the positions of the signals. Signals in each module represent the pulses from the preamp/shaper application-specific integrated circuits (ASICs) and each module was treated as an independent section of the detector. The photon events were first processed with a paralyzable dead time algorithm for each scatterer module readout section. When an event signal is detected in the scatterer pixel and is undergoing processing, the module is not able to process the next signal if the time of detection occurs within a dead time interval of 1 μs from the time of the event under processing, and any new signal restarts the dead time. Signal outputs from the modules were analyzed by a second algorithm that mimics the operation of a nonparalyzable 128-channel multichannel analyzer (MCA). The dead time of the MCA is comprised of a variable processing time of the virtual analogue-to-digital converter (ADC), which is determined by the appropriate signal channel number, and a fixed memory storage time of 2 μs.

The absorber detector is functionally segmented into modules of 64 pixels each. Each module was considered as an independent section of the detector. Within the subgroup, the asynchronous pulses from the preamp/shaper ASICs compete for access to a single output channel via a 'winner-takes-all' arbitration algorithm. Each successful pulse is multiplexed to a free-running ADC. The data stream from the ADC, along with the pixel ID of the winning pixel are forwarded to the coincidence detection algorithm (Griesmer *et al.*, 2002).

The processed events from the scatterer and absorber were then read into the coincidence detection algorithm which matched coincident pulses with their respective time stamps. The algorithm also eliminated accepted events due to an incorrect scattering sequence such as Compton scattering in the absorber followed by a complete absorption in the scatterer. This was done by using the time stamps of the pulses and the corresponding pixel ID to accept the events where the hits took place first in the scatterer before the absorber. At 140.5 keV, the fraction of events with incorrect scattering sequence is less than 1%. But at 511 keV, this factor rose to about 48%, necessitating their elimination with the coincident timing algorithm. Respective pulses from the scatterer and the absorber were summed to find the photon events that meet the coincident window criteria, which are, an energy window of $\pm$10 keV around the radionuclide energy and a time window of 20 ns between the recorded pulses in the scatterer and the absorber. The matched event singles were then clocked out at a trigger rate of 10 kHz for image reconstruction. The overall system dead time was estimated using the decaying source method (Knoll, 2000) with a short-lived ^{15}O radioisotope point source as described in Section 5.3.6. The Compton camera DAQ

characteristics such as pulse pileup and time walk were not investigated in this study.

5.3.3 Modified Compton camera set-up

To investigate the effect of the timing characteristics on the prototype camera, evaluations were done based on the effect of the basic detector parameters (Doppler broadening, energy and spatial resolutions), and then with energy threshold and detector dead time. It was decided to reduce the dimensions of the scatterer due to insufficient computer memory to perform long simulations with multiple stacks of pixelated silicon strips. The modified geometry of the camera is described as follows.

The pixel size of the scatterer was not modified (LeBlanc *et al.*, 1999), but its thickness was reduced to 0.2 cm. This is in line with the prediction by Philips *et al.* (2001) who suggest that the fabrication of single Si detector strips with 0.2 cm thickness is practicable. Hence, the modified scatterer design consists of two stacks of planar 5.8 cm × 5.8 cm × 0.2 cm Si detectors, segmented into 6-by-6 detector modules. Each module consists of 128 Si pixels with 1.2 mm × 1.2 mm dimensions. Note that the optimal thickness of the scatterer as predicted in Section 3.3.1 would require five stacks of Si strips, but this geometry was not possible due to insufficient computer memory. Other characteristics of the detector are as described in Section 4.8.

The absorber dimensions were not modified, nevertheless the detector was segmented into a 5-by-5 array of detector modules. Each module consists of 64 CZT pixels with 2.5 mm × 2.5 mm pitch for each pixel element. The thickness of the absorber was set at 5 mm at 140.5 keV and 1.8 cm at 511 keV (Stickel and Cherry, 2005; Chen *et al.*, 2008; Awadalla *et al.*, 2009). Energy and spatial resolutions were implemented as described in Section 4.8. Figure 5.1 shows a simple diagram of the modified Compton camera model.

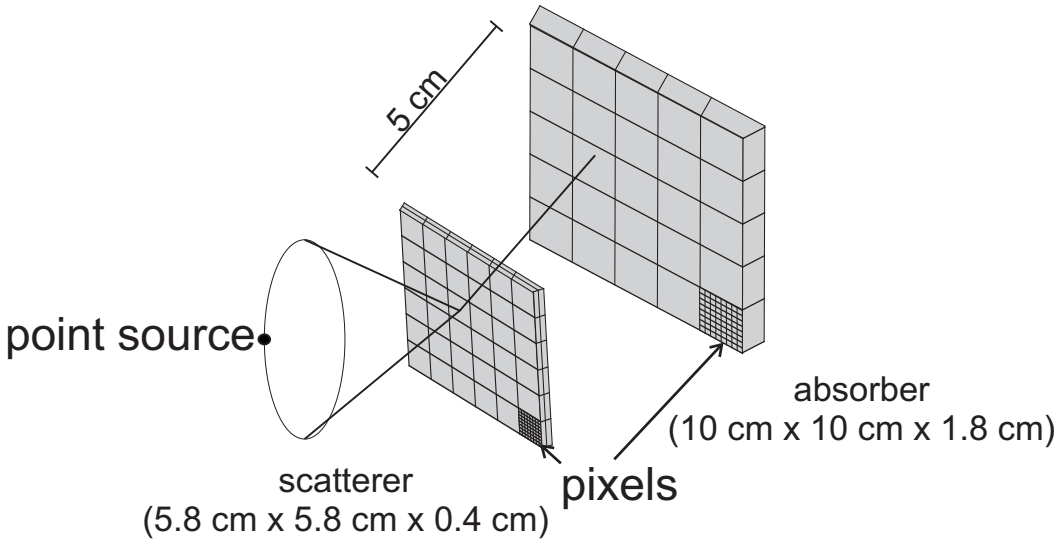

Figure 5.1: Simple diagram of the modified Compton camera set-up.

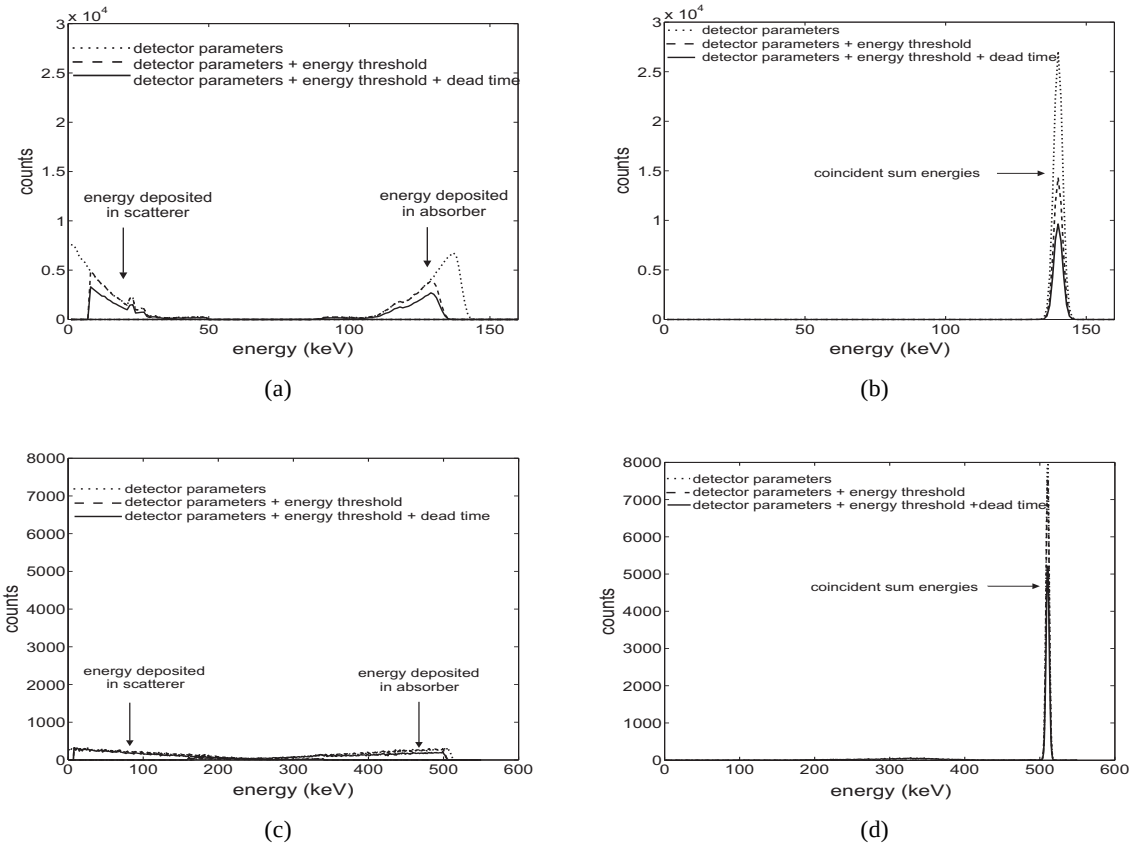

Figure 5.2: The energy spectra of 10 MBq radiotracers showing the impacts of energy threshold and dead time (a) on the scatterer and absorber efficiencies for a ^{99m}Tc (140.5 keV) point source (b) on the total efficiency for a ^{99m}Tc (140.5 keV) point source (c) on the scatterer and absorber efficiencies for a ^{18}F (511 keV) point source and (d) on the total efficiency for a ^{18}F (511 keV) point source.

5.3.4 Impact of energy threshold and dead time on the efficiency

Figures 5.2(a) and 5.2(b) show energy spectra to illustrate the effects of the detector parameters, in addition to energy threshold and dead time on Compton camera efficiency for 120 million simulated photon events for a 10 MBq ^{99m}Tc radiotracer (140.5 keV). The spectra diagrams are derived by binning the energy counts within 1 keV intervals across the distributions. The dotted spectrum line represents the efficiency estimates of studies that ignore energy threshold and dead time. The inclusion of energy threshold and dead time reduced the spectra overlap between the absorber energy and the coincident sum energy. Similar diagrams are also shown in Figures 5.2(c) and 5.2(d) for a 10 MBq ^{18}F radiotracer (511 keV).

It is apparent in these figures that the practical efficiency of the Compton camera has been overestimated by previous investigators who did not predict count rate losses under clinical conditions. The importance of the energy threshold and time effects cannot be ignored. The energy threshold is needed for the stable operation of practical Compton cameras (Studen *et al.*, 2004), specifically to discriminate noise signals and background ra-

Table 5.1: Coincident detection efficiencies of the Compton camera model.

Radiotracer (activity = 10 MBq)	Detector parameters only	Detector parameters + energy threshold	Detector parameters + energy threshold + dead time
^{99m}Tc	8.99×10^{-4}	4.67×10^{-4}	3.16×10^{-4}
^{18}F	3.84×10^{-4}	3.65×10^{-4}	3.10×10^{-4}

Table 5.2: Achievable resolutions of the camera model at source-to-scatterer distance of 5 cm.

Radiotracer energy (keV)	Resolution	Parameters only	Parameters + energy threshold	Parameters + energy threshold + dead time
140.5	Image (mm)	10.0	9.5	9.5
	Angular (deg.)	6.2	5.4	5.4
511	Image (mm)	5.3	5.2	5.4
	Angular (deg.)	3.6	3.6	3.6

diation pickup capable of causing instability of performance. The time effects are necessary for accurate accounting of count rate losses as well as matching coincident events. The application of the energy threshold at 140.5 keV reduced the camera sensitivity by 48%. This is because a significant fraction of the energy transfer to recoil electrons occurs below 8 keV. The inclusion of dead time effects further reduced the camera sensitivity by 17%. But at 511 keV, the energy threshold did not dominate count rate losses as it only reduced sensitivity by 6%, while the dead time inclusion further reduced sensitivity by 13%. The results of the coincident detection efficiency are shown in Table 5.1. The efficiency results in Table 5.1 suggest that the final efficiency of proposed camera would be at least three times more than the Anger camera.

5.3.5 Impact of energy threshold and dead time on the resolution

Table 5.2 illustrates the impacts of the count rate losses due to energy threshold and detector dead time on resolution at 140.5 keV (^{99m}Tc) and 511 keV (^{18}F). As the table highlights, the image resolution of an isotropic point source located at 5 cm in front of the scatterer is improved from 10.7 mm to 9.5 mm by including the energy threshold at 140.5 keV. These correspond to the angular resolutions of 6.2° to 5.4° respectively. The inclusion of the dead time made no impact on the resolution. At 511 keV, the subsequent inclusions of energy threshold and dead time virtually made no difference on the resolution. The plots of reconstructed images and angular resolutions for both radionuclide energies are shown in Figures 5.3 and 5.4 as examples.

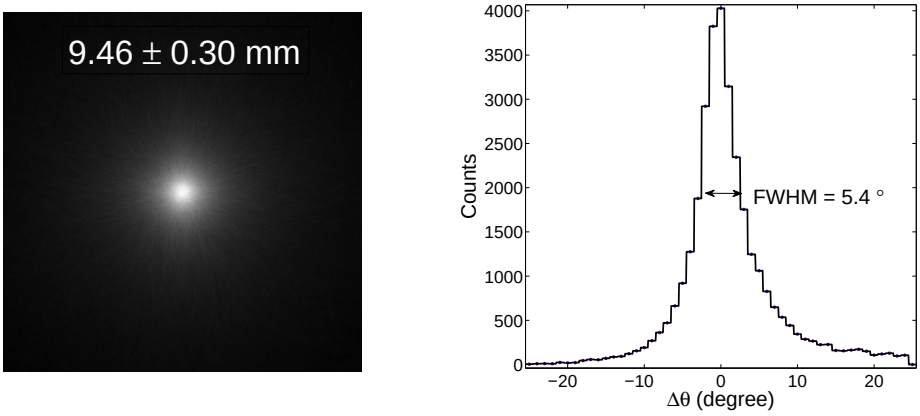

(a) (b)

Figure 5.3: (a) Reconstructed image of a point source located at 5 cm in front of the scatterer with all the effects included and (b) corresponding angular resolution at 140.5 keV.

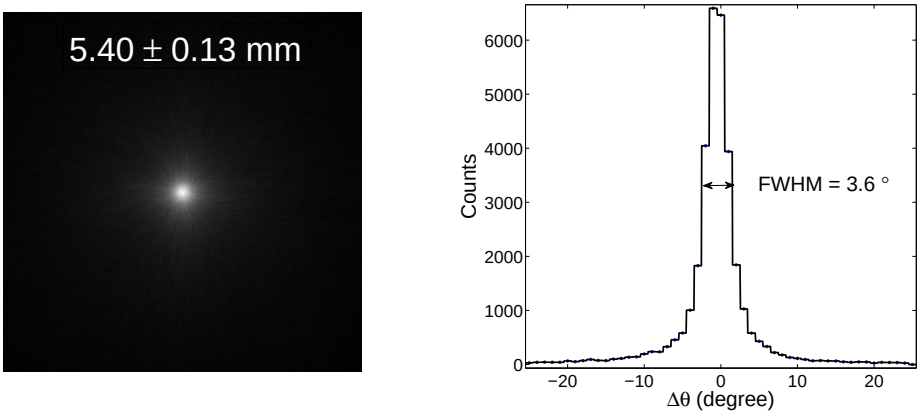

(a) (b)

Figure 5.4: (a) Reconstructed image of a point source located at 5 cm in front of the scatterer with all the effects included and (b) corresponding angular resolution at 511 keV.

5.3.6 The evaluation of system dead time

Knoll (2000) suggests that the dead time of an imaging system can be estimated by using a short-lived radioisotope source in the limit of negligible background. This is known as the decaying source method (Knoll, 2000). The method assumes that the dead time model which describes the system behaviour will fit the best straight line to the observed counting rate data. It is also suggested that this method could be beneficial for cases where the observed counting rates depart slightly from the known exponential decay of the source. Hence, Figure 5.5 is derived by recording the observed count rates R_o as a function of time t, using a short-lived 500 kBq ^{15}O radioisotope source for an acquisition period of 420 seconds. The figures illustrate the degree of fit of the dead time models to our prototype camera

data. In these figures, the paralyzable dead time model demonstrates a better linear fit to our camera data than the nonparalyzable model, with the dead time τ value of 3.1 ms, derived from the slope of the linear fit. Note that λ represents the decay constant of ^{15}O radioisotope and R^2 is the R-square value of the linear fit. The y-intercept of the nonparalyzable plot corresponds to the initial true count rate while that of the paralyzable corresponds to the natural log of the initial true count rate.

The system dead time is, no doubt, very large but not totally unexpected due to the mean trigger rate of 10 kHz (or 0.1 ms dead time) utilized for the readout buffer in Section 5.3.2. However, it had been suggested that the dead times of the first and second generation silicon pad detectors are in the range of 1 ms to 3 ms (LeBlanc, 1999). In fact, the dead time results of this study are comparable to those published for a real C-SPRINT Compton camera system (LeBlanc, 1999), that is, 3.1 ms vs. 3.8 ms for the paralyzable model and 4.8 ms vs. 8.5 ms for the nonparalyzable model. Note that the nonparalyzable dead time graph line did not fit the scattered points for both cases and therefore may not be reliable. It may even be possible that the dead time of the Compton camera system may not be completely characterized using just one dead time model. In any case, the Compton camera system dead time can be reasonably reduced by utilizing electronic readout schemes with shorter dead times. However, this must be done with caution considering the noise added by the preamplifier-amplifier combination which negates the good energy resolution of semiconductor detectors, as well as preventing event mismatching at high count rates which is even more critical. Hence, issues such as pulse pileup and time walk need to be taken in account before it can be done efficiently.

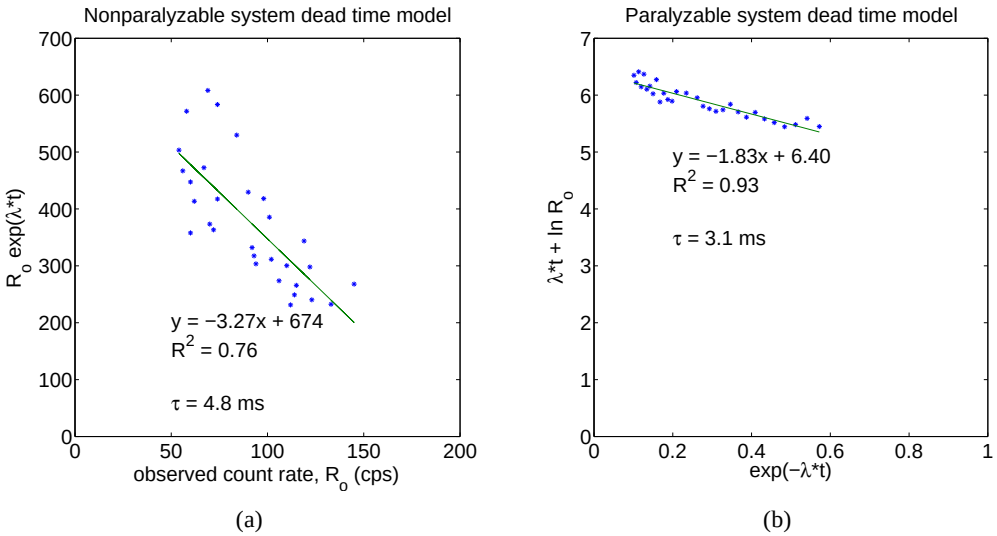

Figure 5.5: Graphs of the system dead time models, obtained by plotting observed data and corresponding linear fit for the data for (a) nonparalyzable (b) paralyzable model.

5.3.7 Limitations of the present study

While it is believed that the dead time explains the differences between the measured and theoretical sensitivity values, it is by no means suggested that this study depicts a complete modelling of the Compton camera data acquisition (DAQ) system considering the rapidly changing and ever improving developments in the designs of new front-end electronics. Also, effects such as pulse pileup and time walk were not studied. Nevertheless, the results of this study can be viewed as more realistic predictions of the Compton camera operation.

Chapter 6

COMPTON CAMERA ASSESSMENT FOR SCINTIMAMMOGRAPHY

Assessment of the performance of SPECT scanners in breast cancer imaging is a complicated task as there is no specific system designed for it. Recently, there has been widespread interest to develop compact SPECT cameras that are based on either new scintillators with very high yield such as $LaBr_3$:Ce or pixelated solid-state detector arrays such as CZT (Gruber *et al.*, 1999) for clinical use. These devices present numerous advantages over the conventional Anger cameras in imaging specific human organs, and have been shown to be potentially capable of improving the imaging of breast cancers in scintimammography (Pani *et al.*, 2006b, 2007). The use of scintimammography as an adjunct to X-ray mammography is useful in reducing the rate of false biopsies. It is recommended for breast cancer cases where additional information is required to reach a definitive diagnosis. However, even with the improved compact SPECT cameras, the very low sensitivity of scintimammography for tumours under 1 cm in diameter is a major limitation in recommending the imaging technique for breast screening purposes (Pani *et al.*, 2006b). Recently, however, Zhang *et al.* (2004) have proposed that the higher sensitivity of Compton cameras could be exploited advantageously to improve the visualization of breast tumours in scintimammography. Based on this proposal, an investigation has been conducted in this chapter to evaluate the performance of the Compton camera for scintimammography using detailed simulations.

For proper appreciation of the relevance of this study, an overview of breast cancer imaging is first presented in Section 6.1, followed by the description of scintimammography in Section 6.2. Given the numerous aspects of this study, it is clearly impossible to deal with all aspects in a short section, hence the Compton camera investigations for scintimammography are treated in Section 6.3 and a discussion of the results is presented in Section 6.4.

6.1 Breast cancer imaging

Breast cancer is ranked as the second cause of death after cardiovascular disease, and is the most common cancer among New Zealand women with more than 2500 new cases expected every year. It is estimated that 1 in 9 New Zealand women is likely to be diagnosed with breast cancer during their lifetime, making it the leading cause of cancer-related death in females. Also it was estimated that approximately 20 men were diagnosed with breast cancer in 2008 (Ministry of Health/NZHIS/BSA, 2007; Ministry of Health, 2008).

Many breast tumours can be detected by self-examination or by a clinical routine examination. Early detection and treatment improve prognosis and survival rate, and this has motivated the implementation of screening tests and improved methods of staging therapy. However, depending on the size of the breast and the density of breast tissue, most tumours do not become palpable until greater than 1 cm in diameter (Donegan, 1992). If the primary screening technique, X-ray mammography, detects a possible tumour, further diagnosis will need to be obtained by biopsy. Biopsy can determine whether the structure is cancerous, and if so, can also determine the type of cancer and thereby aid in treatment selection. However, biopsy is time consuming for the physician, often uncomfortable for the patient, and can increase the patient's radiation exposure. Of most biopsies performed every year, only about 25% find cancer. This has lead many breast cancer experts to conclude that better diagnostic imaging techniques are still needed (Fisher *et al.*, 1983; Morris and Malt, 2000). Consequently, a number of imaging procedures have been introduced to improve diagnosis of breast cancer, which includes ultrasound, magnetic resonance imaging and positron emission mammography. However, beside the high cost of medical equipment, another critical limitation of these imaging procedures is that they do not allow for accurate differentiation between benign and malignant tumours in dense breasts.

6.2 Scintimammography

Scintimammography is a functional imaging technique wherein a radiotracer is introduced into the patient's breasts and axillary nodes, and observed with a radiation detection camera. Radiotracers are designed so that they tend to accumulate in tumours more than in healthy tissues, hence the images that are taken can visualize tumours and aid in diagnosing the presence or absence of breast cancer.

Research has shown that scintimammography imaging can accurately diagnose primary breast cancer, demonstrating sensitivities of 80% to 94% and specificities of 73% to 93% (Khalkhali *et al.*, 2000; Taillefer *et al.*, 1995). Investigations further suggest that the imaging technique performs equally well when used to evaluate the axillary lymph nodes (Kao *et al.*, 1994; Lam *et al.*, 1996; Palmedo *et al.*, 1996).

While researchers agree that scintimammography will not replace X-ray mammography as a mass screening tool, many believe that a good number of patients can benefit from it. One such group of patients is those with dense, glandular breasts wherein the sensitivity

of X-ray mammography is impaired. Another group is those with breast implants, since scintimammography is permeable to implants (Pani *et al.*, 2006b). It is also possible to use scintimammography for post-surgery discrimination between tumour recurrence and scar tissue since scarred breasts are poorly imaged with X-ray mammography.

The above advantages notwithstanding, scintimammography has presently not been introduced as a routine examination in many nuclear medicine centres (Pani *et al.*, 2006b). The reason is due to its currently low sensitivity for detecting cancer tumours of less than 1 cm diameter as there is no specific equipment designed for it. The problem of very low sensitivity of scintimammography for tumours under 1 cm diameter is not trivial, the ability to visualize small breast cancers is really crucial to the patient's survival and more clinical use of scintimammography. Another major limitation is the use of Anger cameras for performing scintimammography (Pani *et al.*, 2006a). It is believed that the number of false negatives (i.e., missed tumours) could be reduced if the limitations of Anger cameras could be overcome. This problem has been partly addressed with compact gamma systems which reduce large dead spaces between the photomultiplier tubes in Anger cameras (Pani *et al.*, 2006a,b, 2007). Nevertheless, the use of compact imaging cameras with wider fields of view and higher sensitivities would be more advantageous.

6.3 Compton cameras for scintimammography

The Compton camera has been shown to be a suitable candidate to replace the Anger camera for scintimammography. This is demonstrated by Zhang *et al.* (2004) who showed that the camera's higher sensitivity and adequate resolution is able to address the problem of very low counts often recorded for breast tumours less than 1 cm in diameter which, time and again, leads to poor or no visualization of tumours, especially for the breast tumours located at the medial region of the breast or close to the chest wall.

Previous simulation studies of the Compton camera did not account for the spatial resolution due to the photomultipliers since they did not include the modelling and collection of scintillation photons by the photomultipliers. Consequently, resolution has been worse than predicted in the actual implementation of Compton cameras that are based on scintillation detectors since the dead zones between neighbouring photomultipliers are not accounted for (LeBlanc *et al.*, 1998). It is for a similar reason that Pani *et al.* (2006a, 2007) reported that large and bulky detectors as used in Anger cameras have not been very successful in scintimammography.

To improve the work of Zhang *et al.* (2004), the group's large sodium iodide (NaI) detectors are replaced with portable lanthanum tri-bromide cerium-doped ($LaBr_3$:Ce) detectors. Further steps are taken to simulate the camera's behaviour more realistically, such as the modelling of radionuclide decay times, scintillation photon transport and interactions with photomultipliers, as well as detector dead time corrections. The performance of the Si/$LaBr_3$:Ce Compton camera model is then compared with Si/NaI(Tl) and Si/CZT Compton camera models of similar geometry.

6.3.1 Camera geometry

The Compton camera model described in this study is dual-head detection system, with each detection head consisting of a scatterer and absorber that operate in time coincidence. The scatterer-to-absorber distance is taken to be 5 cm. The scatterer geometry is mostly as described in Section 5.3.3, except that since simulations are now performed at only 511 keV, energy resolution is assumed to be 2 keV (Watanabe *et al.*, 2005). Position measurements in the scatterer were estimated as being at the centre of the pixel in which the interaction occurred.

The absorber panel consists of an array of four 5 cm × 5 cm × 2 cm planar $LaBr_3$:Ce crystals that are attached to a 4.5 mm thick glass window that is coupled in front of an array of 16 × 16 closely packed, square photomultipliers with 6.25 mm × 6.25 mm dimensions. The crystals are surrounded by 0.5 mm aluminium, and a 0.3 mm Teflon material acting as a Lambertian reflector (reflects photons according to the Lambertian distribution) is used to cover the front surface of the crystal. The energy resolution is estimated as (Lo Meo *et al.*, 2008):

$$\Delta E = \sqrt{\Delta E_{st}^2 + \Delta E_{int}^2}, \tag{6.1}$$

where ΔE_{st} represents the Poissonian component of the energy resolution given by the square root of the number of collected photoelectrons, and ΔE_{int} is the intrinsic resolution of $LaBr_3$:Ce assumed to be approximately 18 keV at 511 keV (Moszyński *et al.*, 2007). The planar (x- and y-) positions of interactions in LaBr:Ce were estimated by implementing an improved Anger algorithm developed by Pani *et al.* (2008) in GEANT4 whereas the depth of photon interaction (z-) positions were estimated with an energy weighted position centroid algorithm in GEANT4 to account for the multiple interaction cases. Intrinsic spatial resolution for $LaBr_3$:Ce was set at 1 mm (Pani *et al.*, 2006b). While most Monte Carlo codes do not allow the simulation of the transport and boundary characteristics for optical photons generated by scintillating crystal, in GEANT4, certain optical models such as the UNIFIED model are available for this purpose. The detail of the UNIFIED model is described in Section 6.3.3. For comparison purposes, the $LaBr_3$:Ce crystals were replaced with CZT and NaI(Tl) detectors of similar dimensions. Details of the CZT design is as described in Section 5.3.3. The intrinsic energy resolution of the NaI(Tl) detector was adjusted to 34 keV at 511 keV (Bailey *et al.*, 2005) and the intrinsic spatial resolution to 3 mm (Zhang *et al.*, 2004). Note that the Si/Ge camera was not modelled due to Ge's poor sensitivity at 511 keV as demonstrated in Chapter 4. Figure 6.1 is the simulated diagram of the Si/$LaBr_3$:Ce scintimammographic camera and a human breast phantom with activity sources placed in between the scatterers.

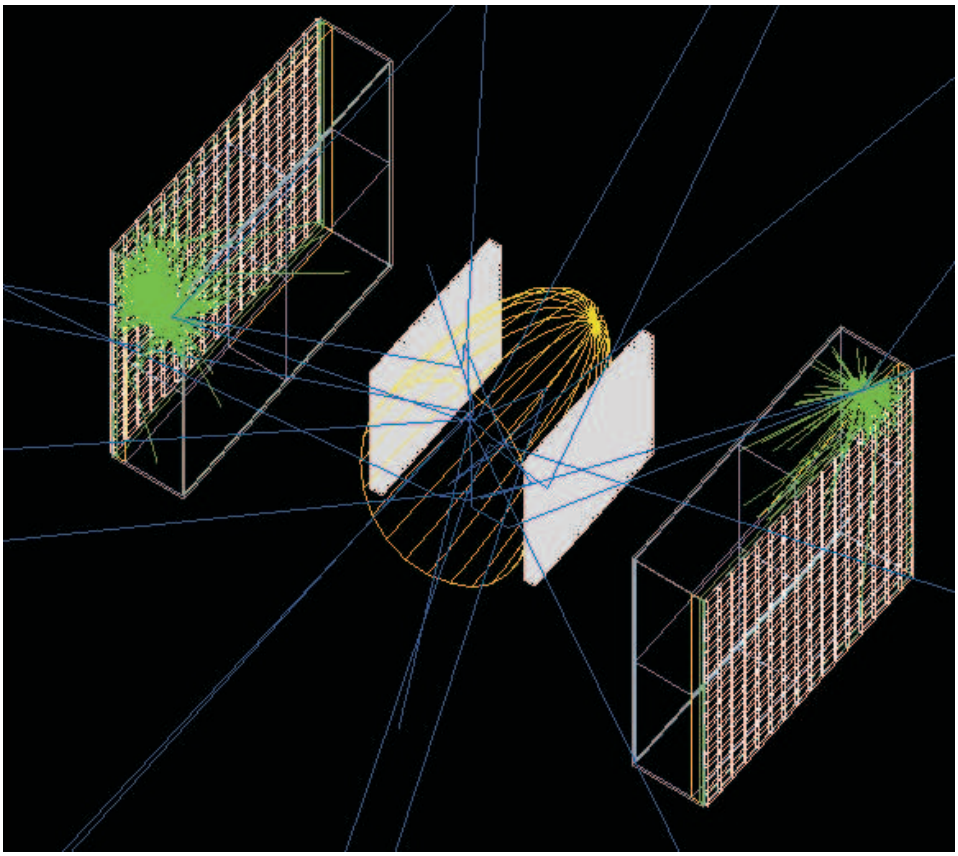

Figure 6.1: A simple simulation diagram of dual-head Compton camera and a breast phantom in between the scatterers. The breast phantom is represented with yellow wireframes to allow visualizing the activity sources in it. The blues lines represent the tracks of the gamma rays and the green lines represent the tracks of the scintillation photons.

6.3.2 Simulation tool

The physics and geometry of the above cameras are explicitly modelled with the GEANT4 simulation toolkit (release 9.3, patch 1) (Agostinelli *et al.*, 2003). GEANT4 allows the modelling of the radiation transport and interactions with the surrounding media, as well as boundary effects for the scintillation photons generated in a scintillation material. Also, the simulation toolkit has the capability to model the x-ray photon interacttions as well as the optical photon physics (e.g., scintillation, absorption, boundary effects), which makes it exceptionally well suited to detector simulations. The “LowEnergy” electromagnetic physics package of GEANT4 is very relevant to medical applications. Other capabilities allow GEANT4 to model the geometries and materials of the Compton camera, as well as the human organ in detail and realistically, making it possible to describe the experimental set-up accurately (Foppiano *et al.*, 2005).

6.3.3 Simulation overview

The general particle source package (GPS) of GEANT4 was used to simulate an isotropic point and spherical gamma ray sources in air and in a breast phantom that is approximated by a soft tissue material. To be successful, a photon event must start with the emission of a gamma ray from the radionuclide, and be detected in the scatterer and be fully absorbed in the absorber where the absorbed gamma ray triggers the generation of scintillation photons which must be detected by the photomultipliers coupled to the absorber. In order to model the wave like properties of the scintillation photons accurately, the detector surface finish properties also need to be considered. To do this, the boundary processes of the absorber crystal surfaces were modelled to follow the rules of the UNIFIED model developed for the DETECT project (Levin and Moisan, 1996). In this model, some combinations of surface finish properties such as polished or ground, enumerate the different situations which can be simulated. The 'Polish' model is meant to account for a perfectly polished surface that may or may not in optical contact with another component. If no other component is specified , the surface is assumed to interface with a vacuum. Photons incident on the surface are assumed to have random polarization, and are first tested for the possibility of Fresnel reflection if a change in refractive index occurs at the surface. If reflection does not occur, scintillation photon is transmitted with the complementary probability given by:

$$T = 1 - R, \tag{6.2}$$

where T is the transmission coefficient. If reflection is selected, the angle of reflection is set equal to the angle of incidence. The 'Ground' option is available to simulate a roughed or ground optical surface. In this case, surfaces are treated in the same way as the polished surfaces, except that the reflection and refraction follows the Lambertian distribution (Lo Meo *et al.*, 2008, 2009; Uche *et al.*, 2011).

The scintillation properties (refraction index and absorption length) of the scintillation absorber crystals used in the simulations are gathered from literature (Dyer, 2001; Kumar *et al.*, 2009; Moszyński *et al.*, 2002; Moszyński, 2003; Moszyński *et al.*, 2006). A scintillation light yield equal to 63000 photons/MeV is assumed for $LaBr_3$:Ce whereas 38000 photons/MeV is assumed for NaI(Tl). The decay times of the materials are assumed to be 16 ns and 230 ns respectively. The quantum efficiency of the photomultipliers was approximated by reducing the number of photons in the output by a factor, 0.27 (Pani *et al.*, 2008).

For the simulation with the isotropic point source in air, modelling was done with respect to the coincident detection efficiency and angular resolution of the camera models at a source-to-scatterer distance of 2.5 cm. This distance represents approximately half the thickness of a mildly compressed average-sized breast (Zhang *et al.*, 2004). The simulated hits data were corrected for decay times by assigning decay instants drawn from Poisson distribution derived from the G4Poisson class of GEANT4 to the emitted gamma rays, considering a source activity of 10 MBq with a decay constant adequate for ^{18}F (511 keV)

radionuclide. Gaussian blur was introduced to the times of the photon detections to account for the detector time jitter. The time resolution of the scatterer corresponds to an experimentally measured value of 12 ns (Studen *et al.*, 2004), whereas those of the absorber were assumed to be 300 ps for $LaBr_3$:Ce (Crespi *et al.*, 2009), 5 ns for CZT (Bolotnikov *et al.*, 1999) and 7.76 ns for NaI(Tl) (Seo *et al.*, 2010).

For the simulation with the spherical tumour sources in a breast phantom, a soft tissue of thickness 5 cm was inserted between the two camera heads to represent the thickness of a mildly compressed average-sized breast. In order to study a challenging detection case, the average size of the two breast tumours was chosen to be 5 mm in diameter and embedded in the medial region of the breast, that is, at 2.5 cm from each camera head. The activity concentration level of the breast phantom was set at 3.7 kBq mL^{-1} (Zhang *et al.*, 2004; Del Guerra *et al.*, 2002) and the tumour/breast radiation uptakes were assumed to be 10:1 and 6:1 for the first and second 5 mm breast tumours respectively. A minimum of one hundred million photon histories were simulated to generate enough photon statistics for image reconstruction. The simulated energy, position and time data were then saved to an output data file for dead time processing with MATLAB code.

6.3.4 Detector dead time corrections

The dead times of three data acquisition (DAQ) readout schemes are considered in this study and are accounted for using straightforward approximations. The dead times of the detectors and amplifiers were considered together, and were assumed to follow a paralyzable dead time behaviour of 1.1 μs between successive events. Signal outputs from the detector modules were analyzed by a second algorithm that mimicked the operation of a 128-channel multichannel analyzer (MCA). The dead time of the MCA follows the nonparalyzable dead time model, and is comprised of a variable processing time that is determined by the appropriate signal channel number, and a fixed memory storage time of 2 μs. For the coincidence detection scheme, pulses from the scatterer and the absorber were matched with their respective time stamps within a coincidence time window of 50 ns, and were then summed to find the deposited energies that added up to the radionuclide energy within a $\pm$10 keV energy window. Event singles from the coincidence scheme were then clocked out at a trigger rate of 250 kHz.

6.3.5 Image reconstruction

The energy and position information from the coincidence scheme were then processed on an event basis using a list-mode back-projection algorithm described in Section 2.9.3. The algorithm analyzed each parameter of the event data to reconstruct a source image. Image performance was estimated using the signal-to-noise ratio (SNR) and image resolution defined as the average of full-width-at-half-maximum (FWHM) values of the horizontal and vertical image profiles of the reconstructed source distribution.

6.4 Results and discussion

The performance of the three Compton camera models was first evaluated by comparing their resolutions and coincident detection efficiencies in an air medium. In Figure 6.2, the reconstructed source images and the corresponding angular resolution histograms for the camera models are presented for a point source located at a source-to-scatterer distance of 2.5 cm. The calculated image and angular resolutions of the camera models correspond to 4.2 mm and 4.1° for the Si/CZT camera, 4.9 mm and 5.0° for the Si/$LaBr_3$ camera, and 5.5 mm and 6.5° for the Si/NaI(Tl) camera, respectively. From these results, it is obvious that the best resolution is attained for the Si/CZT camera, followed by the Si/$LaBr_3$:Ce camera and then, the Si/NaI(Tl) camera. In the same vein, the calculated coincident detection efficiencies are 9.3×10^{-4} for the Si/CZT camera, 6.7×10^{-4} for the Si/$LaBr_3$:Ce camera and 4.3×10^{-4} for the Si/NaI(Tl) camera. Note that only the results of one camera head is shown due to insufficient computer memory to perform long simulations with the two camera heads. Nevertheless, preliminary results obtained with the two camera heads without including detector segmentation and scintillation photon simulation showed that results of the two camera heads are very similar due to the symmetry of the cameras.

An *et al.* (2007) suggest that an image resolution of 5 mm is required for efficient visualization of tumours. Hence, image resolution was manipulated by varying the cameras' imaging distance over 3 cm to 11 cm. The results are shown in Fig. 6.3. As can be seen in the figure, the image resolution is less than 5 mm for all the cameras at the scatterer-to-absorber distance of 7 cm, although with the efficiency compromise of approximately 30%. At this distance, the image resolution is 3.9 mm for the Si/CZT_3:Ce camera model, 4.4 mm for the Si/$LaBr_3$:Ce camera model and 4.9 mm for the Si/NaI(Tl) camera model. Based on these results, the scatterer-to-absorber distance of 7 cm was used to model the geometry of the cameras for the breast tumour imaging.

Breast tumours of about 5 mm diameter are usually considered to be the smallest size for tumour detectability in breast imaging. Tumour detectability was therefore analyzed by varying the tumour/background radiation uptakes of the spherical 5 mm sources from 10:1 ratio down to 6:1 ratio. The signal-to-noise ratio (SNR) is defined as (Del Guerra *et al.*, 2002):

$$SNR = \frac{T - B_g}{\sigma_{B_g}}, \tag{6.3}$$

where T is the average signal in the tumour region of interest (ROI), B_g is the average background signal in the ROI with the same size of the tumour and σ_{B_g} is the standard deviation of B_g. The obtained images of the tumours are shown in Fig. 6.4.

The measured SNR values for the 5 mm tumour with tumour/radiation uptake of 10:1 are 12.2 for the Si/CZT camera, 9.0 for the Si/$LaBr_3$:Ce camera and 6.5 for the Si/NaI(Tl) camera. Using the conventional statistical limit of visibility in analog radiology which is SNR of 5, it is obvious that the images of the 5 mm tumour with tumour/radiation uptakes of 10:1 would be visualized for all the cameras since their SNR values are greater than the

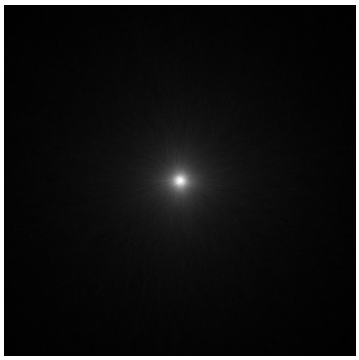

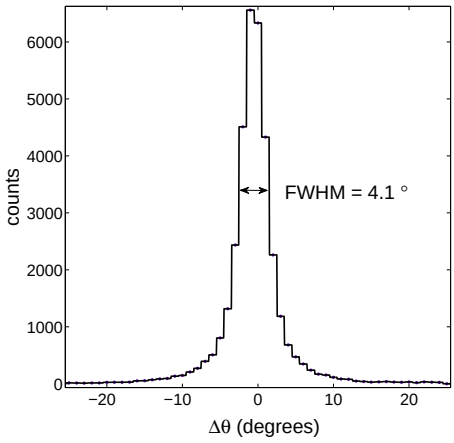

(a) (b)

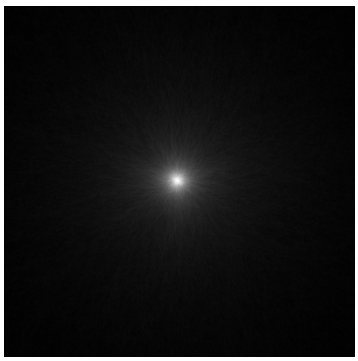

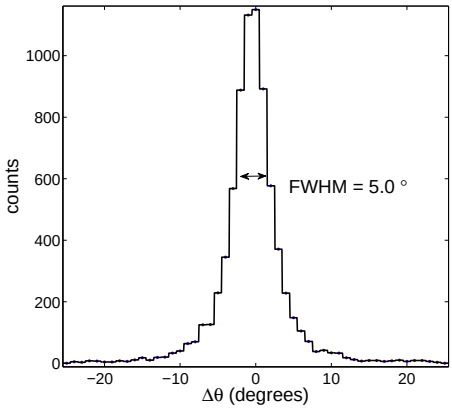

(c) (d)

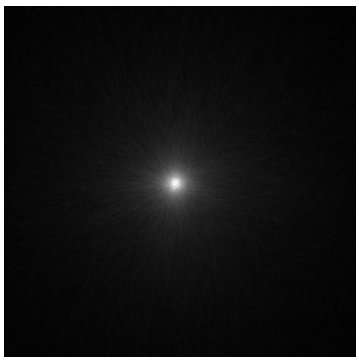

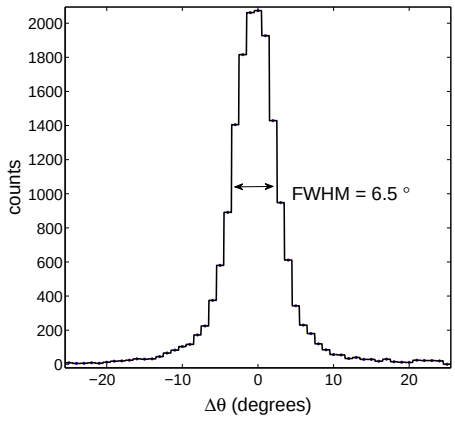

(e) (f)

Figure 6.2: Three reconstructed images of a point source and corresponding angular resolution histograms of (a) the Si/CZT Compton camera, (b) the Si/$LaBr_3$:Ce Compton camera and (c) the Si/NaI(Tl) Compton camera at 511 keV.

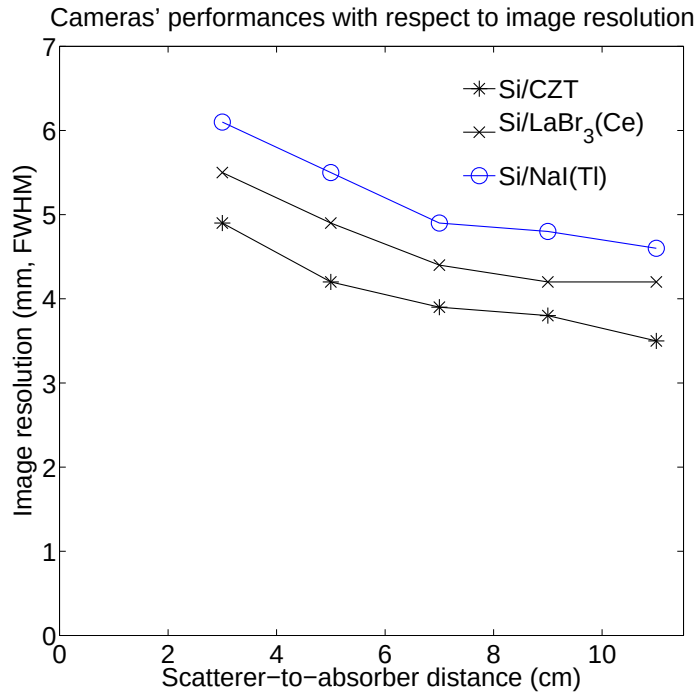

(a)

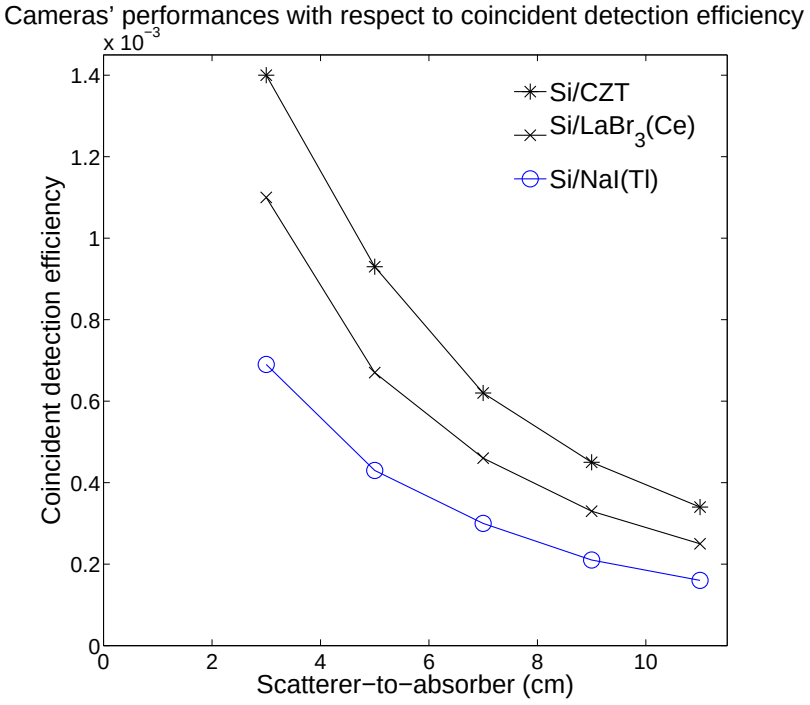

(b)

Figure 6.3: Graphs of: (a) image resolution and (b) coincident detection efficiency over the scatterer-to-absorber of 3 cm to 11 cm for all the camera models.

(a)

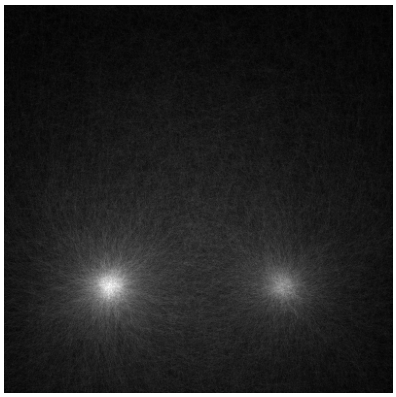

(b)

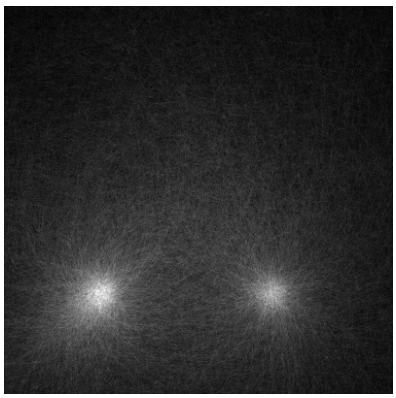

(c)

Figure 6.4: Reconstructed images of two spherical breast tumours embedded in the medial plane of a breast phantom, imaged with: (a) Si/CZT (b) Si/$LaBr_3$:Ce and (c) Si/NaI(Tl) Compton camera models.

conventional statistical limit of visibility in analog radiology. It may also be possible to visualize the image of the 6:1 tumour for the Si/CZT camera since the SNR value is 5.3. However, it is unlikely that the images of the 6:1 tumour for the Si/$LaBr_3$:Ce and Si/NaI(Tl) cameras would be visualized when the effect of background radiation from the heart, lungs and liver are taken into consideration since the SNR values are 4.0 and 4.2 respectively, which are below the statistical limit of visibility in analog radiology. It is however imagined that with better reconstruction techniques and adequate noise filter algorithms, there may be chances of improving SNR (Zhang *et al.*, 2004). For the 10:1 tumour, SNR is proportional to the coincident detection efficiency, suggesting that increased efficiency could further improve SNR. It is however difficult to fully assess the 6:1, 5 mm breast tumour case since the cameras generally recorded very low counts with the Si/NaI(Tl) camera showing the highest noise background.

The above results confirm the prediction by Pani *et al.* (2007) that $LaBr_3$:Ce could replace the widely used NaI(Tl) in nuclear medical imaging. However, this would only be possible if the present limitations of $LaBr_3$:Ce are overcome, such as higher production cost and difficulty in growing large volume crystals. On the other hand, the imaging performance of $LaBr_3$:Ce is slightly inferior to CZT. From this, one can infer that the combination of Si and CZT as the scatterer and the absorber of the Compton camera would make a very promising imaging system for scintimammography at higher gamma ray energies where the collimated gamma ray systems perform very poorly due to increased septal penetration.

Chapter 7

CONCLUSION AND FUTURE WORK

In this thesis, a more realistic and satisfying approach has been developed to study the operation of Compton cameras that are intended for medical applications than previous studies to date. In Chapter 1, the literature review indicates that current SPECT scanners are severely limited in performance due to resolution-efficiency trade-off by the mechanical collimator. A more efficient imaging SPECT camera is therefore sought. The Compton camera uses the process of Compton scattering to determine where a gamma ray has come from. The literature review indicates that this imaging system is able to overcome the present limitations of the current SPECT cameras due to its higher sensitivity and adequate resolution, thus suggesting some merits to exploit the potential applications in the medical field.

Since there is no easy way of isolating and analyzing the parameters of the system experimentally, a Monte Carlo simulation approach using the GEANT4 simulation toolkit is therefore used. GEANT4 allows the modelling of the radiation transport and interactions with the surrounding media, as well as optical physics in a scintillator. The "LowEnergy" electromagnetic physics package of GEANT4 is very relevant to medical applications. It provides the functionalities to model important detector parameters such as Doppler broadening. Other capabilities allow GEANT4 to model the geometries and materials of the Compton camera, as well as the human organs in detail and realistically, making it possible to describe the experimental set-up accurately. The major contributions that are made in this thesis are reported in the following.

Four analyses were used to validate the effect of Doppler broadening on the energy spectrum, angular uncertainty and reconstructed image in Chapter 3. It is shown that the behaviour of the Compton camera depends significantly on Doppler broadening at diagnostic energies lower than 300 keV, whereas at higher diagnostic energies, the effect is minimal. The impacts of detector geometry and material on the rate of photon interaction with respect to Compton scattering were then investigated with the goal of finding the optimal material and geometry. Analyses suggest that silicon of about 1 cm thickness would be suitable

as the Compton camera scatterer. The choice of silicon is however not completely ideal. Doppler broadening for this detector material contributes as much as 7.3 mm and 2.4 mm to FWHM image resolution at 140.5 keV and 511 keV respectively. Hence, the development of fast and robust reconstruction algorithms that would account for the effect is suggested.

The thesis progressed by considering how the parameters of the absorber contribute to the overall performance of the Compton camera in Chapter 4. Three potential absorber materials (cadmium zinc telluride (CZT), thallium-doped sodium iodide (NaI(Tl)) and germanium (Ge)) were selected for this study. Investigations were done to find the contribution of photon interaction type, multiple interaction occurrences and absorber pixel size on the performance of the whole camera. Findings suggest that the efficiency of CZT is comparable to that of NaI(Tl), but about 1.4 times that of Ge at 100 keV and 5 mm thickness. At 600 keV and 2 cm thickness, CZT efficiency increased to 1.6 times that of NaI(Tl) and 1.8 times that of Ge. On the other hand, Ge gave the best spatial resolution which is approximately 1.5 to 3 times better than that of NaI(Tl) across 1 mm to 3mm pixel size respectively. However, its low ratio of single photoelectric/multiple interaction suggests that it is more prone to inter-pixel cross-talk than the other materials at higher energies. In contrast, CZT which demonstrated the least positioning error due to multiple interactions also has comparable spatial resolution with Ge at all energies. This motivated the decision to simulate a Compton camera design based on Si and CZT detectors as the scatterer and absorber respectively. The evaluation of effects of the detector parameters of the Compton camera model on image resolution showed good agreement with previous studies. The detector spatial resolution which accounts for the least image degradation at 140.5 keV was found to be the dominant degrading factor at 511 keV, suggesting that the absorber parameters play major roles in image resolution at high gamma energies.

In Chapter 5, the limitations imposed by the Compton camera data acquisition (DAQ) system on performance was explored with a simplified model of the general electronic architecture. This is done by utilizing straightforward approximations to estimate the charge collection times and their relationship to finding coincident events, setting thresholds to reject noise, and the resultant impacts on the Compton camera performance. In other words, beside the basic detector parameters, modelling includes effects such as decay times, detection time jitters, energy threshold and dead time. The inclusion of the energy threshold and detector dead time at 140.5 keV, reduced the Compton camera detection efficiency by 48% and 17% respectively, but improved the image resolution from 10.7 mm to 9.5 mm. At 511 keV, the inclusion of the energy threshold and the time effects reduced the efficiency by 6% and 13% respectively, but made no significant difference on the camera resolution.

In Chapter 6, assessment of performance is made for three dual-head detection Compton camera models (Si/CZT camera model, Si/$LaBr_3$:Ce camera model and Si/NaI(Tl) camera model) for scintimammography. Simulation steps include the modelling of radionuclide decay times, optical physics and interactions with photomultipliers, as well as detector dead time corrections. Note that no other study has simulated all these aspects of the Compton camera. The performance of the three Compton camera models was evaluated by comparing

their resolutions and coincident detection efficiencies in an air medium for an isotropic point, and then in a breast phantom for two spherical breast tumours. In order to study a challenging detection case, the size of the two breast tumours was chosen to be 5 mm in diameter and embedded in the medial region of the breast, that is, at 2.5 cm from each camera head. The calculated image and angular resolutions of the camera models in the air medium correspond to 4.2 mm and 4.1° for the Si/CZT camera, 4.9 mm and 5.0° for the Si/$LaBr_3$ camera, and 5.5 mm and 6.5° for the Si/NaI(Tl) camera, respectively. Likewise, the calculated coincident detection efficiencies are 9.3×10^{-4} for the Si/CZT camera, 6.7×10^{-4} for the Si/$LaBr_3$:Ce camera and 4.3×10^{-4} for the Si/NaI(Tl) camera. The measured signal-to-noise ratio (SNR) values for the 5 mm tumour with tumour/background uptake of 10:1 are 12.2 for the Si/CZT camera, 9.0 for them Si/$LaBr_3$:Ce camera and 6.5 for the Si/NaI(Tl) camera. For the other 5 mm tumour with tumour/background uptake of 6:1, SNR value is 5.3 for the Si/CZT camera, 4.0 for the Si/$LaBr_3$:Ce camera and 4.2 for the Si/NaI(Tl) camera.

Using the conventional statistical limit of visibility in analog radiology which is SNR of 5, it is obvious that the images of the 5 mm tumour with tumour/background uptakes of 10:1 would be visualized for all the cameras. This statement is however not completely true for the 5 mm tumour with tumour/background uptake of 6:1. In any case, it was anticipated that with improved reconstruction technique and adequate filter algorithm, the images of the 6:1 tumour would be visualized. From the above results, it is envisioned that the combination of Si and CZT as the scatterer and the absorber of the Compton camera would make a very promising imaging system for scintimammography at higher gamma ray energies where the collimated SPECT systems perform very poorly due to increased septal penetration.

While the Compton camera shows promise for medical applications, more work is still needed to optimize its performance. The development of fast and robust reconstruction algorithms to account for the degrading effects of the scatterer would be very helpful for the camera to compete with the collimated SPECT systems in resolution at lower diagnostic energies. It is also suggested that future studies should include inter-pixel spacing and cross-talk that influence the camera's resolution and detection efficiency. The inclusion of significant effects such as pulse pileup and time walk in Compton camera DAQ algorithm would be of significant benefit as it would help to estimate event losses at high count rates more accurately. It is clear in Section 5.3.3 that the reported final cameras' efficiencies are not optimal since limited computer memory did not allow modelling of the optimal geometry of the complete scatterer configuration. Hence, future studies should consider the parallelization of the simulation to utilize all CPU cores. The assessment of the Compton camera performance in scintimammography can be significantly furthered to include more vital imaging factors such as tracer time and motion. It is also acknowledged that if other vital organs of the body are simulated and the effect of background radiation from them studied, the results of the scintimammographic study may change slightly.

References

Agostinelli, S., J. Allison, K. Amako, J. Apostolakis, H. Araujo, P. Arce, and et al. GEANT4 — a simulation toolkit. *Nuclear Instruments and Methods in Physics Research A*, **506**, pp. 250–303 (2003).

Allisy, A., W. A. Jennings, A. M. Kellerer, J. W. Müller, and H. H. Rossi. Radiation quantities and units, interaction coefficients and dosimetry. Technical Report 2, 5-12, ICRU News (1993).

An, S. H., H. Seo, J. H. Lee, C. S. Lee, J. S. Lee, and C. H. Kim. Effect of detector parameters on the image quality of Compton camera for ^{99m} Tc. *Nuclear Instruments and Methods in Physics Research A*, **571**, pp. 251–254 (2007).

Andersen, H. H. and J. F. Zieger. The stopping and ranges of ions in matter. *Pergamon Press*, **3** (1977).

Anderson, H. L. Metropolis, Monte Carlo and the MANIAC. *Los Alamos Science*, **14**, pp. 96–108 (1986).

Andreyev, A., A. Sitek, and A. Celler. Fast image reconstruction for Compton camera using stochatic origin ensemble approach. *Medical Physics*, **38(1)**, pp. 429–438 (2011).

Anger, H. Scintillation camera. *The Review of Scientific Instruments*, **29**, pp. 27–33 (1958).

Awadalla, S. A., H. Chen, J. Mackenzie, P. Lu, K. Iniewski, P. Marthandam, R. Redden, G. Bindley, Z. He, and F. Zhang. Thickness scalability of large volume cadmium zinc telluride high resolution radiation detectors. *Journal of Applied Physics*, **105(114910)** (2009).

Bailey, D. L., D. W. Townsend, P. E. Valk, and M. N. Maisey, editors. *Positron emission tomography, basic sciences*. Springer (2005).

Baro, J., J. Sempau, J. M. Fernandez-Varea, and F. Salvat. Penelope, an algorithm for Monte Carlo simulation of the penetration and energy loss of electrons and positrons in matter. *Nuclear Instruments and Methods in Physics Research B*, **100(1)**, pp. 31–46 (1995).

Barrand, G., P. Binko, M. Dönszelmann, A. Johnson, and A. Pfeiffer. Abstract interfaces for data analysis, component architecture for data analysis tools. In: *Proceedings of Computing in High Energy Physics (CHEP2001)*. Beijing, China (2001).

Basko, R., G. L. Zeng, and G. T. Gullberg. Application of spherical harmonics to image reconstruction for the Compton camera. *Phys. Med. Biol.*, **43**, pp. 887–894 (1998).

Berger, M. J., J. Hubbell, S. M. Seltzer, J. Chang, J. S. Coursey, R. Sukumar, and D. S. Zucker. *XCOM, photon cross section database.* NIST (2010). Http://physics.nist.gov/PhysRefData/Xcom/html/xcom1.html.

Beyer, T., D. W. Townsend, T. Brun, P. E. Kinahan, M. Charron, R. Roddy, J. Jerin, J. Young, L. Byars, and R. Nutt. A combined PET/CT scanner for clinical oncology. *Journal of Nuclear Medicine*, **41**, pp. 369–379 (2000).

Biggs, F., L. B. Mendelsohn, and J. B. Mann. Hartree-Fork Compton profiles for the elements. *Atomic Data and Nuclear Data Tables*, **16**, pp. 201–309 (1975).

Blumgart, H. L. and O. T. Yen. STUDIES ON THE VELOCITY OF BLOOD FLOW I. The Method Utilized. *The Journal of Clinical Investigation*, **4(1)**, pp. 1–13 (1927).

Bolotnikov, A. E., S. E. Boggs, W. R. Cook, F. A. Harrison, and S. M. Schindler. Use of a pulsed laser to study properties of CdZnTe pixel detectors. In: *Penetrating Radiation Systems and Applications*, volume 3769, pp. 52–58. Proceedings of SPIE (1999).

Brusa, D., G. Stutz, J. A. Riveros, J. M. FernÃąndez-Varea, and F. Salvat. Fast sampling algorithm for the simulation of photon Compton scattering. *Nuclear Instruments and Methods in Physics Research A*, **379**, pp. 167–175 (1996).

Bruyant, P. P. Analytic and iterative reconstruction algobrithms in SPECT. *The Journal of Nuclear Medicine*, **43(10)**, pp. 1343–1358 (2002).

Chelikani, S., J. Gore, and G. Zubal. Optimizing Compton camera geometries. *Physics in Medicine and Biology*, **49**, pp. 1387–1408 (2004).

Chen, H., S. A. Awadalla, K. Iniewski, P. H. Lu, F. Harris, J. Mackenzie, T. Hasanen, W. Chen, R. Redden, and G. Bindley. Characterization of large cadmium zinc telluride crystals grown by travelling heater method. *Journal of Applied Physics*, **103(014903)** (2008).

Chen, H., S. A. Awadalla, J. Mackenzie, R. Redden, G. Bindley, A. E. Bolotnikov, G. S. Camarda, G. Carini, and R. B. James. Characterization of travelling heater method (THM) grown Cd0.9Zn0.1Te crystals. *IEEE Transactions on Nuclear Science*, **54(4)**, pp. 811–816 (2007).

Cherry, S. R., J. A. Sorenson, and M. E. Phelps. *Physics in nuclear medicine*. SAUNDERS (2003).

Cree, M. and P. Bones. Towards direct reconstruction from a gamma camera based on Compton scattering. *IEEE Transactions on Medical Imaging*, **13(2)**, pp. 398–407 (1994).

Cree, M. J. *The Compton scattering camera in application to single photon emission computed tomography*. Ph.D. thesis, University of Canterbury, Christchurch, New Zealand (1994).

Crespi, F. C. L., F. Camera, N. Blasi, A. Bracco, S. Brambilla, B. Million, R. Nicolini, L. Pellegri, S. Riboldi, M. Sassi, O. Wieland, F. Quarati, and O. A. Alpha-gamma discrimination by pulse shape in LaBr3:Ce and LaCl3:Ce. *Nuclear Instruments and Methods in Physics Research A*, **602**, pp. 520–524 (2009).

Cullen, D., J. H. Hubdell, and L. Kissel. EPDL97, the evaluated photon data library. *UCRL-50400*, **6** (1997). Rev. 5.

Del Guerra, A., N. Belcari, W. Bencivelli, A. Motta, S. Righi, A. Vaiano, G. Di Domenico, E. Moretti, N. Sabba, G. Zavattini, R. Campanini, N. Lanconelli, A. Riccardi, M. Cinti, R. Pani, and R. Pellegrini. Monte Carlo study and experimental measurements of breast tumor detectability with the YAP-PEM prototype. In: *2002 IEEE Nuclear Science Symposium Conference Record*, volume 3, pp. 1887 – 1891. IEEE, Pisa, Italy (2002).

Dogan, N. and D. K. Wehe. Efficiency and angular resolution calculations for a prototype multiple Compton scatter camera. *Nuclear Instruments and Methods in Physics Research A*, **345**, pp. 296–302 (1994).

Donegan, W. L. Evaluation of a palpable breast mass. *The New England Journal of Medicine*, **327(13)**, pp. 937–942 (1992).

Dorenbos, P., J. T. M. de Haas, and C. W. E. van Eijk. Non-proportionality in the scintillation response and the energy resolution obtainable with scintillation crystals. *IEEE Transactions on Nuclear Science*, **42(6)**, pp. 2190–2202 (1995).

Du, Y. F., Z. He, G. F. Knoll, D. K. Wehe, and W. Li. Evaluation of a Compton scattering camera using 3-D position sensitive CdZnTe detectors. *Nuclear Instruments and Methods in Physics Research A*, **457**, pp. 203–211 (2001).

Dyer, S. A., editor. *Survey of instrumentation and measurement*. John Wiley & Sons, Inc (2001).

Fisher, B., M. Bauer, D. L. Wickerham, C. K. Redmond, E. R. Fisher, A. B. Cruz, R. Foster, B. Gardner, H. Lerner, and R. Margolese. Relation of number of positive axillary nodes to the prognosis of patients with primary breast cancer. *Cancer*, **52**, pp. 1551–1557 (1983).

Foppiano, F., S. Guatelli, and M. G. Pia. A general-purpose dosimetric system for brachytherapy. In: *American Nuclear Society* (2005).

GEANT4 Collaboration. Physics reference manual. `http://www.geant4.org/geant4/support/userdocuments/shtml` (2011).

geant4.web.cern.ch. Geant4 website address. `http://www.geant4.org/geant4/` (2011).

Ghogali, W., R. D. Speller, G. J. Royle, J. Gabathuse, P. J. Sellin, I. H. Lazarus, and D. E. Appelbe. Detector characteristics of a pixellated germanium Compton camera for nuclear medicine. In: *IEEE Nuclear Science Symposium, 2004 Conference Record.*, volume 4, pp. 2216–2220. IEEE (2004).

Griesmer, J. J., J. Kline, B.and Grosholz, K. Parnham, and D. Gagnon. Performance evaluation of a new CZT detector for nuclear medicine: SOLSTICE. In: *Nuclear Science Symposium Conference Record 2001 IEEE (2001)*, volume 2, pp. 1050–1054. IEEE (2002).

Gruber, G. J., W. W. Moses, and S. E. Derenzo. Monte Carlo simulation of breast tumor imaging properties with compact, discrete gamma cameras. *IEEE Transactions on Nuclear Science*, **46**, pp. 2119 – 2123 (1999).

Hamamatsu Photonics, K. K. *Photomultiplier tubes, basics and applications*. Hamamatsu Photonics K.K., Hamamatsu City, Japan, third edition edition (2006).

Harkness, L. J., A. J. Boston, H. C. Boston, R. J. Cooper, J. R. Cresswell, A. N. Grint, P. J. Nolan, D. C. Oxely, D. P. Scraggs, T. Beveridge, J. Gillam, and I. Lazarus. Optimisation of a dual head semiconductor Compton camera using GEANT4. *Nuclear Instruments and Methods in Physics Research A*, **604**, pp. 351–354 (2009).

Hawkins, R. A. and M. E. Phelps. Pet in clinical oncology. *Cancer and metastasis reviews*, **7**, pp. 119–142 (1988).

Hebert, T., R. Leahy, and M. Singh. Three-dimensional maximum-likelihood reconstruction for an electronically-collimated single-photon-emission imaging system. *Journal of the Optical Society of America A*, **7**, pp. 1305–1313 (1990).

Hirasawa, M. and T. Tomitani. An analytical image reconstruction algorithm to compensate for scattering angle broadening in Compton cameras. *Physics in Medicine and Biology*, **48**, pp. 1009–1026 (2003).

Hofstadter, R. and J. McIntyre. Measurement of gamma-ray energies with two crystals in coincidence. *Physical Review*, **78**, pp. 619–620 (1950).

Holly, T. A., B. G. Abbott, M. Al-Mallah, D. A. Calnon, M. C. Cohen, F. P. DiFilippo, E. P. Ficaro, M. R. Freeman, R. C. Hendel, and D. e. a. Jain. Single photon-emission computed tomography. *Journal of Nuclear Cardiology*, **17(5)**, pp. 941–973 (2010).

Hua, C.-h. *Compton imaging system development and performance assessment*. Ph.D. thesis, The University of Michigan (2000).

Hua, C. H., N. H. Clinthorne, S. J. Wilderman, J. W. LeBlanc, and W. L. Rogers. Quantitative evaluation of information loss for Compton cameras. *IEEE Transactions on Nuclear Science*, **46**, pp. 587 – 593 (1999).

Hubbell, J. H., W. H. Veigele, E. A. Briggs, R. T. Brown, D. T. Cromer, and R. J. Howerton. Atomic form factors, incoherent scattering functions, and photon scattering cross sections. *Journal of Physical and Chemical Reference Data*, **4**, pp. 471–538 (1975).

Kao, C. H., S. J. Wang, and S. H. Yeh. Tc-99m MIBI uptake in breast carcinoma and axillary lymph node metastases. *Clinical Nuclear Medicine*, **19**, pp. 898–900 (1994).

Khalkhali, I., J. Villanueva-Meyer, S. L. Edell, J. L. Connolly, S. J. Schnitt, J. K. Baum, M. J. Houlihan, R. M. Jenkins, and S. B. Haber. Diagnostic accuracy of ^{99m}Tc sestamibi breast imaging: multicenter trial results. *Journal of Nuclear Medicine*, **41(1973-1979)** (2000).

Kim, S. M., J. S. Lee, C. S. Lee, C.-H. Kim, M. C. Lee, D. S. Lee, and S.-J. Lee. Fully three-dimensional OSEM-based image reconstruction for Compton imaging using optimized ordering schemes. *Physics in Medicine and Biology*, **55**, pp. 5007–5027 (2010).

Kim, S. M., J. S. Lee, M. N. Lee, J. H. Lee, C. S. Lee, C.-H. Kim, D. S. Lee, and S.-J. Lee. Two approaches to implementing projector-backprojector pairs for 3D reconstruction from Compton scattered data. *Nuclear Instruments and Methods in Physics Research A*, **571**, pp. 255–258 (2007).

Klein, O. and Y. Nishina. Scattering of radiation by free electrons on the new relativistic quantum dynamics of Dirac. *Z. Physik*, **52(11-12)**, pp. 853–868 (1929).

Knoll, G. F. *Radiation detection and measurement*. John Wiley & Sons, Inc., third edition edition (2000).

Kroeger, R. A., W. N. Johnson, R. L. Kinzer, J. D. Kurfess, S. Inderhees, B. Phlips, and N. Gehrels. Spatial and spectral resolution of a germanium strip detector. *Physics and Astronomy, Atomic and Molecular Physics and Spectroscopy* (1994).

Kumar, G. A., I. Mazumdar, and D. A. Gothe. Efficiency calibration and simulation of a $LaBr_3Ce$ detector in close-geometry. *Nuclear Instruments and Methods in Physics Research A*, **609**, pp. 183–186 (2009).

Lam, W. W. W., W. T. Yang, and Y. L. Chan. Detection of axillary lymph node metastases in breast carcinoma by technetium-99m sestamibi breast scintigraphy, ultrasound and conventional mammography. *European Journal of Nuclear Medicine*, **23**, pp. 498–503 (1996).

LeBlanc, J. W. *A Compton camera for low energy gamma ray imaging in nuclear medicine applications*. Ph.D. thesis, University of Michigan (1999). Ph.D. Thesis.

Leblanc, J. W., X. Bai, N. H. Clinthorne, C. Hua, D. Meier, W. L. Rogers, D. K. Wehe, P. Weilhammer, and S. J. Wilderman. ^{99m}Tc imaging performance of the C-SPRINT Compton camera. In: *IEEE Nuclear Science Symposium, 1999 Conference Record.*, volume 1, pp. 545–552. Seattle, WA (1999).

LeBlanc, J. W., N. H. Clinthorne, C. Hua, W. L. Rogers, D. K. Wehe, and S. J. Wilderman. A Compton camera for nuclear medicine applications using ^{113m}in. *Nuclear Instruments and Methods in Physics Research A*, **422**, pp. 735–739 (1999).

LeBlanc, J. W., N. H. Clinthorne, C.-H. Hua, E. Nygard, W. Rogers, D. Wehe, P. Weilhammer, and S. Wilderman. C-sprint: a prototype Compton camera system for low energy gamma ray imaging. *IEEE Transactions on nuclear science*, **45**, pp. 943–949 (1998).

Lee, W., D. Wehe, M. Jeong, P. Barton, and J. Berry. A dual modality gamma camera using $LaCl_3$Ce scintillator. *IEEE Transactions on Nuclear Science*, **56(1)**, pp. 308–315 (2009).

Leo, W. R. *Techniques for nuclear and particle physics experiments, a how-to approach*. Springer-Verlag, second edition edition (1994).

Levin, A. and C. Moisan. A more physical approach to model the surface treatment of scintillation counters and its implementations into DETECT. In: *Nuclear Science Symposium Conference Record, 1996 IEEE*, volume 2, pp. 702–706. IEEE (1996).

Lo Meo, S., G. Baldazzi, P. Bennati, D. Bollini, V. O. Cencelli, M. N. Cinti, N. Lanconelli, G. Moschini, F. L. Navaria, R. Pani, R. Pellegrini, A. Perrotta, and F. Vittorini. Geant4 simulation for modelling the optics of LaBr scintation. In: *2008 IEEE Nuclear Science Symposium Conference Record*, number M10-242, pp. 4964–4968. IEEE (2008).

Lo Meo, S., P. Bennati, M. N. Cinti, N. Lanconelli, F. L. Navaria, R. Pani, R. Pellegrini, A. Perrotta, and F. Vittorini. A GEANT4 simulation code for simulating optical photons in SPECT scintillation detectors. In: *4th International conference on imaging technologies in biomedical sciences, from medical images to clinical information – bridging the gap*, pp. 1–5. IOP Publishing Ltd and SISSA, Milos Island , Greece (2009).

van Loef, E. V. D., P. Dorenbos, C. W. E. van Eijk, K. W. Krämer, and H. U. Güdelb. Scintillation properties of $LaBr_3$:Ce^{3+} crystals: fast, efficient and high-energy-resolution scintillators. *Nuclear Instruments and Methods in Physics Research Section A*, **486**, pp. 254–258 (2002).

Longo, F., L. Pandola, and M. G. Pia. New GEANT4 developments for doppler broadening simulation in Compton scattering - development of charge transfer simulation models in GEANT4. In: *Nuclear Science Symposium Conference Record, 2008. NSS '08. IEEE*, pp. 2865–2868. IEEE, Dresden, Germany (2008).

Majewski, S., R. Raylman, B. Kross, V. Popov, A. G. Weisenberger, B. Welch, and R. Wojcik. Evaluation of a double layer 2x2 cm thick pixellated NaI(Tl) array for application in positron imager. In: *Proceedings of the 2003 IEEE Nuclear Science Symposium*, volume 3, pp. 2153–2155. IEEE (2003).

Martin, J., G. Knoll, D. Wehe, N. Dogan, V. Jordanov, N. Petrick, and M. Singh. A ring Compton scatter camera for imaging medium energy gamma rays. *IEEE Transactions on nuclear science*, **40**, pp. 972–978 (1993).

Martin, J., G. Knoll, D. Wehe, N. Dogan, V. Jordanov, N. Petrick, and M. Singh. Imaging multi-energy gamma ray fields with a Compton scatter camera. *IEEE Transactions on Nuclear Science*, **41**, pp. 1019–1025 (1994).

Martin, J. B. *A Compton scatter camera for spectral imaging of 0.5–3.0 MeV gamma rays*. Ph.D. thesis, University of Michigan (1994). Ph.D. Thesis.

Maxim, V., M. Frandeş, and R. Prost. Analytical inversion of the Compton transform using the full set of available projections. *IOP Publishing*, **25(9)**, pp. 1–21 (2009).

McCarthy, T. J., S. W. Schwarz, and M. J. Welch. Nuclear medicine and positron emission tomography: an overview. *Journal of Chemical Education*, **71**, pp. 830–836 (1994).

McKillop, J. H. Nuclear medicine. *Radiation protection dosimetry*, **68(1/2)**, pp. 47–53 (1996).

Meier, D., A. Czermak, P. Jalocha, B. Sowicki, M. Kowal, W. Dulinski, G. Maehlum, E. Nygard, K. Yoshioka, J. Fuster, C. Lacasta, M. Mikuz, S. Roe, P. Weilhammer, C. Hua, S. Park, S. Wildermann, L. Zhang, N. Clinthorne, and W. Rogers. Silicon detector for a Compton camera in nuclear medical imaging. *IEEE Transactions on nuclear science*, **49**, pp. 812–816 (2002).

Ministry of Health. Cancer new registrations and deaths 2005. Technical Report 18-19, Ministry of Health, Wellington:MOH (2008).

Ministry of Health/NZHIS/BSA. Personal communication. personal communication:. Technical report, Ministry of Health (2007). Bercinskas, L (2007) and Childs, J.(2009).

Morris, P. J. and R. A. Malt, editors. *Oxford textbook of surgery*, volume 1. Oxford University Press, second edition edition (2000).

Moszyński, M. Inorganic scintillation detectors in γ-ray spectrometry. *Nuclear Instruments and Methods in Physics Research A*, **505**, pp. 101–110 (2003).

Moszyński, M., A. Nassalski, A. Syntfeld-Każuch, T. Szczęśniak, W. Czarnacki, D. Wolski, P. G., and J. Stein. Temperature dependences of LaBr3(Ce), LaCl3(Ce) and NaI(Tl) scintillators. *Nuclear Instruments and Methods in Physics Research A*, **568**, pp. 739–751 (2006).

Moszyński, M., L. Świderski, T. Szczęśniak, A. Nassalski, A. Syntfeld-Każuch, W. Czarnacki, G. Pausch, S. J., L. P., F. Lherbert, and F. Kniest. Study of $LaBr_3$ crystals coupled to photomultipliers and avalanche photodiodes. In: *2007 IEEE Nuclear Science*

Symposium Conference Record, number N24-172, pp. 1351–1357. IEEE, New York, N.Y. (2007).

Moszyński, M., L. Świderski, T. Szczęśniak, A. Nassalski, A. Syntfeld-Kazuch, W. Czarnacki, G. Pausch, J. Stein, P. Lavoute, F. Lherbert, and F. Kniest. Study of $LaBr_3$ crystals coupled to photomultipliers and avalanche photodiodes. *IEEE Transactions on nuclear science*, **55**, pp. 1774 – 1780 (2008).

Moszyński, M., J. Zalipska, M. Balcerzyk, M. Kapusta, W. Mengesha, and J. D. Valentine. Intrinsic energy resolution of NaI(Tl)[1]. *Nuclear Instruments and Methods in Physics Research A*, **484**, pp. 259–269 (2002).

Mundy, D. W. and M. G. Herman. Uncertainty analysis of a Compton camera imaging for radiation therapy dose reconstruction. *Medical Physics*, **37(5)**, pp. 2341–2350 (2010).

Nakamura, K. e. Review of particle physics. *Journal of Physics G, Nuclear and Particle Physics*, **37** (2010).

Çonka Nurdan, T. *High resolution measurements with silicon drift detectors for Compton camera applications*. Ph.D. thesis, Universität Siegen, FB Physik, Emmy-Noether-Campus, Walter-Flex-Str. 3, Siegen 57072, Germany (2004).

Ordonez, C. E., A. Bolozdynya, and W. Chang. Doppler broadening of energy spectra in Compton cameras. In: *IEEE Nuclear Science Symposium and Medical Imaging Conference*, volume 2, pp. 1361–1365. Albuquerque, NM , USA (1997).

Ordonez, C. E., W. Chang, and A. Bolozdynya. Angular uncertainties due to geometry and spatial resolution in Compton cameras. *IEEE Transactions on nuclear science*, **46**, pp. 1142–1147 (1999).

Palmedo, H., A. Schomburg, and F. Grunwald. Technetium-99m scintimammography for suspicoius breast lesions. *Journal of Nuclear Medicine*, **37**, pp. 626–630 (1996).

Pani, R., M. N. Cinti, R. Pellegrini, M. Betti, G. Devincentis, P. Bennati, S. Ridolfi, G. Iurlaro, L. Montani, R. Scafé, M. Marini, L. M. Porfiri, G. Giachetti, F. Baglini, G. Salvadori, M. Madesani, M. Pieracci, C. F., and A. Bigongiari. Compact large FOV gamma camera for breast molecular imaging. *Nuclear Instruments and Methods in Physics Research A*, **569**, pp. 255–259 (2006a).

Pani, R., R. Pellegrini, M. Betti, G. De Vincentis, M. N. Cinti, P. Bennati, F. Vittorini, V. Casali, M. Mattioli, V. Orsolini Cencelli, F. Navarria, D. Bollini, G. Moschini, G. Iurlaro, L. Montani, and F. De Notaristefani. Clinical evaluation of pixellated NaI:Tl and continuous $LaBr_3Ce$, compact scintillation cameras for breast tumours imaging. *Nuclear Instruments and Methods in Physics Research A*, **571**, pp. 475–479 (2007).

Pani, R., R. Pellegrini, M. N. Cinti, P. Bennati, M. Betti, V. Casali, O. Schillaci, M. Mattioli, V. Orsolini Cencelli, F. Navarria, D. Bollini, G. Moschini, F. Garibaldi, F. Cusanno, G. Iurlaro, L. Montani, S. R., and F. de Notaristefani. Recent advances and future perspectives of gamma imagers for scintimammography. *Nuclear Instruments and Methods in Physics Research A*, **569**, pp. 296–300 (2006b).

Pani, R., F. Vittorini, R. Pellegrini, P. Bennati, M. Cinti, M. Mattioli, R. Scafé, S. Lo Meo, F. Navarria, G. Moschini, P. Boccaccio, V. O. Cencelli, and F. De Notaristefani. High spatial and energy resolution gamma imaging based on LaBr3(Ce) continuous crystals. In: *Nuclear Science Symposium Conference Record, 2008. NSS '08. IEEE*, pp. 1763–1771. IEEE, Dresden, Germany (2008).

Park, J. H., H. Seo, C. H. Kim, J. H. Lee, C. S. Lee, and J. S. Lee. Explicit modelling of timing characteristics in Compton camera simulation with GEANT4. *Nuclear Instruments and Methods in Physics Research A* (2010). "in press".

Parra, L. C. Reconstruction of cone-beam projections from Compton scattered data. *IEEE Transactions on nuclear science*, **47**, pp. 1543–1550 (2000).

Perkins, S. T., D. E. Cullen, and S. M. Seltzer. Tables and graphs of atomic subshell and relaxation data derived from the LLNL evaluated atomic data library (EADL), z=1-100. *UCRL-50400*, **30** (1997a).

Perkins, S. T., D. E. Cullen, and S. M. Seltzer. Tables and graphs of electron-interaction cross-sections from 10 eV to 100 GeV derived from the LLNL evaluated electron data library (eedl), z=1-100. *UCRL-50400*, **31** (1997b).

Phelps, M. E., H. E. J., N. A. Mullani, and M. M. Ter-pogossian. Application of anihilation coincidence detection to transaxial reconstruction tomography. *Journal of Nuclear Medicine*, **16**, pp. 210–224 (1975).

Philips, B. F., W. N. Johnson, R. A. Kroeger, and J. D. Kurfess. Development of thick silicon detectors for hard x-ray and gamma-ray detection. In: *Conference Record 2001 IEEE Nuclear Science Symposium*, volume 1, pp. 207–211. IEEE, San Diego (2001).

Phillips, W. G. Gamma-ray imaging with Compton cameras. *Nuclear Instruments and Methods in Physics Research B*, **99**, pp. 674–677 (1995).

Pia, M. G. The GEANT4 toolkit, simulation capabilities and application results. *Nuclear Physics B (Proceedings Supplements)*, **125**, pp. 60–68 (2003).

Podgoršak, E. B. *Radiation physics for medical physicists*. Springer (2006).

Reed, W. A. and P. Eisenberger. Gamma-ray Compton of diamond, silicon, and germanium. *Physical Review B*, **6**, p. 12 (1972).

Ribberfors, R. Relationship of the relativistic Compton cross section to the momentum distribution of bound electron states. *Physical Review B*, **12(6)**, pp. 2067–2074 (1975).

Rogers, W. L., N. H. Clinthorne, and A. Bolozdynya. Compton camera for nuclear medical imaging. In: *Emission tomography: The fundamentals of SPECT and PET*, edited by J. N. Wernick, M. N.and Aarsvold, chapter 19, pp. 383–420. Elsevier, San Diego, CA, first edition (2004).

Sauve, A. C., A. O. Hero, W. L. Rogers, S. J. Wilderman, and N. H. Clinthorne. 3D image reconstruction for a Compton SPECT camera model. *IEEE Transactions on nuclear science*, **46**, pp. 2075 – 2084 (1999).

Schönfelder, V., K. Bennett, H. Bloemen, R. Diehl, W. Hermsen, G. Lichti, M. McConnell, J. Ryan, A. Strong, and C. Winkler. COMPTEL overview: achievements and expectations. *Astronomy and Astrophysics Supplement*, **120**, pp. 13–21 (1996).

Schönfelder, V., R. Diehl, G. Lichti, H. Steinle, B. Swanenburg, A. Deerenberg, H. Aarts, J. Lockwood, W. Webber, J. Macri, J. Ryan, G. Simpson, B. Taylor, K. Bennett, and S. M. The imaging compton telescope COMPTEL on the gamma ray observatory. *IEEE Transactions on Nuclear Science*, **NS-31**, pp. 766–770 (1984).

Schönfelder, V., A. Hirner, and S. K. A telescope for soft gamma ray astronomy. *Nuclear Instruments and Methods*, **107**, pp. 385–394 (1973).

Seo, H., C. H. Kim, J. H. Park, J. K. Kim, J. H. Lee, C. S. Lee, and J. S. Lee. Development of double-scattering-type Compton camera with double-sided silicon strip detectors and NaI(Tl) scintillation detector. *Nuclear Instruments and Methods in Physics Research A*, **615**, pp. 333–339 (2010).

Seo, H., S. H. Lee, C. H. Kim, S. H. An, J. H. Lee, and L. C. S. Optimal geometrical configuration of a double-scattering Compton camera for maximum imaging resolution and sensitivity. *Nuclear Instruments and Methods in Physics Research A*, **591**, pp. 80–83 (2008).

Singh, M. An electronically collimated gamma camera for single photon emission computed tomography. part I: theoretical considerations and design criteria. *Medical Physics*, **10**, pp. 421–427 (1983).

Singh, M. and H. Chris. Use of a germanium detector to optimize scatter correction in SPECT. *The Journal of Nuclear Medicine*, **28**, pp. 1853–1860 (1987).

Singh, M. and D. Doria. An electronically-collimated gamma camera for SPECT. part ii: image reconstruction and preliminary experimental measurements. *Medical Physics*, **10(4)**, pp. 428–435 (1983).

Singh, M. and D. Doria. Single photon imaging with electronic collimation. *IEEE Transactions on Nuclear Science*, **32**, pp. 843–847 (1985).

Singh, M., D. E. Gustafson, B. M. J., B. K. Gilbert, and E. L. Ritman. Physics of electronic collimation for single photon transaxialtomography. In: *Medical Publisher*, volume 4, p. 350 (1977). Abstract only.

Singh, M., R. Leahy, R. Brechner, and T. Hebert. Noise propagation in electronically collimated single photon imaging. *IEEE Transactions on Nuclear Science*, **35**, pp. 772–777 (1988).

Smith, B. Reconstruction methods and completeness conditions for two Compton data models. *Journal of the Optical Society of America A*, **22(3)**, pp. 445–459 (2005).

Stickel, J. R. and S. R. Cherry. High-resolution PET detector design: modelling components of intrinsic spatial resolution. *Physics in Medicine and Biology*, **50**, pp. 179–195 (2005).

Studen, A. *Compton camera with position-sensitive silicon detectors*. Ph.D. thesis, University of Ljubljana (2005a).

Studen, A. Compton camera with position-sensitive silicon detectors (2005b). Available at www-f9.ijs.si/študen/sola/thesis/Slides_Studen.pdf.

Studen, A., E. Burdette, D.and Chesi, V. Cindro, N. H. Clinthorne, W. Dulinski, J. Fuster, L. Han, H. Kagan, C. Lacasta, G. Llosá, A. C. Marques, N. Malakhov, D. Meier, M. Mikuz, S. J. Park, S. Roe, W. L. Rogers, J. Steinberg, P. Weilhammer, S. J. Wilderman, L. Zhang, and D. Zontar. First coincidences in pre-clinical Compton camera prototype for medical imaging. *Nuclear Instruments and Methods in Physics Research A*, **531**, pp. 258–264 (2004).

Studen, A., V. Cindro, N. H. Clinthorne, A. Czermak, W. Dulinski, J. Fuster, L. Han, P. Jalocha, M. Kowal, T. Kragh, C. Lacasta, G. Llosá, D. Meier, M. Mikuz, E. Nygard, S. J. Park, S. Roe, W. L. Rogers, B. Sowicki, P. Weilhammer, S. J. Wilderman, K. Yosshioka, and L. Zhang. Development of silicon pad detectors and readout electronics for a Compton camera. *Nuclear Instruments and Methods in Physics Research A*, **501**, pp. 273–279 (2003).

Taillefer, R., A. Robidoux, R. Lambert, S. Turpin, and J. Laperriére. Technetium-99m–Sestamibi prone scintimammography to detect primary breast cancer and axillary lymph node involvement. *Journal of Nuclear Medicine*, **36**, pp. 1758–1765 (1995).

Ter-Pogossian, M. E., M. M.and Phelps, E. J. Hoffman, and N. M. N. A. A positron-emission transaxial tomograph for nuclear imaging (pet). *Radiology*, **114(1)**, pp. 89–98 (1975).

Todd, R., J. Nightingale, and D. Everett. A proposed gamma camera. *Nature*, **251**, pp. 132–134 (1974).

Tomitani, T. and M. Hirasawa. Image reconstruction from limited angle Compton camera data. *Physics in Medicine and Biology*, **47**, pp. 2129–2145 (2002).

Townsend, D. W. and T. Beyer. A combined PET/CT scanner, the path to true image fusion. *The British Institute of Radiology*, **75**, pp. S24–S30 (2002).

Troy, D. B., editor. *Remington: the science and practice of pharmacy*. Lippincott Williams & Wilkins (2006).

Uche, C. Z., W. H. Round, and M. J. Cree. Effects of energy threshold and dead time on Compton camera performance. *Nuclear Instruments and Methods in Physics Research A*, **641**, pp. 114–120 (2011).

Watanabe, S., T. Tanaka, K. Nakazawa, T. Mitani, K. Oonuki, T. Takahashi, T. Takashima, H. Tajima, Y. Fukazawa, M. Nomachi, S. Kubo, M. Onishi, and Y. Kuroda. A Si/CdTe semiconductor Compton camera. *IEEE Transactions on Nuclear Science*, **52**, p. 2045 (2005).

Wilderman, S., N. H. Clinthorne, J. A. Fessler, and W. Les Rogers. List-mode maximum likelihood reconstruction of Compton scatter camera images in nuclear medicine. In: *Proceedings of the 1998 IEEE Nuclear Science Symposium*. IEEE (1998a).

Wilderman, S. J., J. A. Fessler, N. H. Clinthorne, J. W. LeBlanc, and W. L. Rogers. Improved of system response in list mode EM reconstruction of Compton camera scatter images. *IEEE Transactions on Nuclear Science*, **48**, pp. 111–116 (2001).

Wilderman, S. J., W. L. Rogers, G. F. Knoll, and J. C. Engdahl. Fast algorithm for list mode back-projection of Compton scatter camera data. *IEEE Transactions on Nuclear Science*, **45**, pp. 957–962 (1998b).

Zhang, L., W. L. Rogers, and N. H. Clinthorne. Potential of a Compton camera for high performance scintimammography. *Physics in Medicine and Biology*, **49**, pp. 617–638 (2004).

Zoglauer, A. and G. Kanbach. Doppler broadening as a lower limit to the angular resolution of next generation Compton telescopes. In: *Proceedings of the SPIE*, volume 4851, pp. 1302–1309. SPIE (2003).